Axinos in the Sky and on Earth

Dissertation

zur
Erlangung der naturwissenschaftlichen Doktorwürde
(Dr. sc. nat.)
vorgelegt der
Mathematisch-naturwissenschaftlichen Fakultät
der
Universität Zürich
von

Nurhana Tajuddin

aus
Malaysia

Promotionskomitee
Prof. Dr. Daniel Wyler
Prof. Dr. Thomas Gehrmann

Zürich, 2010

Zusammenfassung

Das Axino, der fermionische Superpartner des Axinos, ist ein guter Kandidat für kalte dunkle Materie falls, es das leichteste supersymmetrische Teilchen (LSP) ist. Da das Axino nur sehr schwach an Materiemultiplets koppelt, hat das nächst-leichteste supersymmetrische Teilchen (NLSP) eine lange Lebensdauer, was wichtige Konsequenzen sowohl für die Kosmologie als auch die Beschleunigerphysik hat. Unter der Annahme, dass ein geladenes Slepton das NLSP ist, werden die kompletten führenden Ein– und Zweischleifen–Korrekturen zu dessen Zerfall berechnet. Einschränkungen des Parameterraums, die sich aus der Kosmologie ergeben, werden im Detail analysiert, und es wird diskutiert, wie dieses Szenario an Teilchenbeschleunigern untersucht werden kann.

In diesem Zusammenhang wird die supersymmetrische Realisierung der KSVZ Axion–Erweiterung des Standardmodells untersucht. Die Zwei–, Drei– und Vier–Körper Zerfallsbreiten des Stau NLSPs werden mit der Methode der schwere–Masse Entwicklung berechnet. Unter Zuhilfenahme dieser Resultate wird untersucht, wie der Parameterraum des Modells eingeschränkt wird, basierend vor allem auf folgenden Effekten:

- Dichte der dunklen Materie, sowohl der aktuelle Wert als auch von Stau–Zerfällen abgeleitet;
- klein–Skalen Strukturen;
- katalysierte Big Bang Nukleosynthese;
- späte Energieinjektion.

Es wird gezeigt, dass die Stau Lebensdauer genügend gross sein kann, um primordiale gebundene Zustände zu erlauben, die zu katalysierter Big Bang Nukleosynthese (BBN) von ^{6}Li und ^{9}Be führen. Dies ergibt obere Schranken für die Peccei–Quinn Skala f_a, die wiederum von anderen Parametern des Modells abhängt. Unter Berücksichtigung von Effekten später Energiezufuhr werden hadronische und elektromagnetische BBN Einschränkungen untersucht. Der Vier–Körper Slepton Zerfall in ein Axino, ein Lepton, und ein Quark–Antiquark–Paar ist von Bedeutung in diesem Fall, da er die späte hadronische Energiezufuhr bestimmt. Daher werden die erhaltenen BBN Einschränkungen präsentiert, von denen gezeigt wird, dass sie stärkere Einschränkungen auf manche Regionen des Parameterraums liefern als diejenigen, die aus katalysierter BBN via Bindungszuständen von Sleptonen gewonnen werden. Diese BBN Einschränkungen auf hadronische Energieabgabe liefern neue obere Schranken für f_a. Zusätzlich

werden Einschränkungen durch die Dichte der dunklen Materie und BBN auf die Rückerhitzungstemperatur T_R untersucht. Für eine Masse des Axinos kompatibel mit Strukturen auf grossen Skalen, $m_{\widetilde{a}} \gtrsim 100\,\mathrm{keV}$, wird gezeigt, dass Temperaturen über $10^9\,\mathrm{GeV}$ erlaubt werden, falls $f_a > 3 \times 10^{12}\,\mathrm{GeV}$.

Des weiteren werden phänomenologische Merkmale von supersymmetrischen hadronischen Axion–Modellen an Teilchenbeschleunigern untersucht. Im Besonderen wird die Effektivität der Messung der Lebensdauer und der Masse des Staus und des Axinos am LHC und zukünftigen Linearbeschleunigern analysiert. Nur diejenigen Staus, die in Teilchenkollisionen produziert und im Anschluss im Detektor gefangen werden, werden für diese Studie benutzt. Es wird gezeigt, dass, obwohl die Masse des Staus auf ein Prozent genau gemessen werden kann, eine Bestimmung der Lebensdauer des Staus und der Masse des Axinos am LHC eine grosse Herausforderung darstellen würde.

Schliesslich wird untersucht, welche Schlussfolgerungen gezogen werden können, falls sowohl das Axino als auch das Gravitino leichter als das Stau wären. Dies kann eine an Beschleunigern schwer nachzuweisende Konfiguration darstellen, falls nicht genügend Statistik gesammelt werden kann oder die Massen der beiden Teilchen stark degeneriert sind. In diesem Szenario können einige restriktivere BBN Einschränkungen vermieden werden, während einige vormals bevorzugte Regionen des Parameterraums sich nun als benachteiligt herausstellen.

Abstract

The axino, the fermionic superpartner of the axion, is a well–motivated candidate for cold dark matter if it is the lightest supersymmetric particle (LSP). Since the axino couples very weakly to the matter multiplets, the next–to–lightest supersymmetric particle (NLSP) has a long lifetime, which has important consequences for both cosmology and collider phenomenology. Assuming that a charged slepton is the NLSP, the complete leading one– and two–loop contributions to its decay are calculated. The constraints on the parameter space from cosmology are analysed in detail and the means by which this scenario can be probed at colliders are discussed.

In this framework the supersymmetric realisation of the KSVZ axion extension to the standard model is studied. The 2–, 3– and 4–body decay widths of the stau NLSP are calculated using the method of heavy mass expansion. Using these results, constraints on the parameter space of the model are derived using the following cosmological effects:

- dark matter density, both the present value and from stau decays;
- small scale structure;
- catalysed big bang nucleosynthesis;
- late energy injection.

It is found that the stau lifetime can be sufficiently long to allow for primordial bound states, leading to catalysed big bang nucleosynthesis (BBN) of ^{6}Li and ^{9}Be. This yields upper limits on the Peccei–Quinn scale f_a that depend on other parameters of the model. Taking into account effects of late energy injection, the hadronic and electromagnetic BBN constraints are examined. The 4–body slepton decay into the axino, a lepton, and a quark–antiquark pair is important in this case since it governs late hadronic energy injection. Thus the obtained hadronic BBN constraints are presented, which are shown to be more restrictive than the ones associated with catalysed BBN via slepton–bound–state formation in some regions of parameter space. These BBN constraints on hadronic energy release provide new upper limits on f_a. Additionally, constraints on the reheating temperature T_{R} imposed by the dark matter density and by BBN are studied. For an axino mass compatible with large–scale structure, $m_{\tilde{a}} \gtrsim 100$ keV, it is shown that temperatures above $10^9\,\mathrm{GeV}$ become viable for $f_a > 3 \times 10^{12}\,\mathrm{GeV}$.

Furthermore, the phenomenological collider signatures of the supersymmetric hadronic axion model are studied. In particular the effectiveness of measuring the lifetime and

masses of the stau and axino at the LHC and future linear colliders are investigated. Only the staus that are produced in the particle collisions and are subsequently trapped in the detectors are utilised for this purpose. It is shown that although the stau mass can be measured to the percent level, a determination of the stau lifetime and axino mass would prove to be challenging for the LHC.

Finally the implications of having both the axino and the gravitino lighter than the stau are briefly considered. This can be a difficult configuration to resolve at colliders unless a large amount of statistics is gathered and the masses of the two particles are highly non–degenerate. In this scenario, some of the more restrictive BBN constraints can be evaded while some previously open regions of parameter space become disfavoured.

Contents

Introduction

There is compelling evidence suggesting phenomena beyond our understanding, motivating the study of models of physics beyond the standard model (SM). As the Large Hadron Collider (LHC) starts its operations and we delve ever higher in energy and ever smaller in scale, the first hints of this physics could well be seen soon. However, it is not only with high energy experiments that new scales can be explored, there are also cosmological considerations that can provide testing grounds for new models, or at least help to constrain them. In this thesis, both aspects are investigated in considering axino dark matter scenarios.

Research in the topics of particle physics and astrophysics are becoming increasingly intertwined. As the knowledge in these areas improves, so the questions become more complex. Interestingly, the studies of the largest known object, the universe, complement very well the studies of the smallest known objects, the fundamental particles. In particular, our understanding of how the universe was born can provide insights into the environments that had to have existed very early on. This in turn, helps to determine whether the current knowledge of particle physics can adequately explain and reproduce these environments.

The SM of particle physics provides a very successful description of physical reality at the most fundamental level of particle interactions. It is a quantum field theory based on the $SU(3)_C \times SU(2)_L \times U(1)_Y$ gauge symmetry group representing the strong [1–4], weak, and electromagnetic [5–7] interactions of particles. Precision experimental data collected over the past 25 years at the Tevatron and LEP colliders, as well as the B factories at KEKB and SLAC, agree with the predictions of the SM in almost all aspects to an unprecedented level. Indeed, the only particle left unobserved in the SM is the Higgs boson [8–12], the search for which is the main focus of the current highest energy experiment, the LHC. However, it is one of the largest omissions of the SM to not include gravity, classically described by General Relativity [13], as a quantum theory. This indicates that the SM is incomplete, at least at the scale of the reduced Planck mass $M_P = 2.4 \times 10^{18}\,\mathrm{GeV}$. It is at best only a very good approximation of the true, underlying model. Along with this stark omission, there are other, less obvious problems, such as the hierarchy problem [14–17]. One that is of particular interest in this thesis is the strong CP problem, which is discussed in more detail in the next

chapter.

In order to develop a more comprehensive theory of particle physics, one talks of physics beyond the standard model (BSM). In the studies of BSM physics, one of the most useful and increasingly important tools at hand is the constraints that can be inferred from cosmology and astrophysics. In fact, the most compelling evidence for the need for BSM comes from the discovery of the existence of dark matter (DM) [18]. This is matter that does not interact electromagnetically (hence the term 'dark') but makes up approximately 22% of the total energy content of the universe [19]. Current knowledge of cosmology and astrophysics can also be used to constrain BSM models. For example, BSM particles that existed in abundance in the early universe can significantly alter how the universe evolved to what is seen today, affecting the predictions of big bang nucleosynthesis (BBN). Thus the observations of the abundances of light nuclei can be used to limit the contributions from processes involving BSM particles and interactions. In this way the allowed parameter space of a particular BSM model can be significantly reduced.

One of the most extensively studied BSM scenario is supersymmetry (SUSY) (for an overview see for example, [20] and references therein). With R–parity conservation, the lightest supersymmetric particle (LSP) is stable and provides a natural candidate for dark matter. Combining a supersymmetric extension of the SM with the Peccei–Quinn (PQ) solution to the strong CP problem [21, 22], a very well–motivated dark matter candidate is obtained in the axino $\widetilde{a}$, the fermionic superpartner of the axion. A particularly interesting scenario which is explored in this thesis is one in which the next–to–lightest supersymmetric particle (NLSP) is a charged slepton.

In the next chapter, the theoretical foundations upon which the study relies is outlined. An explanation of the strong CP problem, followed by the PQ solution, is given in the first two sections. Then a brief outline of the model that is investigated in this thesis, the supersymmetric KSVZ model, is introduced. The relevant details of cosmology are given in the second half of this introductory chapter. A brief summary of the standard model of cosmology is given, followed by a section on the theory of big bang nucleosynthesis (BBN) and the possible effects of catalysis and late hadronic injection on the predictions of BBN.

The calculational details of the decay of the stau NLSP are given in Chapter 2 where the 2–, 3– and 4–body decays of the stau NLSP into the axino LSP are outlined and the lifetime of the stau is discussed. Then the cosmological implications of the model are investigated in Chapter 3, resulting in new and updated constraints on the parameter space of the axino model under investigation. In Chapter 4, the possible collider studies at current and future experiments are considered. Lastly, a scenario in which both the axino and the gravitino are lighter than the stau is briefly looked at. The conclusions are given at the end. Note that some of the work in this thesis was published in [23, 24] and some will be included in an upcoming publication.

Chapter 1

Overview

In this chapter an overview of the fundamental concepts that are important to the study carried out in this thesis is given. For ease of clarity, it is divided into two parts, with the first part focusing on particle physics and the second on cosmology. Both of these are very large topics in themselves and only the parts relevant to the thesis are discussed in detail. In the particle physics section, the first two subsections outline the strong CP problem and the PQ solution to the problem. Specifically, the supersymmetric KSVZ model of the axion is the model of interest and an outline of this model is given in the next subsection. The second part gives the cosmological setting of the study, starting with a brief summary of the standard model of cosmology. The subsequent subsections concentrate on the basics of BBN, catalysed BBN and late energy injection.

1.1 Particle Physics

As already mentioned in the introduction, the basis of the standard model of particle physics is an $SU(3)_C \times SU(2)_L \times U(1)_Y$ gauge theory. In this framework, ordinary matter is described by spin–1/2 fermions that are categorised into leptons and quarks while the fundamental forces are mediated by spin–1 gauge bosons. The quarks and leptons are further grouped into three generations which have exactly the same quantum numbers but vary increasingly in mass. $SU(3)_C$ is the basis of QCD, a theory of quarks in the framework of the strong interaction, which is mediated by gluons [1–4]. $SU(2)_L \times U(1)_Y$ describes the theory of the electroweak interactions [5–7]. The force is mediated by the photon, Z and $W^{\pm}$ bosons. Although the SM has been very well verified with experiments, there remain problems within the model, both theoretically and experimentally, that suggest physics beyond this model. The problem on which this thesis focuses is the strong CP problem, and a short description of it is given in the following subsection.

1.1.1 The Strong CP Problem

The strong CP problem arises as a consequence of two phenomena: the axial anomaly of the $U(1)_A$ current and the non–trivial structure of the QCD vacuum. Interestingly, both of these were invoked by 't Hooft [25] to solve the $U(1)_A$ problem. So let us first take a look at what is sometimes now known as the 'old $U(1)_A$ problem'.

In the limit of massless quarks, a 2–flavour QCD lagrangian takes the form

$$\mathcal{L}_{\mathrm{QCD}} = i\bar{q}\gamma_\mu D^\mu q - \frac{1}{4} G^a_{\mu\nu}\tilde{G}^{a,\mu\nu}, \tag{1.1}$$

where

$$q = \begin{pmatrix} u \\ d \end{pmatrix}, \tag{1.2}$$

is the quark field, with u and d representing the up– and down–type quarks, respectively. $D_\mu = \delta_\mu + ig_s t^a G^a_\mu$ is the covariant derivative, $g_s = \sqrt{\alpha_s 4\pi}$ is related to the strong coupling constant, $G^a_{\mu\nu} = \partial_\mu A^a_\nu - \partial_\nu A^a_\mu - g_s f^{abc} A^b_\mu A^c_\nu$ is the gluon field strength tensor and $\widetilde{G}^{a,\mu\nu} = \frac{1}{2}\epsilon^{\mu\nu\alpha\beta} G^a_{\alpha\beta}$ is its dual, where A^a_μ is the gluon field and f^{abc} is the structure constant of the group. The lagrangian has a global chiral $U(2)_L \times U(2)_R$ symmetry

$$\begin{pmatrix} u_L \\ d_L \end{pmatrix} \to U_L \begin{pmatrix} u_L \\ d_L \end{pmatrix}, \qquad \begin{pmatrix} u_R \\ d_R \end{pmatrix} \to U_R \begin{pmatrix} u_R \\ d_R \end{pmatrix}, \tag{1.3}$$

because of

$$\bar{q}\not{D}q = \bar{q}_L \not{D} q_L + \bar{q}_R \not{D} q_R, \tag{1.4}$$

where the subscript L and R labels the quark as either left– or right–handed. The symmetry can be decomposed into a vector $U(2)_V$ and an axial $U(2)_A$ part: $U(2)_V \times U(2)_A$. Due to the formation of a quark–antiquark condensate, this chiral symmetry is spontaneously broken into the vectorial symmetry $U(2)_V \equiv U(2)_{L+R}$, the subgroup of elements that transform with $U_L = U_R$. This is a symmetry of isospin times baryon number, which is realised exactly in nature $U(2)_V = SU(2)_I \times U(1)_B$. The condensate that forms is analogous to the electron pair condensate found in the ground state of superconductors. Because of the strong attractive force between quarks and antiquarks, they easily form quark–antiquark pairs, which exist as a Bose–Einstein condensate in the QCD vacuum. The pairs are formed between left–handed quarks and antiparticles of right–handed quarks in order to preserve parity and have zero total and angular momenta. As a result, the helicities of the quarks are mixed up and the vacuum acquires a non–zero expectation value

$$\langle 0|\overline{Q}Q|0\rangle = \langle 0|\overline{Q}_{\mathrm{L}} Q_{\mathrm{R}} + \overline{Q}_{\mathrm{R}} Q_{\mathrm{L}}|0\rangle \neq 0, \tag{1.5}$$

which spontaneously breaks the chiral symmetry of the theory.

According to Goldstone [26], the four broken generators associated with the broken set of orthogonal axial transformations, which can be denoted by $U(2)_A = SU(2)_A \times U(1)_A$, should give four massless Nambu–Goldstone bosons. As the u and d quarks are in fact not massless but have small masses, these pseudoscalar states are expected to also be light instead of massless. Three of these goldstone bosons can be identified as the isotriplet of the lightest mesons, the pions, associated with the broken $SU(2)_A$ symmetry. However, the fourth goldstone boson, associated with the $U(1)_A$ current

$$j_\mu^A = \sum_a \bar{q}_a \gamma_\mu \gamma_5 q_a \ , \tag{1.6}$$

is more problematic. The closest candidate is η (or η' if the s quark is also considered light) with a mass of $m_\eta = 548\,\mathrm{MeV}$ [27], which is far heavier than the pions. This contradicts the prediction from Weinberg [28], calculated using current algebra, that places an upper bound on the mass $m_\eta \leq \sqrt{3} m_\pi \approx 255\,\mathrm{MeV}$.

In 1976, 't Hooft solved this problem by invoking the combination of the axial anomaly and a more complicated structure to the QCD vacuum than what is expected from naive perturbative gauge theory [25]. The axial anomaly violates the conservation of the associated current, thus explicitly breaking the axial symmetry. In the massless quark limit, the non–conservation of the axial current can be written as

$$\partial_\mu j^{\mu A} \propto \frac{g_s^2}{32\pi^2} G^a_{\mu\nu} \widetilde{G}^{a,\mu\nu}. \tag{1.7}$$

Note that the above expression can be written as a total derivative

$$G^a_{\mu\nu} \widetilde{G}^{a,\mu\nu} = \partial_\mu K^\mu, \tag{1.8}$$

where

$$K^\mu = \epsilon^{\mu\nu\alpha\beta} \left(A^a_\nu G^a_{\alpha\beta} - \frac{g_s}{3} f^{abc} A^a_\nu A^b_\alpha A^c_\beta \right). \tag{1.9}$$

The current can thus be redefined in a way such that it is always conserved, so that the axial anomaly cannot by itself solve the $U(1)_A$ problem. What 't Hooft noticed was that the then recently discovered instanton solutions* to QCD [29] brought with them quantum effects that lead to $G\widetilde{G}$ being non–vanishing, i.e. the current is not conserved, where the simplified notation $G\widetilde{G} \equiv G^a_{\mu\nu} \widetilde{G}^{a,\mu\nu}$ is now used. This means that the $U(1)_A$ symmetry is broken by nonperturbative effects and is in fact not a symmetry of QCD after all. Thus there is no Goldstone boson coupled to the physical $U(1)_A$ current, and in principle, no $U(1)_A$ problem. Note that although the instanton solutions apply to

*Instantons are classical localised solutions of the field equations in Euclidean space–time.

all non–Abelian gauge theories, there is not a similar problem in the weak sector of the SM. In the weak theory, there is no corresponding non-vanishing $U(1)$ anomaly and thus the $F\widetilde{F} \equiv F_{\mu\nu}\widetilde{F}^{\mu\nu}$ term, where $F_{\mu\nu}$ is the electroweak field strength tensor and $\widetilde{F}^{\mu\nu}$ is its dual, that appears in the electroweak lagrangian does not have any physical meaning.

In solving this problem, 't Hooft introduced a different one by assigning a non–trivial vacuum to QCD. Instantons allow tunnelling between different vacua $|n\rangle$, labelled by a winding number n. Hence the true QCD vacuum is a gauge–invariant superposition of all the vacua

$$|\theta\rangle = \sum_n e^{-in\theta}|n\rangle. \tag{1.10}$$

Evidently, the theory depends on θ, and the effects of the instantons can be included by adding a theta term to the QCD lagrangian

$$\mathcal{L}^{\theta}_{\text{QCD}} = \cdots + \theta\frac{g_s^2}{32\pi^2}G\widetilde{G}. \tag{1.11}$$

Where before this theta term was ignored because the gluon fields A_μ were thought to vanish at infinity, this is not actually true due to the instanton solutions. In the massless limit of QCD, a chiral transformation to the quark fields can be applied such that any choice of θ leads to the same physics. However, in massive QCD, the different θ values place us in different vacua, which has a physical, observable effect.

The theta term is CP–violating and would manifest itself most strongly in the neutron electric dipole moment, on which experiments place a very strict bound leading to $|\theta| \leq 10^{-9}$†. This in itself is not such a problem, as it can certainly be argued that θ is zero. However, when the electroweak interactions are included, the mass term in the lagrangian must be dealt with, where M is the complex quark mass matrix

$$\mathcal{L}_{\text{mass}} = \bar{q}_{iR}M_{ij}q_{jL} + \text{h.c.}. \tag{1.12}$$

To go to a physical basis, a a chiral rotation is performed to make M real and diagonal. This then causes a shift in θ

$$\bar{\theta} = \theta_{QCD} + \arg\,\det M. \tag{1.13}$$

Now, not only is a very small CP violation in QCD needed, this fact needs to come from the cancellation of two terms that are, a priori, unrelated to each other. This is the strong CP problem.

†This bound has taken the perturbative effects, coming from loop corrections, into account such that this is a bound purely on the nonperturbative contributions.

There have been a number of solutions proposed to solve this problem. The simplest one is the possibility of having a massless u–quark [30], which would obtain its small mass through radiative corrections and instanton effects. This would allow for a redefinition of the u–quark field that would make the theta term vanish. This possibility is almost completely ruled out, but still has a few proponents. Another way of solving the problem is by claiming CP invariance as a property of an underlying, more fundamental theory, which then requires the electroweak CP violation to come from a spontaneously broken symmetry [31–35]. $\bar{\theta}$ would then be calculable and very small. Finally, there is a dynamical approach to solving the problem, and this is the solution that is focused on hereafter. In this approach, the theta parameter is promoted to a field and dynamically set to zero, or a very small value. The most famous and elegant solution in this category is the Peccei–Quinn mechanism [21,22], which produces a light pseudoscalar called the axion [36,37].

1.1.2 Peccei–Quinn Mechanism and the Axion

As a way of dynamically setting $\bar{\theta}$ to zero, Peccei and Quinn [21,22] introduced a global chiral $U(1)_{\mathrm{PQ}}$ symmetry which is spontaneously broken to give a pseudoscalar, known as the axion [36,37]. The original idea behind this PQ mechanism was to imitate the solution of the massless u–quark scenario, so a brief outline of what happens if the u–quark is massless is useful here.

A chiral transformation of the quark fields can be carried out

$$q \rightarrow e^{i\gamma_5\alpha}q, \tag{1.14}$$

where α is a transformation parameter, which leads to the following relevant terms in the QCD lagrangian

$$\mathcal{L}_{\mathrm{QCD}} = ... - m\bar{q}q + \frac{\theta}{32\pi^2}G\widetilde{G}, \tag{1.15}$$

to transform in the following way

$$\mathcal{L}'_{\mathrm{QCD}} = ... - m\bar{q}e^{2i\gamma_5\alpha}q + \frac{\theta - 2\alpha}{32\pi^2}G\widetilde{G}. \tag{1.16}$$

For $m = 0$, this is equivalent to a shift symmetry of $\theta \rightarrow \theta - 2\alpha$, which means that θ is rendered unphysical and there is no strong CP problem.

However, as mentioned in the previous section, the current consensus is that the u–quark has a non–zero mass. Instead, in order to solve the strong CP problem, Peccei and Quinn required two Higgs doublets, with H_u giving mass to the up–type quark and H_d to the down–type quark. Under the PQ symmetry, these fields undergo the following transformations

$$q \rightarrow e^{i\gamma_5\alpha}q \ , \qquad \{H_u, H_d\} \rightarrow e^{i\beta}\{H_u, H_d\} \ , \tag{1.17}$$

where α and β are the transformation parameters. This leads to the lagrangian transforming as such

$$\begin{aligned}\mathcal{L} &= (\bar{q}_L H_u u_R + \bar{q}_L H_d d_R + \text{h.c.}) - V(H_u, H_d) + \frac{\theta}{32\pi^2} G\widetilde{G} \\ &\rightarrow \mathcal{L}' = (e^{i(\beta-\alpha)} \bar{q}_L H_u u_R + e^{i(\beta-\alpha)} \bar{q}_L H_d d_R + \text{h.c.}) - V(H_u, H_d) + (\theta - 2\alpha) \frac{\theta}{32\pi^2} G\widetilde{G}.\end{aligned} \tag{1.18}$$

Note that $V(H_u, H_d)$ must be invariant under this transformation. For $\alpha = \beta$, the massless u–quark scenario is approximately recovered, where the lagrangian is invariant under the shift $\theta \rightarrow \theta - 2\alpha$, such that θ is only a phase of the PQ transformation.

However, the PQ symmetry is spontaneously broken by the Higgs vacuum expectation values (VEVs), leading to the appearance of the axion a, in accordance with Goldstone's theorem [26]. Under the $U(1)_{\text{PQ}}$ symmetry, the axion field transforms as

$$a(x) \rightarrow a(x) + \alpha f_a, \tag{1.19}$$

where f_a is the PQ symmetry breaking scale. As a Goldstone boson, the axion field appears in the lagrangian only in derivative terms. Due to the axial anomaly [38–40] however, it also enters via a linear coupling with the anomaly

$$\mathcal{L}_{\text{axion}} = (\partial_\mu a)^2 + \frac{a(x)}{f_a} \frac{g_s^2}{32\pi^2} G\widetilde{G}. \tag{1.20}$$

The anomalous term, the second term on the right hand side in the above equation, acts as a potential for the axion field. The minimum of the axion field effective potential occurs at $\langle a \rangle = -\bar{\theta} f_a / N$, where N is the colour anomaly of the PQ symmetry whose value is model–dependent. Replacing the axion field in the lagrangian by its physical field $a_{\text{phys}} = a - \langle a \rangle$, the CP–violating theta term is replaced by the CP–conserving coupling of the dynamical field of the axion to the gluonic pseudoscalar density. It has been shown [41] that this term preferably relaxes to its minimum, at $\bar{\theta} = 0$. This is the PQ solution to the strong CP problem.

The axion acquires a mass through the above–mentioned axial anomaly and QCD instanton effects and at low energies its mass m_a can be approximated by [42]

$$m_a^2 \approx \frac{m_u m_d}{(m_u + m_d)^2} \left(\frac{f_\pi m_\pi}{f_a / N} \right)^2, \tag{1.21}$$

where m_u and m_d are the masses of the up and down quarks, respectively, f_π is the decay constant of the pion and m_π is the mass of the pion.

Unfortunately, less than one year after the proposal of this solution, the original Peccei–Quinn–Weinberg–Wilczek (PQWW) axion, so–called because it was Weinberg

[36] and Wilczek [37] who first examined the pseudoscalar that resulted from the broken PQ symmetry, was experimentally ruled out [43]. The theory assumes that the scale at which the PQ symmetry breaks down is the weak scale. There is in fact no fundamental reason to constrain f_a to this scale and the PQ symmetry can be broken at a much higher energy. With a higher f_a and a requirement that there is no direct tree–level couplings between the axion and the SM fermions, the experimental bounds can be evaded. Indeed, one now speaks of an "invisible axion", whose couplings to SM particles are extremely suppressed.

The mechanism of the invisible axion models remains the same as the original PQ mechanism. However, most of the models introduce a new complex scalar field ϕ, usually an $SU(2) \times U(1)$ singlet that is charged under $U(1)_{\mathrm{PQ}}$, which acquires a large vacuum expectation value. These properties allow the PQ symmetry to be broken at a scale much larger than the weak scale, thus suppressing the axion interactions, which are proportional to $1/f_a$, and reducing its mass. As a result, the axion couplings to the SM particles can vary greatly to the original PQWW axion.

There exist two main general types of invisible axion models: the Kim–Shifman–Vainshtein–Zakharov (KSVZ) model and the Dine–Fischler–Srednicki–Zhitnitskii (DFSZ) model. In the DFSZ model [44, 45], there are similarly two Higgs doublets, but additionally, the quarks and leptons carry a PQ charge. In this model, there is no direct fermion–ϕ coupling and the fermions only feel the PQ breaking through the Higgs potential. The KSVZ (or equivalently, hadronic) model [46, 47] requires only one Higgs doublet but introduces new heavy quarks. Only these new quarks and the scalar ϕ are then charged under $U(1)_{\mathrm{PQ}}$.

There are many variants on these two models, and in this thesis the KSVZ or hadronic axion type models are considered. Following very closely the paper from Shifman, Vainshtein and Zakharov [47], the important points of the model are summarised here.

First, the unbroken $U(1)_{\mathrm{PQ}}$ case is looked at. Denoting the heavy quark by Q, the following terms in the lagrangian are obtained for the new interactions in the model

$$\mathcal{L}_{\mathrm{KSVZ}} = \bar{Q} i \not{\partial} Q - y(\phi \bar{Q}_R Q_L + \phi^\dagger \bar{Q}_L Q_R) + (\partial_\mu \phi^\dagger)(\partial_\mu \phi) - V(\phi), \tag{1.22}$$

where y is a Yukawa coupling and

$$V(\phi) = -m^2 \phi^\dagger \phi + \lambda (\phi^\dagger \phi)^2, \tag{1.23}$$

is the potential of the new ϕ field, which acquires a non–zero vacuum expectation value

$$\langle \phi \rangle = \phi_0 \equiv \frac{f_a}{\sqrt{2}} = \frac{m}{\sqrt{2\lambda}}. \tag{1.24}$$

Expanding ϕ around its VEV

$$\phi(x) = \phi_0 + \frac{1}{\sqrt{2}} \left[\phi_1(x) + i \phi_2(x) \right], \tag{1.25}$$

and substituting this back into the potential $V(\phi)$ in (1.23) shows that the lagrangian describes a scalar state, the saxion $\phi_1(x)$ with mass $m\sqrt{2}$ and a pseudoscalar state, the axion $\phi_2(x)$ with zero mass in the classical approximation. The mass of the saxion is often taken to be very large such that its effects can be neglected and this is the approach taken in this thesis.

The PQ symmetry is of course broken by instanton effects through the axial anomaly. This produces a $aG\widetilde{G}$ term that has been discussed in the context of the original PQWW axion model above and solves the strong CP problem in the same way. This happens at $T \approx \Lambda_{QCD}$, causing the mexican hat axion potential $V(\phi)$ to be tilted, hence giving the axion a non–zero mass.

There are some constraints that can be placed on the axion mass, and by relation, the PQ scale f_a, depending on the early history of the universe and also the specifics of the model. For small f_a, the axions were in thermal equilibrium with the hot primordial plasma and decoupled as a hot relic. Requiring that its relic density is not larger than that of the present day dark matter density $\Omega_a \leq \Omega_{\rm dm}$ leads to a limit on its mass $m_a \lesssim 1\,\text{eV}$, which places it in the category of hot dark matter. As a result, constraints from large scale structure (LSS) then requires that these axions not make up a dominant part of the dark matter density. For larger f_a, the axions were never in thermal equilibrium and their relic density Ω_a is governed by the initial misalignment angle Θ_i of the axion field with respect to the CP–conserving position, see for example [48–50] and references therein. It behaves as a condensate and can be categorised as cold dark matter. With a sufficiently small Θ_i being an option, $\Omega_a \ll \Omega_{\rm dm}$ is possible even for f_a as large as $10^{16}\,\text{GeV}$. Further details on the the cosmology aspect of the above discussion can be found in Sec. 1.2 and Chapter 3.

Experiments searching for axions have been around since their first inception over 30 years ago. The first experiments that were responsible for ruling out the original PQWW axion, where the PQ scale was set to around the weak scale, studied the decays of K^+, J/ψ and Υ [51–57]. Present day experiments search for the so–called invisible axions [58]. These experiments can roughly be divided into three categories.

Direct searches of galactic halo look for cold dark matter axions (with mass range μeV to meV) by using microwave cavities to resonantly convert the axions into photons in a reverse Primakoff process [59]. These photons can then be detected as an excess in the cavity power output. This search is sensitive to the axion mass m_a as well as its distribution in the galactic halo. The latest experiment of this type is the axion dark matter experiment (ADMX) [60,61], which provides exclusion limits on the axion mass in the preferred f_a range. In addition, cosmic axions can be indirectly searched for by looking for photons from $a \to \gamma\gamma$ decays, which probe axions with masses in the $\mathcal{O}(\text{eV})$ range.

Another type of search being carried out is of axions produced in the core of the sun. These solar axion searches probe axions with $10^{-5}\text{eV} < m_a < 1\text{eV}$ (warm or hot dark matter that decoupled from the primordial plasma as thermal relics) and

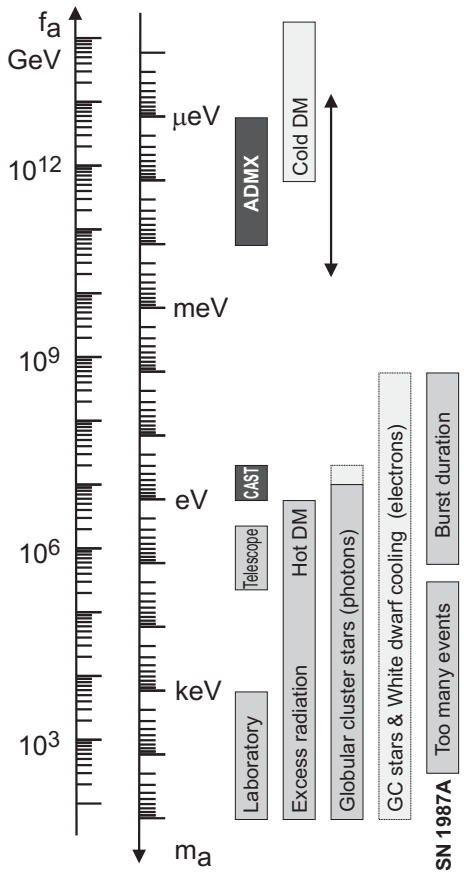

Figure 1.1: A summary of the astrophysical and cosmological constraints on f_a and m_a taken from [66]. The black bars illustrate the sensitivity ranges of the respective experiments as indicated.

use electromagnetic fields in axion helioscopes to convert the axions into photons that can be detected and analysed. The experiments currently carrying out this type of search include CERN Axion Solar Telescope (CAST) [62, 63] and the Tokyo Axion Helioscope [64].

At the same time, laboratory searches try to produce axions in a variety of experiments. One example of these is the 'shining light through a wall' experiment [65]. The experiment uses a polarised laser beam in a transverse magnetic field to convert photons from the laser into axions that will then travel through a wall and be converted back into photons that can be detected.

These experiments are starting to probe a larger parameter space than before. However, the best constraints on axion physics currently come from astrophysical and cosmological considerations. These are summarised in Fig. 1.1, which is taken from the review [66]. The black bars for the experiments denote the range which the respective experiments probe. The strongest lower limit comes from the observed burst duration

of supernova SN 1987A. In the very hot and dense medium of the supernova, axions can be produced and emitted, carrying energy away from the star. This would provide an additional means by which the supernova can cool down and thus reduce the burst duration of SN 1987A. Consequently a lower limit on f_a is obtained [66]

$$f_a/N \gtrsim 6 \times 10^8\,\mathrm{GeV}. \tag{1.26}$$

An upper limit on f_a can also be derived by imposing the condition of avoiding over-closure of the universe due to an overabundance of axions. However, this upper limit relies on the value of the initial misalignment angle Θ_i. When this is taken to be of a natural value ~ 1, this limit would be $f_a \lesssim 10^{12}\,\mathrm{GeV}$. But when this constraint is relaxed, the upper limit can be raised to as high as $f_a \lesssim 10^{16}\,\mathrm{GeV}$.

1.1.3 Supersymmetric KSVZ Model

In this thesis, the supersymmetric extension of the KSVZ model, first discussed in detail in [67–70], is of particular interest. This is the Minimal Supersymmetric Model (MSSM) with the Peccei–Quinn symmetry embedded in it, which introduces new heavy quark superfields that couple to the axion superfield. Only these new (s)quarks, the axion a and its superpartner the axino $\widetilde{a}$ are charged under $U(1)_{\mathrm{PQ}}$. A scenario with only one additional quark field Q, which is an SU(3) triplet and SU(2) singlet, with electrical charge e_Q and hypercharge $e_Y = e_Q$, is considered. The colour anomaly obtained with this model is $N = 1$. Using 2–component notation, the chiral multiplets of the new particles are given by

$$\begin{aligned} \text{Axion}: \quad & \Phi = \phi + \sqrt{2}\chi\theta + \mathrm{F}_\Phi\theta\theta, \\ \text{KSVZ Quarks}: \quad & Q_1 = \widetilde{Q}_1 + \sqrt{2}q_1\theta + \mathrm{F}_1\theta\theta, \\ & Q_2 = \widetilde{Q}_2 + \sqrt{2}q_2\theta + \mathrm{F}_2\theta\theta, \end{aligned} \tag{1.27}$$

where θ is the Grassman variable and F_i are auxiliary fields.

The interaction between the axino supermultiplet Φ and the heavy KSVZ quark supermultiplets $Q_{1,2}$ is specified by the following superpotential

$$W_{\mathrm{PQ}} = y\Phi Q_1 Q_2, \tag{1.28}$$

where y is the Yukawa coupling. The quantum numbers of the multiplets are summarised in Table 1.1. From the 2–component fields notation above, the 4–component fields describing the axino and the heavy KSVZ quark are given, respectively, by

$$\widetilde{a} = \begin{pmatrix} \chi \\ \bar{\chi} \end{pmatrix} \quad \text{and} \quad Q = \begin{pmatrix} q_1 \\ \bar{q}_2 \end{pmatrix}. \tag{1.29}$$

Chiral multiplet	$\mathrm{U(1)_{PQ}}$	$(\mathrm{SU(3)_c}, \mathrm{SU(2)_L})_\mathrm{Y}$
$\Phi = \phi + \sqrt{2}\chi\theta + F_\Phi\theta\theta$	+1	$(\mathbf{1},\mathbf{1})_0$
$Q_1 = \widetilde{Q}_1 + \sqrt{2}q_1\theta + F_1\theta\theta$	-1/2	$(\mathbf{3},\mathbf{1})_{+e_Q}$
$Q_2 = \widetilde{Q}_2 + \sqrt{2}q_2\theta + F_2\theta\theta$	-1/2	$(\mathbf{3}^*,\mathbf{1})_{-e_Q}$

Table 1.1: The axion multiplet Φ, the heavy KSVZ quark multiplets $Q_{1,2}$, and the associated quantum numbers considered in this work.

For the heavy KSVZ (s)quark masses, the SUSY limit

$$m_Q = m_{\tilde{Q}_{1,2}} = y\, f_a/\sqrt{2}, \tag{1.30}$$

is used, with both y and f_a taken to be real by field redefinitions. The astrophysical limit on the value of f_a discussed in the previous section $f_a \gtrsim 6\times10^8\,\mathrm{GeV}$ then implies a large hierarchy between the mass of the new (s)quark and the soft SUSY mass scale

$$m_{Q,\tilde{Q}_{1,2}} \gg m_Z, m_\mathrm{SUSY}, \tag{1.31}$$

for $y = \mathcal{O}(1)$.

The axion and axino interactions are briefly recalled to clarify the definition of $f_a = \sqrt{2}\langle\phi\rangle$ in the considered model. By integrating out the heavy KSVZ (s)quarks, axion–gluon and axion–photon interactions are obtained as described by the effective Lagrangians

$$\mathcal{L}_{agg} = \frac{g_\mathrm{s}^2}{32\pi^2 f_a}\, a\, G\widetilde{G}, \tag{1.32}$$

$$\mathcal{L}_{a\gamma\gamma} = \frac{e^2 C_{a\gamma\gamma}}{32\pi^2 f_a}\, a\, F\widetilde{F}, \tag{1.33}$$

with $e^2 = 4\pi\alpha$. After chiral symmetry breaking,

$$C_{a\gamma\gamma} = 6e_Q^2 - \frac{2}{3}\frac{4+z}{1+z}, \tag{1.34}$$

for the models described by (1.28) and (1.27), where $z = m_u/m_d \simeq 0.56$ denotes the ratio of the up and down quark masses. The corresponding interactions of axinos with gluons and gluinos $\tilde{g}$ are obtained as described by

$$\mathcal{L}_{\tilde{a}\tilde{g}g} = i\,\frac{g_\mathrm{s}^2}{64\pi^2 f_a}\,\bar{\tilde{a}}\,\gamma_5\,[\gamma^\mu,\gamma^\nu]\;\tilde{g}^a\,G^a_{\mu\nu}. \tag{1.35}$$

An attractive realisation of this supersymmetric KSVZ model with conserved R–parity has the axino $\widetilde{a}$ as the LSP and a charged slepton $\tilde{l}$ as the NLSP. Since the

axino LSP allows for a long–lived charged slepton which should be easy to discover at the LHC, those scenarios are appealing not only from a theoretical but also from a phenomenological point of view.

While the study presented in this thesis can easily be generalised, the focus here is on the case in which the NLSP is a purely right–chiral lighter stau, $\widetilde{\tau}_1 = \widetilde{\tau}_\mathrm{R}$, which is a good approximation at least for small $\tan\beta$. Its coupling to neutralinos is then dominated by the bino coupling. For further simplicity, it is assumed that mixing in the neutralino sector is such that one of the neutralino states is an (almost) pure bino $\widetilde{B}$. In fact, the cosmological considerations given in the study rely on a spectrum in which that state is the lightest neutralino, $\widetilde{\chi}_1^0 = \widetilde{B}$, while the results for the $\widetilde{\tau}_\mathrm{R}$ decays are not restricted to this case. The axino mass $m_{\widetilde{a}}$ is treated as a free parameter which is bounded from above by the stau NLSP mass $m_{\widetilde{\tau}}$.

Axions and saxions are also integral parts of the physics of an axino dark matter scenario. As noted for instance by Kim [71–73], the decays of the saxion could lead to significant entropy production reheating the universe, thereby changing the allowed mass range for the axion [71–74]. For the present investigation it is assumed that the saxion mass is such that saxion effects are negligible.

1.2 Cosmology

In this section the standard model of cosmology is briefly outlined, which sets the framework within which the cosmological constraints are derived on the hadronic axion model. In order to facilitate explanation, the workings of big bang nucleosynthesis in the early universe and the possible effects of catalysis and late energy injection on this nucleosynthesis are described in further detail.

1.2.1 ΛCDM Model

The current standard model of cosmology was developed in several stages and is now known as the Lambda–Cold Dark Matter (ΛCDM) model. The ΛCDM model is the simplest model that successfully explains the cosmic microwave background (CMB), large scale structure (LSS), the accelerating expansion of the universe and the primordial abundances of light elements. It is a modern version of the original hot big bang theory, which was first proposed by Lemaitre in 1931, then known as the "hypothesis of the primeval atom". The ΛCDM model is built upon two central ideas, general relativity and the cosmological principle, which states that on a large enough scale, the universe is homogeneous and isotropic. It consists of an early, very hot and dense state, from which the universe as it is known today evolved. The aftermath of this initial state exists today as a 'glow' of photon radiation known as the CMB radiation. This was predicted in the 1940s by Gamow, Alpher and Herman, when they further developed

the big bang theory, and was first experimentally detected in 1965 [75]. This, along with the determination that the CMB has an almost perfect blackbody spectrum was an important affirmation of the hot big bang theory. It has since been measured to great accuracy by the Wilkinson Microwave Anisotropy Probe (WMAP) satellite, putting the photonic temperature of the universe at $T \approx 2.73\,\mathrm{K}$ and showing fluctuations of the order 10^{-5} [19].

A homogeneous spacetime can be described by the Friedmann–Lemaitre–Robertson–Walker (FLRW) metric

$$\mathrm{d}s^2 = \mathrm{d}t^2 - a^2(t)\left[\frac{\mathrm{d}r^2}{1-kr^2} + r^2\left(\mathrm{d}\theta^2 + \sin^2\theta\,\mathrm{d}\phi^2\right)\right], \tag{1.36}$$

where $a(t)$ is the cosmic scale factor and k is the curvature of the universe. The present day value for the scale factor $a(t_0) \equiv a_0$ is normalised to 1. With the right parameterisation, the curvature can be discretised into three values, $k = -1$ for open, $k = 1$ for closed and $k = 0$ for spatially flat geometries. Observational evidence points towards a universe that is almost perfectly flat [19]. Friedmann used this metric to solve Einstein's field equations

$$G_{\mu\nu} = 8\pi G_N T_{\mu\nu}, \tag{1.37}$$

where $G_{\mu\nu}$ is the Einstein tensor, G_N is the Newtonian gravitational constant and $T_{\mu\nu}$ is the stress–energy tensor. This leads to what are now known as the Friedmann equations

$$3\left(\frac{\dot{a}}{a}\right)^2 + \frac{3k}{a^2} = 8\pi G_N \rho, \tag{1.38}$$

$$2\frac{\ddot{a}}{a} + \left(\frac{\dot{a}}{a}\right)^2 + \frac{k}{a^2} = -8\pi G_N p, \tag{1.39}$$

where ρ is the total energy density and p is the total isotropic pressure, both of which include contributions from matter, radiation and the cosmological constant Λ. These equations form the governing basis of the ΛCDM theory and describe the evolution of the universe. They were also one of the earliest indications of a non–static universe. Through this Friedmann showed that the expansion of the universe is in fact a natural outcome of combining general relativity and the cosmological principle. Furthermore, the two Friedmann equations can be combined to lead to another important equation that is independent of the curvature factor, describing the acceleration of the cosmic scale

$$\frac{\ddot{a}}{a} = -\frac{4\pi G_N}{3}\left(\rho + 3p\right). \tag{1.40}$$

Although earlier observations had shown extragalactic objects moving away from us, it was not until 1929 when Hubble carried out a systematic and thorough study of the

redshifts of galaxies, that the expansion of the universe was experimentally established [76, 77]. In a relation now known as Hubble's law, it was shown that these objects are receding away from us, and that the farther away they are from us, the faster they are receding. This confirms the expectation from the cosmological principle and leads to the verification that the universe is undergoing an accelerating expansion. The expansion can be described using the Hubble parameter, defined as $H(t) \equiv \dot{a}(t)/a(t)$, with Hubble's law given by

$$v = H_0 D, \tag{1.41}$$

where v is the recessional velocity of the galaxy, H_0 is the Hubble parameter at the time of observation and D is the proper distance of the galaxy from us. This expansion is accounted for by Λ, a cosmological constant that describes a form of energy with a large negative pressure, called dark energy.

The model, when fitted to observational data, allows for the energy content of the universe to be calculated. Using data from the CMB and type 1a supernovae, the different contributions to the energy density can be derived [19]. Baryonic matter, with which we are very familiar, makes up less than 5% of the energy content. Instead, 22% of the total energy (or over 80% of the total matter content) resides in non–baryonic collisionless matter, termed dark matter (DM), whose identity is yet unknown. The rest of the energy content, 73%, is made up of dark energy. It is believed that we are in an era where this dark energy is dominating the evolution of the universe and is thus driving the accelerating expansion against the collapsing forces of gravity.

By rewriting the Friedmann equations, a critical density can be defined for $k = 0$

$$\rho_{\rm c} \equiv \frac{3H^2}{8\pi G_N}, \tag{1.42}$$

and can be used to define the cosmological density parameter

$$\Omega \equiv \frac{\rho_{\rm tot}}{\rho_c}, \tag{1.43}$$

where $\rho_{\rm tot}$ is the total energy density of the universe. This parameterisation is also used for the individual components of the energy density

$$\Omega_i \equiv \frac{\rho_i}{\rho_c}. \tag{1.44}$$

The total density parameter Ω has a direct relation to the curvature factor k, thus making a link between the total energy density and the geometrical shape of the universe. $\Omega = 1$ corresponds to the flat universe that we believe we are living in while $\Omega > 1$ corresponds to a closed universe and $\Omega < 1$ corresponds to an open universe.

Although the universe can be described as homogeneous and isotropic, observations and the anisotropies of the CMB show that there exists structure on smaller scales. The explanation for these structures is simple. Gravitational forces act on initially small, adiabatic Gaussian density fluctuations that originate from the inflationary era. This results in a bottom–up hierarchy of structures forming, in agreement with known observational data. To account for the sizes and ages of observed objects, the structure formation had to have started before baryonic matter decoupled from the thermal bath. This is one of the reasons for requiring DM to be weakly interacting, such that it decouples much earlier than baryonic matter. LSS observed in the universe demands this DM to be cold, although warm dark matter, or at least components of warm dark matter, is not yet ruled out.

The categorisation of dark matter as cold, warm or hot is not very well–defined but can be treated in terms of how it affects structure formation. If the DM was initially in thermal equilibrium with the primordial plasma, cold DM is defined as matter that decoupled from the thermal bath and started seeding structure very early in the history of the universe, forming small objects that gravitationally grew into larger ones. Hot DM on the other hand, decoupled while relativistic such that its free–streaming in the early universe erased a lot of structure on scales comparable to its free–streaming length and smaller. Objects formed early on would thus form only on very large scales and would subsequently fragment into smaller objects, leading to a top–down hierarchy. Warm DM lies somewhere in between cold and hot. It can lead to an erasure of some small scale structures while maintaining the bottom–up hierarchy of structure formation that is supported by observational data. However, the DM does not have to have been in thermal equilibrium. As will be explored in this thesis, DM produced from the thermal scatterings of particles that were in thermal equilibrium or DM resulting from out–of–equilibrium decays can also, in principle, constitute all three types of dark matter. Again, the discerning feature that categorises the DM as cold, warm or hot is the manner in which they affect structure formation.

The big bang theory described how the universe evolves and why, but did not explain the initial conditions required to obtain such a model, for example homogeneity. An inflationary epoch right after the initial big bang was proposed to solve the problem of the initial conditions. During inflation, the universe underwent an exponential expansion, believed to be driven by vacuum energy, the same energy that is driving the expansion now. There are many models of inflation currently being theorised, with experimental verification being still years away, but it is an accepted part of modern cosmology and the ΛCDM model.

Another important aspect of the ΛCDM model is the theory of nucleosynthesis. In the first few minutes after the big bang, nucleosynthesis takes place, producing light elements that can still be detected today. Collectively known as big bang nucleosynthesis, the predictions of the abundances of primordial D, ^{3}He, ^{4}He and ^{7}Li in this framework depends on only one parameter, the baryon–to–photon ratio $\eta \equiv n_b/n_\gamma$.

This ratio has been measured to great accuracy and has verified the predictions of BBN with the observationally inferred primordial abundances of the light elements, proving to be another great success of the ΛCDM model.

1.2.2 Standard BBN

Big bang nucleosynthesis refers to the synthesis of light elements that started in the early period of the universe, at $T \sim 1\,\mathrm{MeV}$ or equivalently, $t \sim 1\,\mathrm{s}$. This is the highest temperature that has been experimentally verified to have existed in the history of the universe. The theory of BBN provides theoretical predictions of primordial abundances of light elements such as D, ^{3}He, ^{4}He and ^{7}Li that have been shown to be in good agreement with the primordial abundances inferred from observations. Elements heavier than beryllium were formed later, in stellar processes. This allows constraints to be placed on the physical conditions that had to have existed during the times of BBN. As the predictions of the primordial abundances are very sensitive to these early conditions, BBN can by extension also be used to place constraints on BSM physics that might significantly alter the BBN predictions, see for example [78] and references therein.

The details of BBN theory have been covered in great detail in the literature. Only a brief summary is provided here of the essence of the processes. At temperatures $T \gtrsim 1\,\mathrm{MeV}$, the weak interactions of neutron–proton interconversion are in thermal equilibrium,

$$\begin{aligned} n &\rightleftharpoons p + e^- + \bar{\nu}_e, \\ \nu_e + n &\rightleftharpoons p + e^-, \\ e^+ + n &\rightleftharpoons p + \bar{\nu}_e, \end{aligned} \tag{1.45}$$

thus fixing the neutron–to–proton number ratio to $n/p = e^{-\Delta m/T}$, where $\Delta m = m_n - m_p = 1.293\,\mathrm{MeV}$ is the neutron–proton mass difference.

As the temperature drops and the interaction rates fall below the Hubble expansion rate $\Gamma < H$, these weak interactions freeze–out. This happens at a temperature of

$$T_f = \left(\frac{g_* G_N}{G_F^4}\right)^{1/6} = 0.7\,\mathrm{MeV}, \tag{1.46}$$

where $g_* = g_{\mathrm{boson}} + (7/8) g_{\mathrm{fermion}}$ counts the number of excited relativistic degrees of freedom and G_F is the Fermi constant. At this point, the neutron fraction is $n/p \sim 1/6$. At $T < T_f$, the neutrons undergo β–decay and occasionally, out of equilibrium weak conversions into protons, decreasing the neutron fraction further to $n/p \sim 1/7$ before nuclear reactions actually begin. Almost all of the neutrons that exist at this point will end up in ^{4}He, the most stable light element.

Nucleosynthesis starts with the formation of deuterium, a substantial amount of which is required to synthesise the other, heavier elements. However, the formation of

deuterium, which proceeds through

$$p + n \rightarrow \gamma + \mathrm{D}, \tag{1.47}$$

is subject to what is known as the 'deuterium bottleneck', which delays the formation of stable deuterium to a temperature of $T \sim 0.1\,\mathrm{MeV}$. At temperatures higher than this, the rather fragile deuterium is quickly photodissociated by the high density of CMB photons. It is only after the temperature has dropped to well below the binding energy of deuterium $BE_{\mathrm{D}} = 2.23\,\mathrm{MeV}$, that it is stable enough to partake in further nuclear reactions and heavier elements can be produced.

The synthesis of the heavier elements then proceeds rather quickly. The resulting primordial abundances of the elements depend on the creation/annihilation rates of the respective elements as well as the available abundances of the required nuclei. The evolution of the abundance of element i can be schematically represented by the following Boltzmann equation [79]

$$\frac{\mathrm{d}Y_i}{\mathrm{d}t} = -H(T)\,T\,\frac{\mathrm{d}Y_i}{\mathrm{d}T} = \sum\left(\Gamma_{ij}Y_j + \Gamma_{ikl}Y_kY_l + \cdots\right), \tag{1.48}$$

where $Y_i = n_i/s$ is the yield of the element, defined as the ratio between the number density of the element n_i and the entropy density s, $\Gamma_{ij\ldots}$ is the generalised rates of interconversion and/or decay and $H(T)$ is the temperature–dependent Hubble expansion rate, which at the time relevant to BBN takes the form

$$H(T) = T^2\left(\frac{8\pi^2 g_* G_N}{90}\right)^{1/2}. \tag{1.49}$$

There are many modern numerical codes available to solve the coupled system of equations (1.48) and calculate the resulting primordial abundances, mostly based on the original work by Wagoner, Fowler and Hoyle [80]. These abundances are usually given as a function of the baryon–to–photon ratio η and take as input, the rates $\Gamma_{ij\ldots}$, which are either experimentally determined or theoretically calculated in nuclear physics. For a completely analytical approach to calculating the freeze–out yields, refer to for example, [81].

By far the largest primordial abundance that existed and still exists today is of ^{4}He, formed through the following processes

$$D + D \rightarrow {}^3\mathrm{He} + n, \tag{1.50}$$
$$D + D \rightarrow {}^3\mathrm{H} + p, \tag{1.51}$$
$${}^3\mathrm{He} + D \rightarrow {}^4\mathrm{He} + p, \tag{1.52}$$
$${}^3\mathrm{H} + D \rightarrow {}^4\mathrm{He} + n, \tag{1.53}$$

with its mass fraction estimated to be [82]

$$Y_P = \frac{4n_{^4\mathrm{He}}}{n_{\mathrm{tot}}} = \frac{4\,(n/2)}{n+p} = \frac{2\,(n/p)}{1+n/p} \approx 0.25. \tag{1.54}$$

After BBN stops, there exist only small amounts $\mathcal{O}(10^{-5})$ of D and ^{3}He as most of it was burned into ^{4}He. Heavier elements such as lithium and beryllium were also produced, but only in trace amounts. The synthesis of ^{7}Li and ^{7}Be proceeded through

$$^4\mathrm{He} + {}^3\mathrm{H} \rightarrow {}^7\mathrm{Li} + \gamma, \tag{1.55}$$

$$^4\mathrm{He} + {}^3\mathrm{He} \rightarrow {}^7\mathrm{Be} + \gamma, \tag{1.56}$$

$$^7\mathrm{Be} + \gamma \rightarrow {}^7\mathrm{Li} + p, \tag{1.57}$$

with BBN making a prediction for the combined abundance, of both ^{7}Li and ^{7}Be, of $\mathcal{O}(10^{-10})$. Elements with atomic number $A \geq 9$ were produced in even smaller abundances due to the absence of a stable $A = 8$ nuclei. These abundances and their comparison with observationally inferred primordial abundances are illustrated in Fig. 1.2, taken from [27]. There is a general concordance in the observationally inferred abundances of the light nuclei in that the yellow boxes, along with the vertical blue CMB band, overlap, which is celebrated as a great success of the ΛCDM model. Note that ^{3}He is no longer used as a cosmological probe due to the difficulty in inferring its primordial abundance [83].

As can be observed in Fig. 1.2, the BBN prediction of the primordial abundance of ^{7}Li nuclei overestimates the observationally inferred value. This is commonly referred to as the "Lithium problem". So far explanations involving systematic errors in the measurement of stellar atmospheric temperature, which is needed to infer the abundance of ^{7}Li, is insufficient to make up the discrepancy. Changes in the nuclear rates of processes involved in the creation/annihilation of ^{7}Li also do not produce the required reduction in the BBN prediction of the primordial abundance. This (4-5)σ deviation has been suggested to be a sign of particle physics beyond the standard model [79].

BBN eventually desists as the number density of nucleons decrease and the nuclear reaction rates fall below the expansion rate of the universe due to the increasing suppression of the Coulomb barrier at lower temperatures. No heavier elements are produced during BBN due to the absence of stable nuclei with atomic numbers 5 and 8.

1.2.3 Catalysed BBN

As BBN is very sensitive to the conditions of the early universe in which it takes place, any change in those conditions can greatly affect the primordial abundances of the light elements. This makes it a powerful tool in constraining particle physics beyond the standard model as well as the standard model of cosmology [78]. Many studies

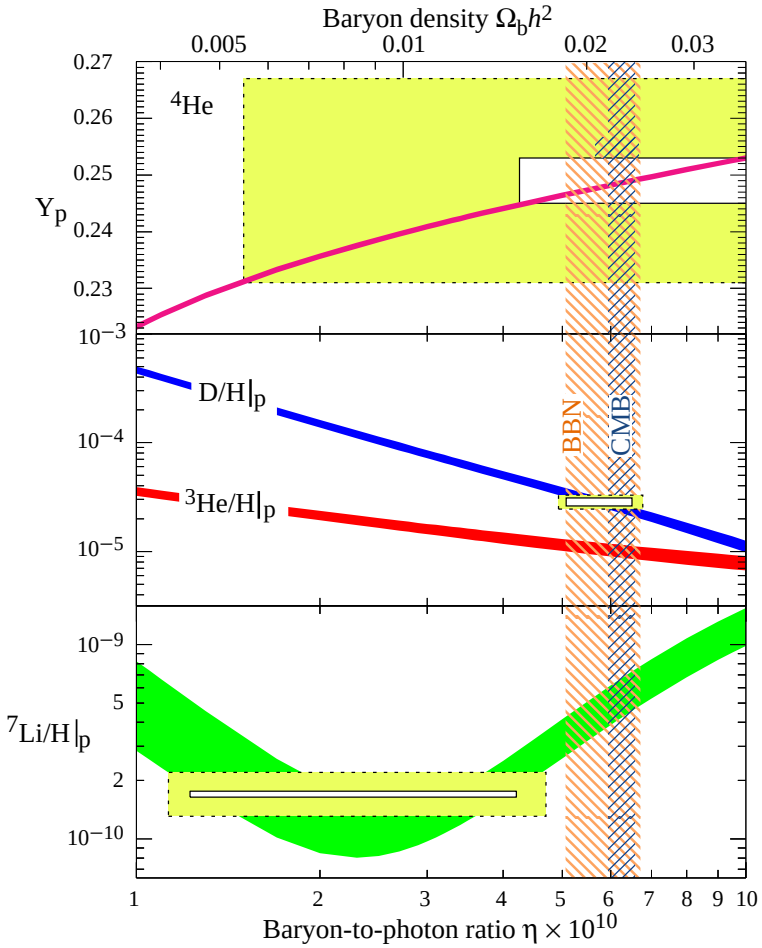

Figure 1.2: The primordial abundances of ^{4}He, D, ^{3}He and ^{7}Li as functions of the baryon–to–photon ratio η, as predicted by standard BBN [82]. The bands for the respective nuclei illustrate the 95% CL range. The white boxes indicate the observationally inferred abundances with $\pm 2\sigma$ statistical errors, while the yellow boxes include the $\pm 2\sigma$ systematic errors as well. The narrow blue vertical shaded band indicates the cosmic baryon density as measured by CMB while the wider peach vertical band indicates the BBN concordance range (both at 95% level). This is taken from [27].

in the context of various BSM models have been carried out. For example, in models that introduce new stable particles, the value of g_* can be altered, depending on the mass and coupling of those particles. Should the new particle be light enough, it could introduce additional relativistic degrees of freedom that could significantly increase the Hubble expansion parameter and thus cause the weak interactions to freeze–out earlier. This would result in a higher neutron fraction n/p and an earlier onset of BBN, hence increasing the abundance of ^{4}He, Y_p.

In this thesis, the effects of long–lived charged massive particles (CHAMPs) in the

early universe, whose consequences on standard BBN (SBBN) were initially explored over 20 years ago [84–86], are of great interest. One of the effects of the existence of CHAMPs during BBN is that they can lead to catalysed BBN (CBBN), through a two–fold impact. As they are charged, the CHAMPs form bound states with existing nuclei, which then partake in nuclear reactions to provide a homologue to each standard BBN (SBBN) reaction

$$\begin{aligned} \text{SBBN}: &\qquad A_1 + A_2 \to A_3 + A_4, \\ \text{CBBN}: &\qquad A_1X + A_2 \to A_3 + A_4 + X, \end{aligned} \tag{1.58}$$

where X is a CHAMP and A_i are nuclei. Another way in which the CHAMPS catalyse SBBN processes is by opening up new reaction channels that were otherwise inaccessible or strongly suppressed in the SM. Note that other types of relics, such as strongly interacting particles, can also result in CBBN. The catalysis of BBN reaction rates could potentially solve the lithium problem through the depletion of ^{7}Be. As ^{7}Li production proceeds through ^{7}Be, a significant reduction in the abundance of ^{7}Be could lead to a ^{7}Li abundance that is in agreement with the observationally inferred value [79].

The focus here is only on the reactions that are pertinent to the study, that is of ^{6}Li and ^{9}Be. The catalysis of the production mechanisms for these two elements takes place at $T \sim 8\,\text{keV}$, when an efficient formation of $^4\text{He}X$ is possible. The following CBBN reactions can then become very efficient in producing ^{9}Be [87–89]‡

$$\begin{aligned} &{}^4\text{He} + ({}^4\text{He}\,X) \to ({}^8\text{Be}\,X) + \gamma, \\ &({}^8\text{Be}\,X) + n \to {}^9\text{Be} + X, \qquad\qquad Q = 0.26\,\text{MeV}, \end{aligned} \tag{1.59}$$

with reaction rates that are many orders of magnitude larger than the SBBN reaction rates. These reactions overcome the problem of the analogous SBBN process

$${}^8\text{Be} + n \to {}^9\text{Be} + \gamma, \qquad Q = 1.665\,\text{MeV}, \tag{1.60}$$

that suffers both from a higher Q–value and an unstable ^{8}Be, which lives for under a femtosecond [88].

The production mechanism of ^{6}Li in SBBN proceeds via the process

$${}^4\text{He} + \text{D} \to {}^6\text{Li} + \gamma, \qquad Q = 1.47\,\text{MeV}, \tag{1.61}$$

which is highly suppressed at BBN temperatures, resulting in a ^{6}Li abundance of $\mathcal{O}(10^{-14})$. With the presence of metastable charged particles X however, a new production mechanism becomes available [87]

$$({}^4\text{He}\,X) + \text{D} \to {}^6\text{Li} + X, \qquad Q \approx 1.13\,\text{MeV}. \tag{1.62}$$

‡The large ^{9}Be–production cross section reported and used in [88, 89] has recently been questioned by [90], in which a study based on a four–body model is announced as work in progress to clarify the efficiency of ^{9}Be production.

This photonless production mechanism rate is $\mathcal{O}(10^6)$ larger than the SBBN equivalent given by (1.61) [87].

This is interesting as observational data has shown that the inferred primordial abundances of ^{6}Li and ^{9}Be are above those predicted by SBBN [89, 91–93]. The constraints from avoiding the overproduction of both ^{6}Li and ^{9}Be can be translated into a constraint on the lifetime of these CHAMPs [87, 94–96]

$$\tau_X \lesssim 5 \times 10^3 \,\mathrm{s}, \tag{1.63}$$

when typical yields are assumed for the thermal relics of X. More details are given in Chapter 3.

In contrast to SBBN, the calculations involving CBBN processes take only theoretical reaction rates as input, as they cannot be experimentally confirmed. However, as these processes involve mostly electromagnetic interactions, the uncertainty in the rates are small. Note that by assuming a significant amount of late–time entropy production after CHAMP decoupling and before primordial nucleosynthesis – which is a non-standard cosmological history – this limit can be weakened. This is discussed for the case of the gravitino LSP in [97].

1.2.4 Late Energy Injection

Another way in which long–lived CHAMPs can alter the predictions of SBBN is by the late injection of electromagnetic and hadronic energy through their decay products. This has an effect when the CHAMPs decay during or after BBN. The magnitude and extent of the effects on SBBN depend on the lifetime of the CHAMPs.

From hadronic decays, quarks and gluons are produced, which fragment into hadronic jets. For $\tau_X \lesssim 100$ s, these mesons and nucleons lose their energy very efficiently and are quickly stopped via electromagnetic interaction. Thus, hadro/photodissociation is not important at these times and no light elements are directly destroyed. Instead, the now slow–moving emitted hadrons can take part in proton–neutron interconversion processes [98, 99], which could lead to a sizeable increase in the abundance of ^{4}He and D. Indeed, the most stringent constraint in this region would come from ^{4}He [99]. This is due to the fact that the protons are more abundant during these times, which feeds the conversion of p to n more than the reverse and hence increases the n/p ratio. However, without a dedicated numerical treatment of primordial nucleosynthesis that includes non–standard processes at hand, it is difficult to derive quantitative limits in this parameter region.

At $\tau_X \gtrsim 100$ s, the mesons decay before they can interact with the background nucleons while the emitted nucleons remain energetic and can lead to significant hadrodissociation in the light elements [100–105]. Through successive hadronic collisions with the background nucleons, hadronic showers are produced. During this process, a significant amount of ^{4}He can be dissociated into D, ^{3}H and ^{3}He. The ^{3}H and ^{3}He nuclei

then go on to produce ^{6}Li and ^{7}Li via processes that include the background ^{4}He. The high abundance of ^{4}He during these times allows these processes to potentially create significantly higher abundances of these light elements than predicted by SBBN [99]. Constraints on the hadronic energy injection can thus be imposed by the primordial abundances of ^{4}He, ^{3}He/D, ^{7}Li, ^{6}Li/^{7}Li and D [99, 104–109]. However, in the region allowed by CBBN constraints $\tau_X \lesssim \mathcal{O}(10^3\,\mathrm{s})$, see (1.63), the hadronic effect on D, whose abundance is affected through the hadrodissociation of ^{4}He, dominates. This can be seen for example, in Figs. 38–41 of [99] and in Figs. 6–8 of [105].

For $\tau_X \gtrsim 10^4$ s, the contribution from electromagnetic energy injection [91,98,99,105, 110] starts becoming significant and can also affect the abundance of primordial light elements. Analogous to the hadronic decays, the electromagnetic decay products induce electromagnetic showers, which go on to destroy/create the light elements, including ^{7}Li. Due to their large abundances, photodissociation of D and ^{4}He is the most effective at these times. At $\tau_X \lesssim 10^6$ s the dominant constraint would come from the destruction of D and for $\tau_X \gtrsim 10^6$ s from the overproduction of D and ^{3}He due to the destruction of ^{4}He.

Chapter 2

Stau NLSP Decays

In this chapter, the calculations and results of the 2–, 3– and 4–body decays of the stau NLSP into the axino are outlined. In the particle physics setting considered in this thesis, this is the 2–body decay of the right–handed stau into the tau and the axino $\widetilde{\tau}_{\mathrm{R}} \to \tau\widetilde{a}$, the 3–body decay into the tau, the axino and a photon $\widetilde{\tau}_{\mathrm{R}} \to \tau\widetilde{a}\gamma$, and the 4–body decay into the tau, the axino and a $q\bar{q}$ pair $\widetilde{\tau}_{\mathrm{R}} \to \tau\widetilde{a}q\bar{q}$. Finally, the resulting lifetime of the stau NLSP, which is governed by the 2–body decay, is discussed.

2.1 2–body Decays

In this section the 2–body decay $\widetilde{\tau}_{\mathrm{R}} \to \tau\widetilde{a}$ of the stau NLSP into the tau and the axino LSP, which first occurs at the two–loop level, is considered. The relevant Feynman diagrams are shown in Fig. 2.1, with 32 diagrams in total. As $m_\tau \ll m_{\widetilde{\tau}}$, the limit $m_\tau \to 0$ is taken.

For the calculation of the two–loop diagrams, the large mass hierarchy between the heavy quark multiplet and the electroweak scale or the supersymmetry breaking scale can be exploited, see (1.31). As a result, a heavy mass expansion (HME) in powers of $1/f_a$ can be performed. Already the leading term $\propto 1/f_a$ of the amplitude provides a precise approximation since the sub–leading terms are suppressed by many orders of magnitude. After the HME, only vacuum two–loop integrals (i.e. integrals with zero external momenta) and one–loop integrals remain in the expansion coefficients, for which well–known results are available in literature.

In this section, only a basic outline of the heavy mass expansion as it becomes relevant to understanding the calculation is given. Further details about the technique than what is explained here can be found in Appendix A. For a Feynman integral $\mathcal{F}$ of Feynman diagram Γ, the expansion can be compactly written as

$$\mathcal{F}(\Gamma) \to \mathcal{F}'(\Gamma) = \sum_{\gamma} \mathcal{F}(\Gamma\backslash\gamma) * \mathcal{T}_{\{k_i,m_i\}}\mathcal{F}(\gamma), \tag{2.1}$$

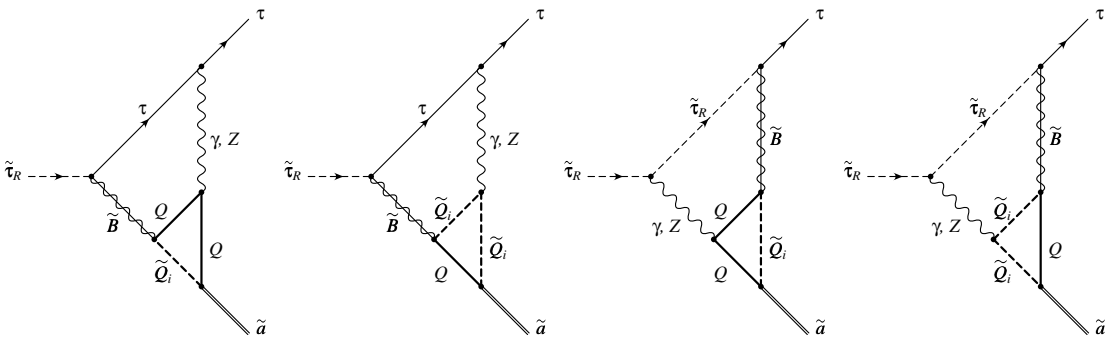

Figure 2.1: Feynman diagrams for the 2–body stau NLSP decay $\widetilde{\tau}_{\rm R} \to \tau\widetilde{a}$ in the considered type of KSVZ axion models. The thick lines indicate heavy (s)quark propagators Q and $\tilde{Q}_{1,2}$.

where γ represents the subgraphs over which the sum is performed (a subgraph is derived by drawing all possible one–particle irreducible graphs containing the heavy propagators). The operator $\mathcal{T}_{\{k_i,m_i\}}$ performs a Taylor expansion on the subgraphs with respect to the small parameters k_i and/or m_i where i runs over all momenta and masses that are considered small compared to the large mass $m_Q = yf_a/\sqrt{2}$. $\mathcal{F}(\Gamma\backslash\gamma)$ represents the original graphs where the subgraphs have been shrunk to a point. Using the Feynman rules derived in [111], where the methodology was first laid out, the diagrams are calculated using FeynCalc 5.1 [112] and LoopTools 2.4 [113].

The calculation of one representative diagram is followed to outline the main steps. In particular, the calculation of the diagram on the far right in Fig. 2.1 with $i = 1$ is chosen for this purpose. This diagram shall be denoted by $\Gamma^{\zeta}_{\rm 2b}$ and the momenta running through it are shown explicitly in Fig. 2.2. Note that the ultraviolet (UV) divergences

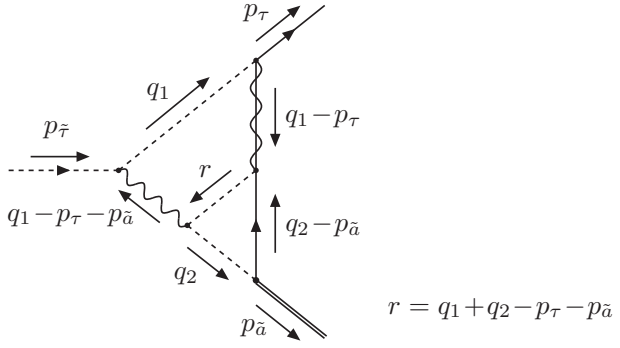

Figure 2.2: Feynman diagram $\Gamma^{\zeta}_{\rm 2b}$ for the 2–body stau NLSP decay $\widetilde{\tau}_{\rm R} \to \tau\widetilde{a}$.

encountered in the calculation do not cancel on a diagram by diagram basis. Translating the diagram into the corresponding amplitude using the relevant Feynman rules and

carrying out some simplification of the Dirac algebra gives

$$\mathcal{M}^{\zeta}_{2\mathrm{b}} = N_c \frac{\alpha^2 e_Q^2 y}{128\pi^8 c_W^2}\, m_{\widetilde{B}} m_Q \int \frac{\mathrm{d}^D q_1}{(2\pi\mu)^{4-D}} \int \frac{\mathrm{d}^D q_2}{(2\pi\mu)^{4-D}} \frac{1}{(q_1 - p_\tau - p_{\widetilde{a}})^2 (q_1^2 - m_{\widetilde{\tau}}^2)\left((q_1 - p_\tau)^2 - m_{\widetilde{B}}^2\right)} \times \frac{\bar{u}(p_\tau)\Big[P_L(p_\tau + p_{\widetilde{a}} + q_1)\cdot(p_\tau + p_{\widetilde{a}} - q_1 - 2q_2)\Big] v(p_{\widetilde{a}})}{\left((q_2 - p_{\widetilde{a}})^2 - m_Q^2\right)\left((-p_\tau - p_{\widetilde{a}} + q_1 + q_2)^2 - m_Q^2\right)\left(q_2^2 - m_Q^2\right)}, \tag{2.2}$$

where N_C is the number of colours, $P_L = 1/2(1-\gamma_5)$, α is the fine structure constant and $c_{\mathrm{W}} \equiv \cos\theta_{\mathrm{W}}$, where θ_{W} is the Weinberg angle. D denotes the number of dimensions and μ is the regularisation scale. The momentum running through the outer loop is denoted by q_1 while q_2 is the momentum running through the heavy loop. All external momenta and masses other than that of the heavy (s)quarks are taken to be small. As the loop momenta are not bounded by energy or momentum conservation, there are phase space regions where they are of the order of the large mass m_Q and regions where they are small. Each of these regions must be considered separately in order to carry out a consistent expansion of the diagram.

There are four such regions and it can be shown that in two of these regions the integrals reduce to scaleless integrals after expansion and therefore vanish in dimensional regularisation. There are thus only two regions that must be calculated. The corresponding subgraphs are labelled γ_1 and γ_2, leading to

$$\mathcal{F}'(\Gamma^{\zeta}_{2\mathrm{b}}) = \mathcal{F}(\Gamma^{\zeta}_{2\mathrm{b}} \backslash \gamma_1) * \mathcal{T}_{\{k_i,m_i\}} \mathcal{F}(\gamma_1) + \mathcal{F}(\Gamma^{\zeta}_{2\mathrm{b}} \backslash \gamma_2) * \mathcal{T}_{\{k_i,m_i\}} \mathcal{F}(\gamma_2). \tag{2.3}$$

Starting with the first region, both the loop momenta are large $|q_1|, |q_2| \sim m_Q$, with all the other parameters small. Accordingly, the full diagram must be Taylor expanded in the external momenta and the stau and bino masses

$$\begin{aligned}
\mathcal{T}_{\{k_i,m_i\}} \mathcal{F}(\gamma_1) &= \mathcal{T}_{\{p_\tau, p_{\widetilde{a}}, m_{\widetilde{\tau}}, m_{\widetilde{B}}\}} \mathcal{M}^{\zeta}_{2\mathrm{b}} \\
&= -\frac{\alpha^2 e_Q^2 y}{8D\pi^6 c_W^2}\, m_{\widetilde{B}} m_Q \Bigg\{ m_{\widetilde{a}}^2 \Big[2m_Q^2 T_0(2,3,2) + 4m_Q^2 T_0(2,4,1) - T_0(1,3,2) \\
&\quad - (D-5) T_0(2,3,1) + T_0(3,1,2) - 3T_0(3,2,1) \Big] + D \Big[m_{\widetilde{B}}^2 T_0(3,2,1) \\
&\quad + T_0(2,2,1) \Big] - m_{\widetilde{\tau}}^2 \Big[-4m_Q^2 T_0(2,2,3) - 2m_Q^2 T_0(2,3,2) + T_0(1,3,2) \\
&\quad + (D-8) T_0(2,2,2) + T_0(2,3,1) + 3T_0(3,1,2) - 7T_0(3,2,1) \\
&\quad - 2T_0(3,3,0) \Big] \Bigg\},
\end{aligned} \tag{2.4}$$

where

$$T_0(n_1,n_2,n_3) = \int \mathrm{d}^D q_1\, \mathrm{d}^D q_2\, \frac{1}{(q_1^2-m_Q^2)^{n_1}(q_2^2-m_Q^2)^{n_2}(q_1+q_2)^{2n_3}}. \tag{2.5}$$

These two–loop T_0 integrals can be reduced to one master integral $T_0(1,1,0)$, i.e. the product of two one–loop integrals. Putting in $D = 4-2\epsilon$ and taking the leading term leads to the following expression

$$\mathcal{T}_{\{p_\tau,p_{\widetilde{a}},m_{\widetilde{\tau}},m_{\widetilde{B}}\}}\mathcal{F}(\gamma_1) = \frac{\epsilon-1}{2\epsilon+1}\frac{\alpha^2 e_Q^2}{256\pi^8 c_W^2}\frac{y\, m_{\widetilde{B}}}{m_Q^5}T_0(1,1,0). \tag{2.6}$$

Substituting in for T_0 and evaluating the integrals give the following result

$$\mathcal{F}(\Gamma_{2\mathrm{b}}^{\zeta}\backslash\gamma_1) * \mathcal{T}_{\{p_\tau,p_{\widetilde{a}},m_{\widetilde{\tau}},m_{\widetilde{B}}\}}\mathcal{F}(\gamma_1) = \frac{\alpha^2 e_Q^2}{256\pi^4 c_W^2}\frac{y\, m_{\widetilde{B}}}{m_Q}\left[2\log\left(\frac{\mu^2}{m_Q^2}\right)-1+\frac{1}{\epsilon}\right]\bar{u}(p_\tau)P_L v(p_{\widetilde{a}}). \tag{2.7}$$

For the second term in the heavy mass expansion, the heavy loop must be Taylor expanded in q_2 as well as the external momenta and stau and bino masses, as the second region consists of $|q_1| \ll m_Q$ and $|q_2| \sim m_Q$

$$\mathcal{T}_{\{k_i,m_i\}}\mathcal{F}(\gamma_2) = \mathcal{T}_{\{p_\tau,p_{\widetilde{a}},q_1,m_{\widetilde{\tau}},m_{\widetilde{B}}\}}\frac{(p_\tau+p_{\widetilde{a}}+q_1)\cdot(p_\tau+p_{\widetilde{a}}-q_1-2q_2)}{\left((q_2-p_{\widetilde{a}})^2-m_Q^2\right)\left((-p_\tau-p_{\widetilde{a}}+q_1+q_2)^2-m_Q^2\right)\left(q_2^2-m_Q^2\right)}. \tag{2.8}$$

Only the leading non-vanishing terms in the small parameters are kept*, leading to

$$\mathcal{T}_{\{p_\tau,p_{\widetilde{a}},q_1,m_{\widetilde{\tau}},m_{\widetilde{B}}\}}\mathcal{F}(\gamma_2) = \frac{(p_\tau+p_{\widetilde{a}}+q_1)\cdot(p_\tau+p_{\widetilde{a}}-q_1-2q_2)}{\left(q_2^2-m_Q^2\right)^3}, \tag{2.9}$$

which is then inserted into the original diagram where the heavy loop has been shrunk to a point, to give the second of the two terms in the heavy mass expansion

$$\begin{aligned}\mathcal{F}(\Gamma_{2\mathrm{b}}^{\zeta}\backslash\gamma_2) * \mathcal{T}_{\{p_\tau,p_{\widetilde{a}},q_1,m_{\widetilde{\tau}},m_{\widetilde{B}}\}}\mathcal{F}(\gamma_2) = N_c\frac{\alpha^2 e_Q^2 y}{128\pi^8 c_W^2}\, m_{\widetilde{B}} m_Q \int\frac{\mathrm{d}^D q_2}{(2\pi\mu)^{4-D}}\frac{1}{\left(q_2^2-m_Q^2\right)^3} \\ \times\int\frac{\mathrm{d}^D q_1}{(2\pi\mu)^{4-D}}\frac{\bar{u}(p_\tau)P_L\Big[(p_\tau+p_{\widetilde{a}}+q_1)\cdot(p_\tau+p_{\widetilde{a}}-q_1-2q_2)\Big]v(p_{\widetilde{a}})}{(q_1-p_\tau-p_{\widetilde{a}})^2\,(q_1^2-m_{\widetilde{\tau}}^2)\left((q_1-p_\tau)^2-m_{\widetilde{B}}^2\right)}.\end{aligned} \tag{2.10}$$

*The formally leading term can often give a vanishing result.

The tensor integrals are reduced using Passarino–Veltman reduction procedures which are briefly outlined in Appendix A.2, before the integrals are evaluated. The end result can then be expressed in terms of A_0, B_0 and C_0, the usual scalar one–loop tadpole, self–energy and vertex functions, respectively [114]. The expression is rather lengthy and only the UV–divergent parts are presented here to give an idea of the structure of the result of the expansion

$$\mathcal{F}(\Gamma_{\rm 2b}^{\zeta}\backslash\gamma_2) * \mathcal{T}_{\{p_\tau,p_{\tilde{a}},q_1,m_{\tilde{\tau}},m_{\tilde{B}}\}}\mathcal{F}(\gamma_2)|_{\rm UV-div} = \frac{1}{\epsilon}\frac{\alpha^2 e_Q^2}{16\pi^2}\frac{y\, m_{\tilde{B}}}{m_Q}\,\bar{u}(p_\tau)P_L v(p_{\tilde{a}}). \tag{2.11}$$

Once all 32 diagrams are summed up, the $1/\epsilon$ divergences cancel and the dependence on μ drops out, resulting in the leading term in the heavy mass expansion of the diagram. The decay width is given by

$$\Gamma(\widetilde{\tau}_{\rm R} \to \tau\widetilde{a}) = \frac{1}{2m_{\tilde{\tau}}}\Phi_2 \sum_{\rm spins} \overline{|\mathcal{M}(\widetilde{\tau}_{\rm R} \to \tau\widetilde{a})|}^2, \tag{2.12}$$

where the bar over the amplitude indicates an averaging over the stau initial states and Φ_2 is the 2–body phase space

$$\Phi_2 = \frac{1}{2m_{\tilde{\tau}}}\frac{1}{4\pi}\frac{m_{\tilde{\tau}}^2 - m_{\tilde{a}}^2}{2m_{\tilde{\tau}}}. \tag{2.13}$$

The following result for the decay rate is thus obtained

$$\Gamma(\widetilde{\tau}_{\rm R} \to \tau\widetilde{a}) = \frac{m_{\tilde{\tau}}(1-A_{\tilde{a}})^2}{16\pi}\,|A|^2, \tag{2.14}$$

$$
\begin{aligned}
A = \frac{3\alpha^2\, e_Q^2}{8\pi^2\, c_{\rm W}^4}\,\frac{\sqrt{2}\, m_{\tilde\tau}}{f_a}\Bigg[& 3\sqrt{A_{\tilde B}}\,\log\left(\frac{y^2 f_a^2}{2\, m_{\tilde\tau}^2}\right) - \frac{1}{4}\sqrt{A_{\tilde a}} \\
& + \frac{2(1-A_{\tilde B})[\sqrt{A_{\tilde a}}(1-A_{\tilde B}) - \sqrt{A_{\tilde B}}(1-A_{\tilde a})]}{1-A_{\tilde a}}\log\frac{A_{\tilde B}-1}{A_{\tilde B}} \\
& + \frac{2c_{\rm W}^2\sqrt{A_{\tilde B}}(A_{\tilde a}-A_{\tilde B})(1-\sqrt{A_{\tilde B}/A_{\tilde a}})}{1-A_{\tilde a}}\log\frac{A_{\tilde B}-A_{\tilde a}}{A_{\tilde B}} \\
& + \frac{2\sqrt{A_{\tilde a}}(1-A_{\tilde B})^2 - \sqrt{A_{\tilde B}}(2-A_{\tilde B})(1-A_{\tilde a}) + 2c_{\rm W}^2(1-A_{\tilde B})(A_{\tilde a}\sqrt{A_{\tilde B}} + A_{\tilde B}\sqrt{A_{\tilde a}})}{(1-A_{\tilde a})(1-A_{\tilde B})}\log A_{\tilde B} \\
& - \frac{s_{\rm W}^2(\sqrt{A_{\tilde a}}-\sqrt{A_{\tilde B}})[2(\sqrt{A_{\tilde a}}+\sqrt{A_{\tilde B}})^2 - A_Z(1+\sqrt{A_{\tilde a}A_{\tilde B}})]}{1-A_{\tilde a}}\, m_{\tilde\tau}^2\, C_0(m_{\tilde\tau}^2, m_{\tilde a}^2, 0, m_{\tilde\tau}^2, m_Z^2, m_{\tilde B}^2) \\
& - \frac{2c_{\rm W}^2(\sqrt{A_{\tilde a}}+\sqrt{A_{\tilde B}})(A_{\tilde a}-A_{\tilde B})}{1-A_{\tilde a}}\, m_{\tilde\tau}^2\, C_0(m_{\tilde\tau}^2, m_{\tilde a}^2, 0, m_{\tilde\tau}^2, 0, m_{\tilde B}^2) \\
& - \frac{2s_{\rm W}^2[\sqrt{A_{\tilde a}}(1-A_{\tilde B}) - \sqrt{A_{\tilde B}}(1-A_{\tilde a})]}{1-A_{\tilde a}}\, m_Z^2\, C_0(0, m_{\tilde a}^2, m_{\tilde\tau}^2, 0, m_Z^2, m_{\tilde B}^2) \\
& - \frac{s_{\rm W}^2\sqrt{A_{\tilde a}}(2\sqrt{A_{\tilde a}A_{\tilde B}} + 2A_{\tilde B} - A_Z)}{1-A_{\tilde a}}\left(B_0(m_{\tilde a}^2, m_Z^2, m_{\tilde B}^2) - B_0(0,0,m_{\tilde\tau}^2)\right) \\
& + \frac{s_{\rm W}^2(2\sqrt{A_{\tilde B}} + 2\sqrt{A_{\tilde a}} - \sqrt{A_{\tilde a}}A_Z)}{1-A_{\tilde a}}\Big(B_0(m_{\tilde\tau}^2, m_Z^2, m_{\tilde\tau}^2) - B_0(0,0,m_{\tilde\tau}^2)\Big) \\
& - \frac{2[s_{\rm W}^2\sqrt{A_{\tilde a}}(1-A_{\tilde B}) - (4+c_{\rm W}^2)\sqrt{A_{\tilde B}}(1-A_{\tilde a})]}{1-A_{\tilde a}}\Bigg],
\end{aligned}
\tag{2.15}
$$

with

$$
A_{\tilde a} \equiv \frac{m_{\tilde a}^2}{m_{\tilde\tau}^2}, \qquad A_{\tilde B} \equiv \frac{m_{\tilde B}^2}{m_{\tilde\tau}^2}, \qquad A_Z \equiv \frac{m_Z^2}{m_{\tilde\tau}^2}, \tag{2.16}
$$

where the substitution $m_Q = y f_a/\sqrt{2}$ has been made. The result has been arranged so as to make the independence of the regularisation scale (which appears implicitly in the B_0 functions) manifest.

A striking feature of (2.14) is the appearance of the logarithm term $\propto \log(y^2 f_a^2/2m_{\tilde\tau}^2)$ in the first line of (2.15). For typical values, $y \approx 1$, $f_a \sim 10^9 \ldots 10^{16}$ GeV, and $m_{\tilde\tau} \sim 100 \ldots 1000$ GeV, the logarithm becomes large, $\log(y^2 f_a^2/2m_{\tilde\tau}^2) \sim 26 \ldots 63$, and dominates the numerical result. This aspect will further be elaborated on below, and in particular, in Sec. 2.4.

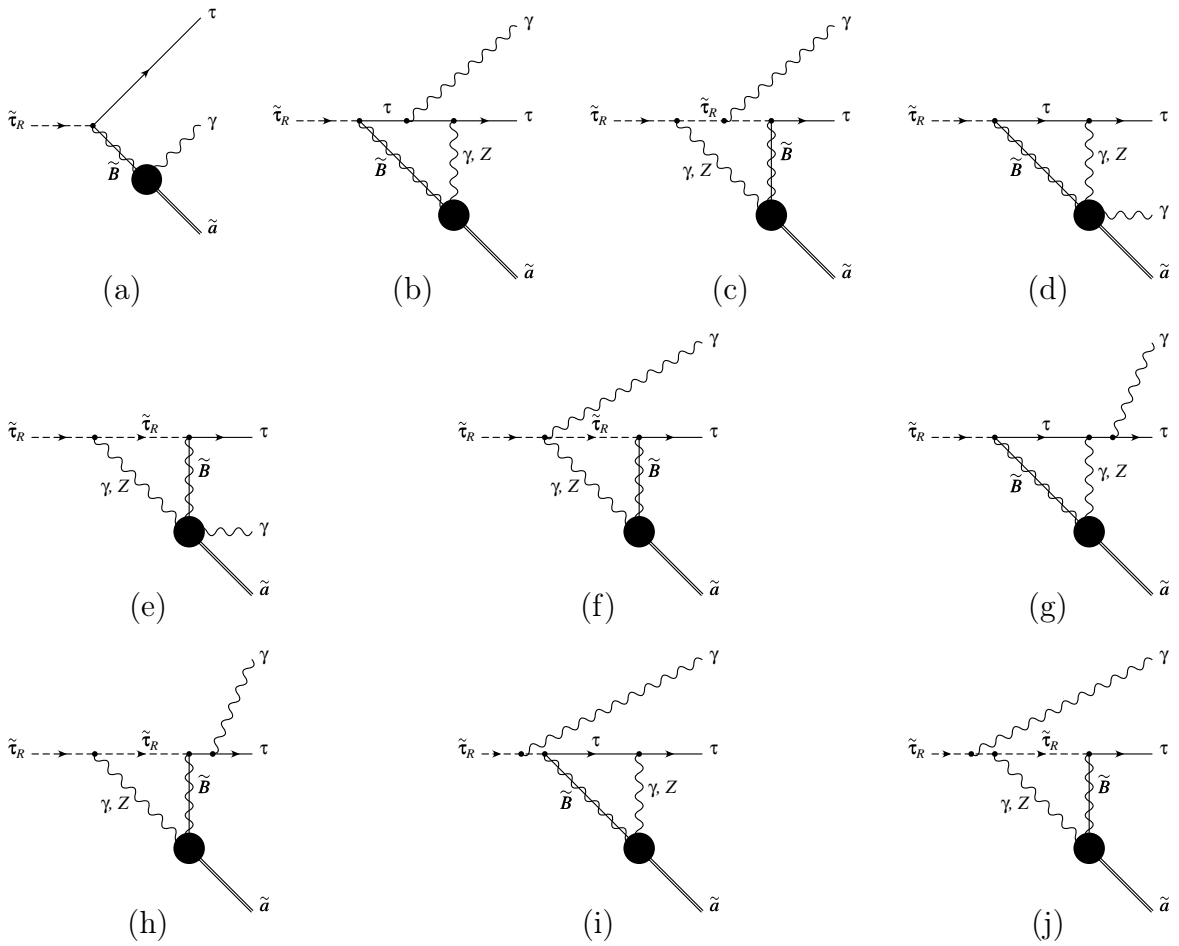

Figure 2.3: Feynman diagrams for the 3–body stau NLSP decay $\widetilde{\tau}_{\rm R} \to \tau\widetilde{a}\gamma$ in KSVZ axion models, at one–loop (a) and two–loop (b-j) level. The blob indicates the heavy (s)quark loops.

2.2 3–body Decays

Now let us turn to the 3–body decay $\widetilde{\tau}_{\rm R} \to \tau\widetilde{a}\gamma$. As before, the tau mass will be neglected throughout. The 3–body decay occurs already at one–loop order, see Fig. 2.3 (a), where the heavy quarks and squarks run in the loop indicated by the blob. However, the two–loop contributions shown in Fig. 2.3 (b-j) can be numerically important since they could generate a large logarithmic factor $\log(y^2 f_a^2/2m_{\widetilde{\tau}}^2)$, similar to the one in (2.14). This factor can partially compensate the loop suppression factor α.

Again the associated squared matrix element of the diagrams is calculated using an asymptotic expansion for large (s)quark masses (1.31), retaining only the leading term $\propto 1/f_a$. The same notation is kept, with q_1 denoting the momentum running through the outer loop while q_2 denotes the momentum running through the heavy loop. For the one–loop diagram, q_2 is also used to denote the momentum of the heavy loop for

consistency.

An outline of the one–loop calculation is given here. There are eight diagrams contributing to the one–loop amplitude, four with two squarks and one quark in the heavy loop, and four with one squark and two quarks. There are two momentum regions to be considered, $|q_2| \sim m_Q$ and $|q_2| \ll m_Q$. The second region vanishes after the Taylor expansion due to a reduction to scaleless integrals. Therefore the integral only needs to be evaluated in the first region, which involves a Taylor expansion in $1/q_2$ and large mass $1/m_Q$. The calculation for the two–loop diagrams proceeds exactly as for the 2–body diagrams above. The calculation of one characteristic diagram, denoted by $\Gamma^{\psi}_{3\mathrm{b}}$, shall be followed. This is illustrated in Fig. 2.4. The matrix element of $\Gamma^{\psi}_{3\mathrm{b}}$ is given by

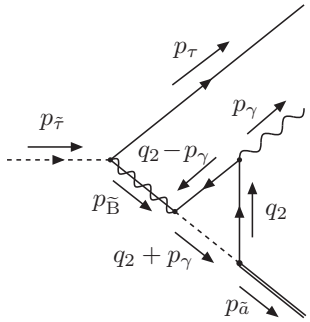

Figure 2.4: Feynman diagram $\Gamma^{\psi}_{3\mathrm{b}}$ for the 3–body, one–loop stau NLSP decay $\widetilde{\tau}_{\mathrm{R}} \to \tau \tilde{a} \gamma$.

$$\begin{aligned}\mathcal{M}^{\psi}_{3\mathrm{b}} = &-\frac{i\alpha^{3/2} e_Q^2 y}{c_W^2 \pi^{5/2}} \frac{1}{(p_{\tilde{a}} + p_\gamma)^2 - m_{\widetilde{B}}^2} \\ &\times \int \frac{\mathrm{d}^D q_2}{(2\pi\mu)^{4-D}} \frac{\bar{u}(p_\tau) P_L \big(m_{\widetilde{B}} - \not{p}_{\tilde{a}} - \not{p}_\gamma\big) P_R \,(m_Q - \not{p}_\gamma + \not{q}_2) \not{\varepsilon}^*(p_\gamma)(m_Q + \not{q}_2)\, P_R\, v(p_{\tilde{a}})}{\big((q_2 - p_\gamma)^2 - m_Q^2\big)\,\big(q_2^2 - m_Q^2\big)\,\big((p_{\tilde{a}} + q_2)^2 - m_Q^2\big)}.\end{aligned} \tag{2.17}$$

Similarly to the two–loop case, the Taylor expansion on the subgraph is evaluated first

$$\begin{aligned}\mathcal{T}_{\{k_i, m_i\}} \mathcal{F}(\gamma_1) &= \mathcal{T}_{\{p_\tau, p_{\tilde{a}}, p_\gamma, m_{\widetilde{B}}\}} \frac{P_L \left(m_{\widetilde{B}} - \not{p}_{\tilde{a}} - \not{p}_\gamma\right) P_R \,(m_Q - \not{p}_\gamma + \not{q}_2)\ \not{\varepsilon}^*(p_\gamma)\,(m_Q + \not{q}_2)\, P_R}{\big((q_2 - p_\gamma)^2 - m_Q^2\big)\,\big(q_2^2 - m_Q^2\big)\,\big((q_2 + p_{\tilde{a}})^2 - m_Q^2\big)} \\ &= \frac{P_L \left(m_{\widetilde{B}} - \not{p}_{\tilde{a}} - \not{p}_\gamma\right) P_R \,(m_Q - \not{p}_\gamma + \not{q}_2)\ \not{\varepsilon}^*(p_\gamma)\,(m_Q + \not{q}_2)\, P_R}{\big(q_2^2 - m_Q^2\big)^3},\end{aligned} \tag{2.18}$$

where again, only the leading non-vanishing terms in the expansion has been kept.

Inserting this back in the full graph,

$$\mathcal{F}(\Gamma^{\psi}_{3\mathrm{b}}\backslash\gamma_1) * \mathcal{T}_{\{p_\tau,p_{\widetilde{a}},p_\gamma,m_{\widetilde{B}}\}}\mathcal{F}(\gamma_1) = -\frac{i\alpha^{3/2}e_Q^2 y}{c_W^2\pi^{5/2}}\frac{1}{\left(p_{\widetilde{a}}+p_\gamma\right)^2-m_{\widetilde{B}}^2} \times \int\frac{\mathrm{d}^D q_2}{(2\pi\mu)^{4-D}}\frac{\bar{u}(p_\tau)P_L\big(m_{\widetilde{B}}-\not{p}_{\widetilde{a}}-\not{p}_\gamma\big)P_R\,(m_Q-\not{p}_\gamma+\not{q}_2)\not{\epsilon}^*(p_\gamma)(m_Q+\not{q}_2)P_R\,v(p_{\widetilde{a}})}{\left(q_2^2-m_Q^2\right)^3}, \tag{2.19}$$

and evaluating the momentum integral leads to

$$\mathcal{M}^{\psi}_{3\mathrm{b}} = -i\frac{\alpha^{3/2}e_Q^2}{2c_W^2\pi^{1/2}}\frac{y}{m_Q}\frac{\bar{u}(p_\tau)P_L\left(m_{\widetilde{B}}-\not{p}_{\widetilde{a}}-\not{p}_\gamma\right)P_R\,(m_Q-\not{p}_\gamma)\not{\epsilon}^*(p_\gamma)\,P_R v(p_{\widetilde{a}})}{\left(p_{\widetilde{a}}+p_\gamma\right)^2-m_{\widetilde{B}}^2}, \tag{2.20}$$

where only the leading term in ϵ has been taken.

The complete result for the two–loop contribution is rather lengthy. However, since the 3–body decay rate is suppressed with respect to that of the 2–body decay, it is sufficiently accurate to keep only the dominant logarithm term $\propto \log(y^2 f_a^2/2m_{\widetilde{\tau}}^2)$ of the two–loop part. The differential decay rate including the one– and two–loop amplitudes reads

$$\frac{\mathrm{d}^2\Gamma(\widetilde{\tau}_\mathrm{R}\to\tau\widetilde{a}\gamma)}{\mathrm{d}x_\gamma\,\mathrm{d}\cos\theta} = \frac{1}{2m_{\widetilde{\tau}}}\frac{\mathrm{d}^2\Phi_3}{\mathrm{d}x_\gamma\,\mathrm{d}\cos\theta}\sum_{\text{spins}}\overline{|\mathcal{M}(\widetilde{\tau}_\mathrm{R}\to\tau\widetilde{a}\gamma)|}^2, \tag{2.21}$$

where Φ_3 is the 3–body phase space

$$\frac{\mathrm{d}^2\Phi_3}{\mathrm{d}x_\gamma\,\mathrm{d}\cos\theta} = \frac{m_{\widetilde{\tau}}^2}{256\pi^3}\frac{x_\gamma(1-A_{\widetilde{a}}-x_\gamma)}{\left[1-(x_\gamma/2)(1-\cos\theta)\right]^2}, \tag{2.22}$$

and

$$x_\gamma = 2E_\gamma/m_{\widetilde{\tau}}\ , \tag{2.23}$$

is the photon energy E_γ divided by its maximum value and θ is the angle between the photon and tau in the rest frame of the stau. In full, the 3-body differential decay rate is given by

$$\frac{\mathrm{d}^2\Gamma(\widetilde{\tau}_\mathrm{R} \to \tau\widetilde{a}\gamma)}{\mathrm{d}x_\gamma\,\mathrm{d}\cos\theta} = \frac{9}{64\pi^4}\,\frac{\alpha^3\,e_Q^4}{c_\mathrm{W}^4}\,\frac{m_{\widetilde{\tau}}^3}{f_a^2}\,\frac{x_\gamma(1-A_{\tilde{a}}-x_\gamma)}{[2-x_\gamma(1-\cos\theta)]^2}$$
$$\times\Bigg[\frac{2x_\gamma^2(1-A_{\tilde{a}}-x_\gamma)[1+\cos\theta+A_{\tilde{a}}(1-\cos\theta)][1+\cos\theta+A_{\tilde{B}}(1-\cos\theta)]}{[2A_{\tilde{a}}-A_{\tilde{B}}(2-x_\gamma+x_\gamma\cos\theta)+x_\gamma(1+\cos\theta)]^2}$$
$$+\frac{3\alpha}{\pi c_\mathrm{W}^2}\,\log\left(\frac{y^2f_a^2}{2m_{\widetilde{\tau}}^2}\right)\frac{[A_{\tilde{B}}(1-A_{\tilde{a}})+\sqrt{A_{\tilde{a}}A_{\tilde{B}}}(1-A_{\tilde{a}}-x_\gamma)](1+\cos\theta)+A_{\tilde{a}}A_{\tilde{B}}x_\gamma(1-\cos\theta)}{2A_{\tilde{a}}-A_{\tilde{B}}(2-x_\gamma+x_\gamma\cos\theta)+x_\gamma(1+\cos\theta)}$$
$$+\frac{9\alpha^2}{8\pi^2c_\mathrm{W}^4}\,\log^2\left(\frac{y^2f_a^2}{2m_{\widetilde{\tau}}^2}\right)A_{\tilde{B}}\frac{2(1-A_{\tilde{a}})(1-A_{\tilde{a}}-x_\gamma)(1+\cos\theta)+x_\gamma^2[2-(1-A_{\tilde{a}})(1-\cos\theta)]}{x_\gamma^2(1-\cos\theta)(1-A_{\tilde{a}}-x_\gamma)}\Bigg]. \tag{2.24}$$

It is interesting to note that only the contributions from the diagrams in Fig. 2.3 (f-j) are logarithmically enhanced. In these diagrams the photon is radiated either from the external tau or stau line or from a four–vertex, so that the loop integral is essentially the same as for the 2–body decay. If the photon is radiated off the heavy (s)quark loop, as in Fig. 2.3 (d,e), an additional heavy (s)quark propagator is introduced in this loop. In fact, the leading term in the HME of these diagrams is not $\mathcal{O}(1/f_a)$ but $\mathcal{O}(1/f_a^2)$ and thus strongly suppressed. Finally, the absence of a large logarithm $\log(y^2f_a^2/2\,m_{\widetilde{\tau}}^2)$ in the diagrams Fig. 2.3 (b,c) can be understood as follows: a logarithmic dependence on the heavy (s)quark mass corresponds to a UV divergence if the (s)quark mass becomes infinite, $m_{Q/\tilde{Q}_{1,2}} = y\,f_a/\sqrt{2} \to \infty$. When the (s)quark loop is integrated out, Fig. 2.3 (b,c) turn into one–loop diagrams with four propagators in the loop. One can see from simple power counting that these one–loop terms are UV finite so that the full two–loop contribution from Fig. 2.3 (b,c) cannot generate any large logarithms.

In [115], the 2– and 3–body decay rates were calculated using an effective theory where heavy (s)quark loops were integrated out. As mentioned above, this method leads to a logarithmic divergence in the result. As in [116], that logarithmic divergence was regulated with the cutoff f_a, and only the dominant contributions were kept. Moreover, the authors of [115] introduced a factor ξ and a mass scale m to parameterise the uncertainty associated with this cutoff procedure. The direct two–loop result now allows a direct connection with the parameters of the underlying model to be made, yielding agreement between (2.24) and the 3–body result of [115] for $\xi = 1$, $m = \sqrt{2}m_{\widetilde{\tau}}/y$ and $C_\mathrm{aYY} = 6e_Q^2$. The comparison of the 2–body results can be found in [23] and will also be addressed in Sec. 2.4.

The term in the last line of (2.24) has an infrared (IR) divergence for $x_\gamma \to 0$ and a collinear divergence for $\cos\theta \to 1$. These divergencies would be cancelled by the virtual three–loop correction to the 2–body decay channel. However, the calculation of this three–loop contribution is a formidable task and beyond the scope of this thesis. Furthermore, as will be shown below, the branching ratio of the 3–body mode is small

and has a minor effect on the total lifetime. Therefore, the three–loop contribution to the 2–body decay mode will have a similarly small effect and can be safely neglected. Nevertheless, our calculation of the 3–body decay mode provides a meaningful description of the energy and angular distributions of the photon (as long as x_γ and $1-\cos\theta$ do not become too small), which can be used for analysing this decay at colliders, see Chapter 4.

Because of the soft and collinear divergencies, the integrated 3–body rate with cuts on the scaled photon energy, $x_\gamma > x_\gamma^{\rm cut}$, and on the photon angle, $\cos\theta < 1 - x_\theta^{\rm cut}$, is considered

$$\Gamma(\widetilde{\tau}_{\rm R} \to \tau\widetilde{a}\gamma; x_\gamma^{\rm cut}; x_\theta^{\rm cut}) \equiv \int_{x_\gamma^{\rm cut}}^{1-A_{\widetilde{a}}} {\rm d}x_\gamma \int_{-1}^{1-x_\theta^{\rm cut}} {\rm d}\cos\theta \, \frac{{\rm d}^2\Gamma(\widetilde{\tau}_{\rm R} \to \tau\widetilde{a}\gamma)}{{\rm d}x_\gamma \, {\rm d}\cos\theta}. \tag{2.25}$$

Figure 2.5 shows the branching ratio of the integrated 3–body decay rate,

$${\rm BR}(\widetilde{\tau}_{\rm R} \to \tau\widetilde{a}\gamma; x_\gamma^{\rm cut}; x_\theta^{\rm cut}) \equiv \frac{\Gamma(\widetilde{\tau}_{\rm R} \to \tau\widetilde{a}\gamma; x_\gamma^{\rm cut}; x_\theta^{\rm cut})}{\Gamma_{\rm tot}^{\widetilde{\tau}_{\rm R}}}, \tag{2.26}$$

with

$$\Gamma_{\rm tot}^{\widetilde{\tau}_{\rm R}} \equiv \Gamma(\widetilde{\tau}_{\rm R} \to \tau\widetilde{a}) + \Gamma(\widetilde{\tau}_{\rm R} \to \tau\widetilde{a}\gamma; x_\gamma^{\rm cut}; x_\theta^{\rm cut}). \tag{2.27}$$

As can be seen from Fig. 2.5 (a), within reasonable ranges of $x_\gamma^{\rm cut}$ and $x_\theta^{\rm cut}$, the 3–body decay contributes only $\mathcal{O}(1\%)$ to the total decay rate. The latter is therefore well approximated by the 2–body contribution. For $A_{\widetilde{B}} \equiv m_{\widetilde{B}}^2/m_{\widetilde{\tau}}^2 \to 1$, the branching ratio (2.26) grows rapidly as shown in Fig. 2.5 (b) for $x_\gamma^{\rm cut} = x_\theta^{\rm cut} = 0.1$. This is because the dominant, logarithmically–enhanced part of $\Gamma(\widetilde{\tau}_{\rm R} \to \tau\widetilde{a}) \propto m_{\widetilde{\tau}}\, m_{\widetilde{B}}^2$ while $\Gamma(\widetilde{\tau}_{\rm R} \to \tau\widetilde{a}\gamma) \propto m_{\widetilde{\tau}}^3$. However, the branching ratio always stays below about 3.5% for $m_{\widetilde{\tau}} \lesssim 5\,{\rm TeV}$ and $x_\gamma^{\rm cut} = x_\theta^{\rm cut} = 0.1$. As long as $m_{\widetilde{a}}^2/m_{\widetilde{\tau}}^2 \ll 1$ the influence of $m_{\widetilde{a}}$ on the branching ratio is small. The product yf_a also determines the relative contribution of the one– and two–loop amplitudes to the 3–body decay rate. For the parameters in Fig. 2.5, both the one– and two–loop amplitudes are of roughly equal importance. Varying yf_a by one order of magnitude up or down changes the 3–body branching ratio by 2–10%.

2.3 4–body Decay

The 4–body decay modes $\widetilde{\tau}_{\rm R} \to \tau\widetilde{a}\gamma\gamma$, $\widetilde{\tau}_{\rm R} \to \tau\widetilde{a}l\bar{l}$ and $\widetilde{\tau}_{\rm R} \to \tau\widetilde{a}q\bar{q}$ have a negligible impact on the total stau decay rate since they are suppressed by an additional factor α compared to the 3–body decay. However, for $\tau_{\widetilde{\tau}} > 100$ s, hadronic energy injection [99–105] from $\widetilde{\tau}_{\rm R} \to \tau\widetilde{a}q\bar{q}$ decays can affect the abundances of primordial light nuclei

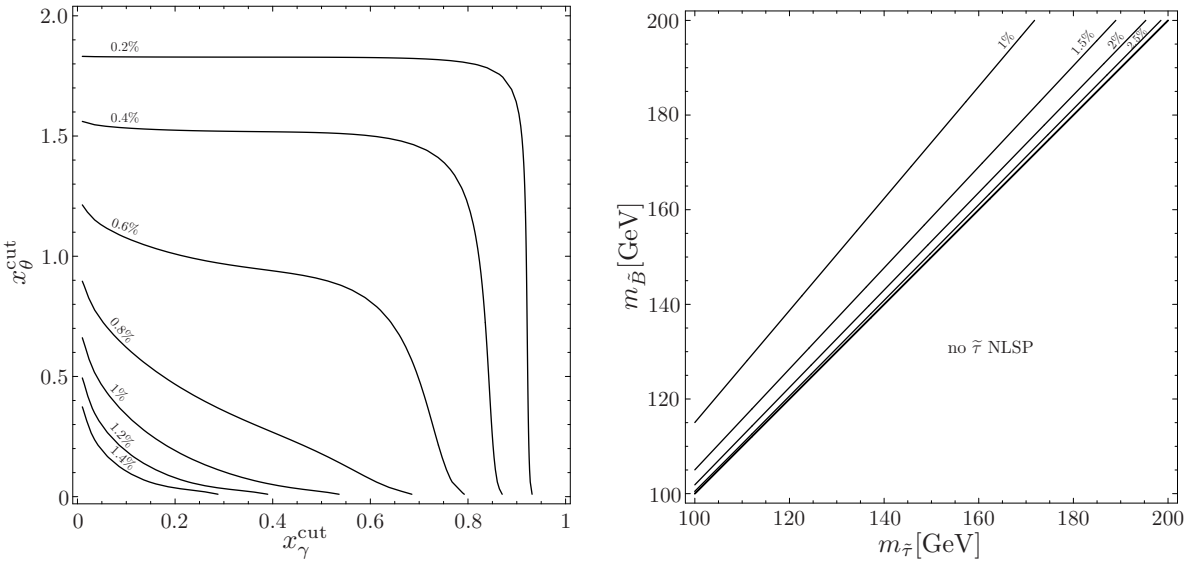

Figure 2.5: Branching ratio of the 3–body decay $\widetilde{\tau}_{\rm R} \to \tau\widetilde{a}\gamma$ as a function of (a) the soft and collinear cut parameters $x_\gamma^{\rm cut}$ and $x_\theta^{\rm cut}$ and (b) the masses $m_{\widetilde{\tau}}$ and $m_{\widetilde{B}}$. In both plots the other parameters are set to $m_{\widetilde{a}} = 10$ GeV, $f_a = 10^{11}$ GeV, $|e_Q| = 1/3$, $y = 1$, as well as $m_{\widetilde{\tau}} = 100$ GeV, $m_{\widetilde{B}} = 110$ GeV for the left figure, and $x_\gamma^{\rm cut} = x_\theta^{\rm cut} = 0.1$ for the right figure.

significantly, see Sec. 3.3. The evaluation of BBN constraints from this effect requires the calculation of the hadronic 4–body decays.

The Feynman diagrams for $\widetilde{\tau}_{\rm R} \to \tau\widetilde{a}q\bar{q}$ can be deduced from the diagrams in Fig. 2.3 by splitting the final state photon into a $q\bar{q}$ pair. In addition there are diagrams where this photon is replaced by a Z boson. These are explicitly shown in Fig. 2.6.

The one–loop contribution, see Fig. 2.6, has been calculated with the same HME techniques explained in the previous subsections. Again for the two–loop amplitude, only the terms $\propto \log(y^2 f_a^2/2m_{\widetilde{\tau}}^2)$ are retained. Following the arguments of the previous subsection, no such logarithmic term is generated from diagrams where the $(\gamma \to q\bar{q})$ or $(Z \to q\bar{q})$ is emitted from inside the loops. One has to consider only the two–loop diagrams where the γ, Z is emitted from the external stau or tau lines or is attached via a quartic coupling to the external and internal stau and the internal γ, Z (see also Fig. 1 of [24]). As a result, one can directly use the result for the 3–body decay without having to recompute the complete amplitude. As the only necessary modifications, the stau-γ/Z or tau-γ/Z splitting functions have to be added and the stau or tau momentum in the loop integrals moved off–shell. In this calculation the width of the Z boson is included by introducing a complex mass in the propagator, $m_Z^2 \to m_Z^2 - im_Z\Gamma_Z$.

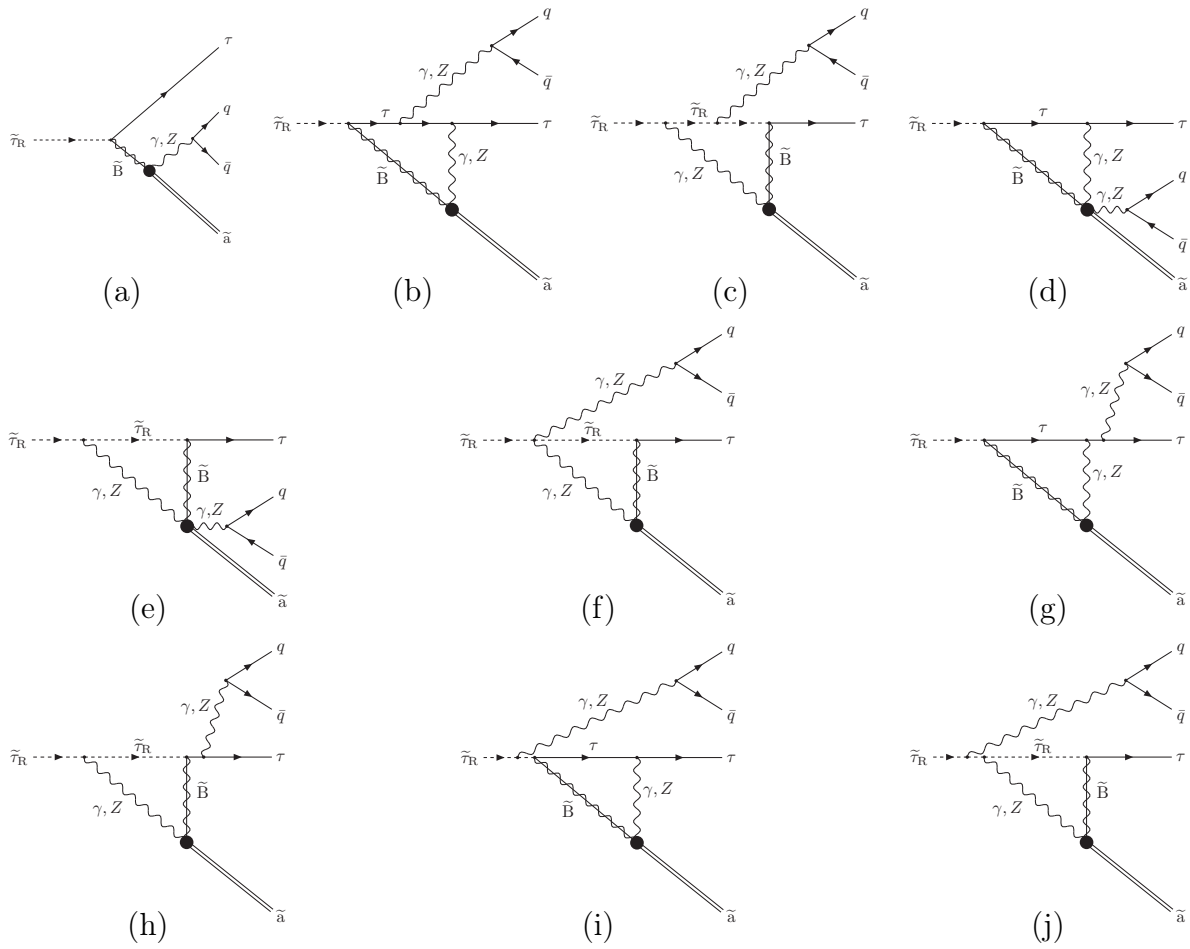

Figure 2.6: Feynman diagrams for the 4–body stau NLSP decay $\widetilde{\tau}_{\rm R} \to \tau \widetilde{a} q \bar{q}$ in KSVZ axion models, at one–loop (a) and two–loop (b-j) level. The blob indicates the heavy (s)quark loops.

The differential decay rate as a function of the $q\bar{q}$ invariant mass, $m_{q\bar{q}}$ is given by

$$\frac{\mathrm{d}\Gamma(\widetilde{\tau}_{\rm R} \to \tau \widetilde{a} q \bar{q})}{\mathrm{d}m_{q\bar{q}}} = \frac{1}{32 m_{\widetilde{\tau}}^2} \frac{1}{(2\pi)^8} \int \mathrm{d}m_{\tau V} \int \mathrm{d}\Omega_{\tilde{a}} \int \mathrm{d}\Omega'_V \int \mathrm{d}\Omega''_q \times |\boldsymbol{k}_{\tilde{a}}|\, |\boldsymbol{k}'_V|\, |\boldsymbol{k}''_q|\, |\mathcal{M}(\widetilde{\tau}_{\rm R} \to \tau \widetilde{a} q \bar{q})|^2, \tag{2.28}$$

where $m_{\tau V}$ is the invariant mass of the final state τ and the intermediate $V = \gamma, Z$ boson, $\Omega_{\tilde{a}}$ and $\boldsymbol{k}_{\tilde{a}}$ are the solid angle and 3–momentum of the axino in the $\widetilde{\tau}_{\rm R}$ rest frame, Ω'_V and $\boldsymbol{k}'_V$ are the solid angle and 3–momentum of the $V = \gamma, Z$ boson in the τV rest frame, and Ω''_q and $\boldsymbol{k}''_q$ are the solid angle and 3–momentum of the final state quark in the $V = \gamma, Z$ rest frame.

One of the solid angle integrations, say $\int \mathrm{d}\Omega_{\tilde{a}}$, is trivial and simply corresponds to a redefinition of the coordinate system. One additional azimuthal angle integration is

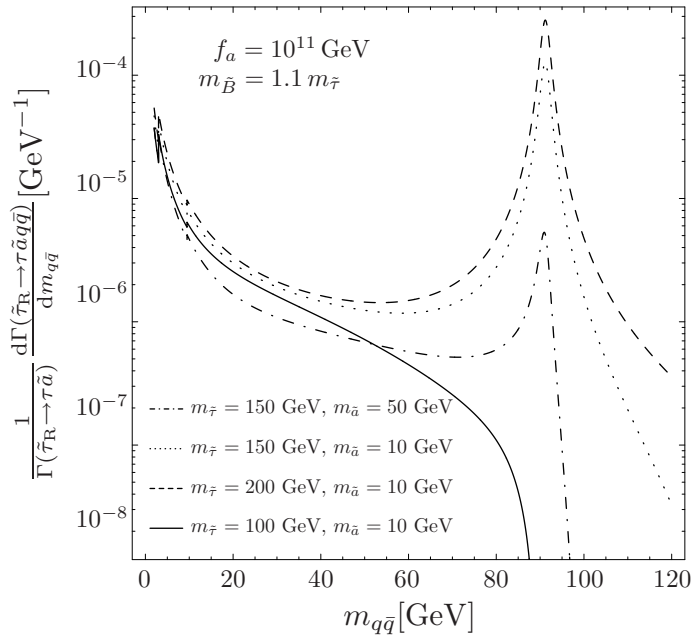

Figure 2.7: Energy spectrum of quark–antiquark pairs emitted from the 4–body decay $\widetilde{\tau}_\mathrm{R} \to \tau\widetilde{a}q\bar{q}$ with an invariant mass $m_{q\bar{q}}$, normalised to the 2–body decay rate, $\Gamma(\widetilde{\tau}_\mathrm{R} \to \tau\widetilde{a})$. The shown quantity is independent of e_Q. The other parameters are set to $m_{\widetilde{B}} = 1.1\,m_{\widetilde{\tau}}$, $f_a = 10^{11}$ GeV and $y = 1$.

also trivial since the incoming stau carries no polarisation. The integration over the angle of the final state $q\bar{q}$ pair yields, for massless quarks,

$$\int \mathrm{d}\Omega_q'' \; [\bar{u}(k_q)\gamma^\mu(v+a\gamma_5)u(k_{\bar{q}})]\,[\bar{u}(k_{\bar{q}})\gamma^\nu(v+a\gamma_5)u(k_q)] = \frac{16\pi}{3}\left(-g_{\mu\nu}k_V^2 + k_V^\mu k_V^\nu\right)(v^2+a^2), \tag{2.29}$$

where v and a are the respective vector and axial couplings and $k_V = k_q + k_{\bar{q}}$. The remaining integrations over $\cos\theta_V'$ and $m_{\tau V}$,

$$\begin{aligned}\frac{\mathrm{d}\Gamma(\widetilde{\tau}_\mathrm{R} \to \tau\widetilde{a}q\bar{q})}{\mathrm{d}m_{q\bar{q}}} = \frac{1}{128(2\pi)^6 m_{\widetilde{\tau}}^2}\,\frac{\lambda^{1/2}(m_{\widetilde{\tau}}^2, m_{\widetilde{a}}^2, m_{\tau V}^2)}{2m_{\widetilde{\tau}}}\,\frac{m_{\tau V}^2 - m_{q\bar{q}}^2}{2m_{\tau V}}\,\frac{m_{q\bar{q}}}{2} \\ \times \int_{-1}^{1} \mathrm{d}\cos\theta_V' \int_{m_{q\bar{q}}}^{m_{\widetilde{\tau}}-m_{\widetilde{a}}} \mathrm{d}m_{\tau V}\; |\hat{\mathcal{M}}|^2,\end{aligned} \tag{2.30}$$

need to be performed numerically. Here $\lambda(a,b,c) \equiv a^2+b^2+c^2-2(ab+ac+bc)$, θ_V' is the polar angle of Ω_V', and $|\hat{\mathcal{M}}|^2$ is the squared matrix element with the external quark current replaced by expression (2.29).

Figure 2.7 shows the obtained energy spectrum of the quark–antiquark pair stemming from the 4–body decay for several choices of the stau and axino masses, $m_{\widetilde{B}} = 1.1\,m_{\widetilde{\tau}}$ and $f_a = 10^{11}\,\mathrm{GeV}$. It is normalised to the 2–body decay width given by (2.14).

As evident from the figure the effect of the Z boson resonance becomes important only for $m_{\widetilde{\tau}} - m_{\widetilde{a}} \gtrsim 100$ GeV.

Since pions decay fast, the major impact of hadronic energy release on primordial nucleosynthesis stems from nucleons that hadronise from the $q\bar{q}$ pair (see Sec. 3.3). Therefore only $q\bar{q}$ pairs with $m_{q\bar{q}} > 2$ GeV are considered. Moreover, $c\bar{c}$ and $b\bar{b}$ pairs only contribute for invariant masses above the $J/\Psi(1S)$ resonance with $m_{J/\Psi,1S} = 3.0$ GeV and the $\Upsilon(1S)$ resonance with $m_{\Upsilon,1S} = 9.5$ GeV, respectively. The contribution from $t\bar{t}$ pairs is strongly suppressed due to the large threshold $m_{t\bar{t}} \gtrsim 350$ GeV. In the matrix element all quarks are taken to be massless. This approximation is justified by the behaviour of the cross section for $e^+e^- \to q\bar{q}$ as a function of the centre–of–mass energy, which is well described by step function thresholds for the heavy quarks.

2.4 Stau Lifetime

It has already been mentioned and shown that the branching ratios of the 3– and 4–body decays are very small. This means that the stau NLSP lifetime $\tau_{\widetilde{\tau}} = 1/\Gamma^{\widetilde{\tau}_R}_{\rm tot}$ can be very well estimated by the 2–body partial decay width alone, given by (2.14)

$$\Gamma^{\widetilde{\tau}_R}_{\rm tot} \approx \Gamma(\widetilde{\tau}_R \to \tau\widetilde{a}). \tag{2.31}$$

Indeed, the lifetime is dominated by the leading logarithmic (LL) term of the 2–body decay,

$$\Gamma(\widetilde{\tau}_R \to \tau\widetilde{a})_{\rm LL} = \frac{81\alpha^4\, e_Q^4}{512\pi^5\, c_W^8}\, \frac{m_{\widetilde{\tau}}}{f_a^2}(1 - A_{\tilde{a}})^2\, m_{\widetilde{B}}^2\, \log^2\left(\frac{y^2 f_a^2}{2m_{\widetilde{\tau}}^2}\right). \tag{2.32}$$

The mass of the axino enters only through the kinematics factor in this leading term, and the lifetime quickly becomes independent of $m_{\widetilde{a}}$ if it is sufficiently smaller than $m_{\widetilde{\tau}}$, i.e. when $A_{\tilde{a}}$ is small enough. Moreover, it is useful to look at the LL expression (2.32) to see analytically the dependency of the lifetime on the parameters of the underlying model. It is highly sensitive to the charge of the heavy (s)quarks $\tau_{\widetilde{\tau}_R} \propto 1/e_Q^4$, and less so to the Yukawa coupling y. With respect to the case in Fig. 2.9, $\tau_{\widetilde{\tau}}$ is thus reduced by a factor of 81 (16) for $|e_Q| = 1$ (2/3). On the other hand, if $e_Q = 0$, the decay of the $\widetilde{\tau}$ NLSP will require 4–loop diagrams involving gluons, gluinos, and ordinary (s)quarks, which would thus lead to significantly larger lifetimes than in Fig. 2.9.

Figure 2.8 shows the discrepancy between the LL approximation (2.32) and the full expression (2.14), $1 - \Gamma(\widetilde{\tau}_R \to \tau\widetilde{a})_{\rm LL}/\Gamma(\widetilde{\tau}_R \to \tau\widetilde{a})$, which is maximised for small f_a and $m_{\widetilde{a}}$, and large $m_{\widetilde{\tau}}$ and $m_{\widetilde{B}}$. This LL result (2.32) can be compared to Eqn. (2) obtained in [115], where a cut–off method [116] had been used to calculate the 2–body decay. Fixing the mass scale to $m = 100\,\text{GeV}$ as suggested in [115], the discrepancy is insensitive to f_a as, in the leading logarithm, it enters in the same way in both cases. However, due to the fixed mass scale used in [115] to account for the uncertainty of the

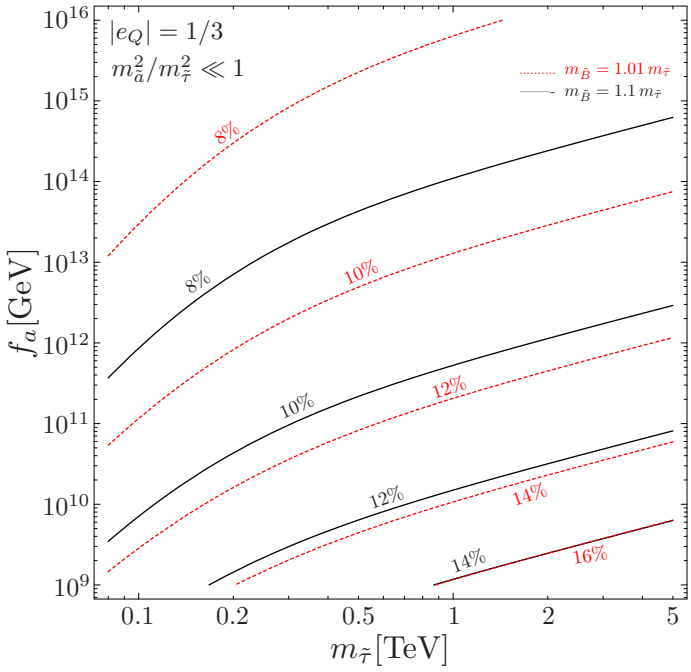

Figure 2.8: The discrepancy between the LL approximation (2.32) and full expression (2.14) for the 2–body decay of the stau NLSP, $1 - \Gamma(\widetilde{\tau}_{\rm R} \to \tau\widetilde{a})_{\rm LL}/\Gamma(\widetilde{\tau}_{\rm R} \to \tau\widetilde{a})$, for $m_{\widetilde{B}} = 1.1 m_{\widetilde{\tau}}$ (solid lines) and $m_{\widetilde{B}} = 1.01 m_{\widetilde{\tau}}$ (dotted lines). $|e_Q| = 1/3$, $y = 1$ and the limit $m_{\widetilde{a}}^2/m_{\widetilde{\tau}}^2 \ll 1$ is taken.

result, its discrepancy to the exact full result (2.14) can be much larger than that of the LL obtained in the calculation presented here. For this case, the error increases with increasing $m_{\widetilde{\tau}}$ and $m_{\widetilde{B}}$, and decreasing f_a. In general, it represents an overestimation of the exact result and the discrepancy reaches over 35% for $m_{\widetilde{\tau}} \approx 1\,\text{TeV}$, $m_{\widetilde{B}} = 2.0\, m_{\widetilde{\tau}}$ and $f_a \approx 10^9\,\text{GeV}$.

The stau lifetime (including the non–LL terms) is plotted in Fig. 2.9 as a function of its mass $m_{\widetilde{\tau}}$. It illustrates the sensitivity of the lifetime not only to $m_{\widetilde{\tau}}$ but also f_a and $m_{\widetilde{B}}$. The limit of $m_{\widetilde{a}}^2/m_{\widetilde{\tau}}^2 \ll 1$ is taken, where the effect of a changing $m_{\widetilde{a}}$ becomes negligible. For stau masses in the range that would be accessible at the LHC, and the allowed range of f_a (see introduction), one sees that the lifetime can range from about $10^{-4}\,\text{s}$ to $10^4\,\text{s}$. Note that lifetimes larger than $10^4\,\text{s}$ can be excluded by catalysed BBN, as will be shown in Sec. 3.3. This has implications both phenomenologically and cosmologically, which will be explored in the proceeding sections. In the analyses that follow, the full expression of the 2–body decay is used to calculate the stau NLSP lifetime. For demonstrative purposes, $|e_Q| = 1/3$ and $y = 1$ are generically set. Furthermore, the results are only shown for $m_{\widetilde{\tau}} \geq 80\,\text{GeV}$ [27], the limit set from searches for long–lived staus at the Large Electron Positron (LEP) collider.

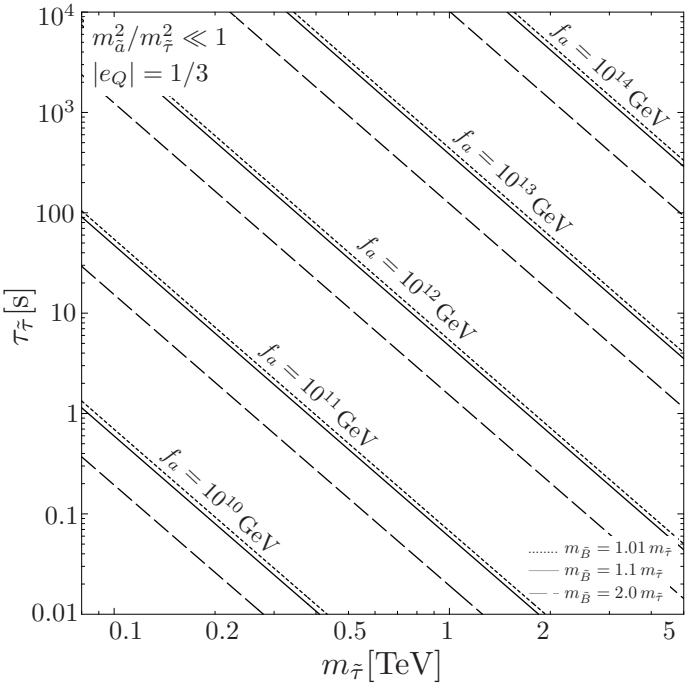

Figure 2.9: The lifetime of the stau NLSP as a function of $m_{\tilde{\tau}}$ for $m_a^2/m_{\tilde{\tau}}^2 \ll 1$, $|e_Q| = 1/3$, $y = 1$ and f_a values ranging from 10^{10} to 10^{14} GeV. The solid, dashed and dotted lines indicate $\tau_{\tilde{\tau}}$ for $m_{\tilde{B}} = 1.1\, m_{\tilde{\tau}}$, $m_{\tilde{B}} = 2.0\, m_{\tilde{\tau}}$ and $m_{\tilde{B}} = 1.01\, m_{\tilde{\tau}}$, respectively.

Chapter 3

Cosmological Constraints

In this chapter the results for the stau NLSP decays obtained in the previous chapter are used to systematically study cosmological constraints on axino dark matter scenarios. First the focus is placed on the relic axino density, which is constrained by the present dark matter density. Then the constraints from structure formation are explored, where upper limits on the present free–streaming velocities of axino dark matter emerge in order to respect the power spectrum observed at small scales. Lastly, the effects on big bang nucleosynthesis is studied, which can substantially constrain the parameter space of the considered hadronic axino model. Using these constraints, limits on the PQ scale f_a and the reheating temperature T_R can be derived.

For the following considerations, a standard thermal history with a post–inflationary reheating temperature in the range of $T_{\mathrm{f}}^{\widetilde{\tau}} < T_{\mathrm{R}} < f_a$ is assumed, where $T_{\mathrm{f}}^{\widetilde{\tau}} \sim m_{\widetilde{\tau}}/25$ is the freeze–out temperature of the staus, i.e. the temperature at which the staus decouple from the thermal bath in the early universe.* By considering $T_{\mathrm{R}} < f_a$, scenarios in which the PQ symmetry is not restored during or after reheating are picked out. In fact, the PQ symmetry is assumed to be broken before inflation and not restored afterwards. For large f_a, the relic axion density Ω_a is governed by the initial misalignment angle Θ_i of the axion field with respect to the CP–conserving position (see [49, 66] and references therein). This allows the presented dark matter density constraints to be kept conservative by assuming $\Omega_a \ll \Omega_{\mathrm{dm}}$ which is possible even for f_a above $10^{14}\,\mathrm{GeV}$ since Θ_i can be sufficiently small. Depending on the model, the saxion – which is the bosonic partner of the axino that appears in addition to the axion – can be a late decaying particle and as such be associated with significant entropy production [71–73, 117]. This could affect cosmological constraints [118] including those considered in this work. Leaving a study of saxion effects for future work, a standard thermal history is assumed in this thesis. Those effects can then be considered negligible.

*T_{R} is referred to as the initial temperature of the radiation–dominated epoch. Relations to T_{R} definitions in terms of the decay width of the inflaton field can be established in the way presented explicitly for the $\widetilde{G}$ LSP case in [97].

3.1 Constraints from the Present Dark Matter Density

In this section, the constraints on the relic axino density from the dark matter density [119, 120]

$$\Omega_{\rm dm}^{3\sigma} h^2 = 0.105^{+0.021}_{-0.030}, \tag{3.1}$$

as obtained from the measurements of the CMB anisotropies by the WMAP satellite, with $h = 0.73^{+0.04}_{-0.03}$ denoting the Hubble constant in units of $100\,{\rm km\,Mpc^{-1}\,s^{-1}}$, are discussed. Note that this nominal 3σ range is derived assuming the six–parameter flat ΛCDM model briefly described in Sec. 1.2.1, and in more detail in [119]† . If the fit is performed in the context of a more general model, a larger range is possible even with additional data from other cosmological probes [122].

The primordial origin of axinos is dependent on the history of the universe and the particle physics model. The thermal history considered here is as described above and it is further assumed that all axinos that existed before inflation were diluted away during the slow–roll phase, such that the density becomes negligible at the start of the reheating period. The dark matter density (3.1) constrains the relic axino density

$$\Omega_{\widetilde{a}} = \Omega_{\widetilde{a}}^{\rm therm/TP} + \Omega_{\widetilde{a}}^{\rm NTP} \leq \Omega_{\rm dm} - \Omega_a, \tag{3.2}$$

where contributions from thermal relic (therm) or thermally produced (TP) axinos and from non–thermally produced (NTP) axinos from stau NLSP decays are included.

The freeze–out temperature of the axino $T_{\rm f}^{\widetilde{a}}$ can be very high due to its extremely weak interactions. For example, $T_{\rm f}^{\widetilde{a}} \sim 10^9\,{\rm GeV}$ ($10^{11}\,{\rm GeV}$) has been found for $f_a = 10^{11}\,{\rm GeV}$ ($10^{12}\,{\rm GeV}$) [123–125]. For a reheating temperature $T_{\rm R} > T_{\rm f}^{\widetilde{a}}$, axinos were initially in thermal equilibrium with the primordial plasma, and decoupled while still relativistic, at $T_{\rm f}^{\widetilde{a}} \gg m_{\widetilde{a}}$. Accordingly, the resulting thermal relic axino density is given by [123–126]

$$\Omega_{\widetilde{a}}^{\rm therm} h^2 = 0.05 \left(\frac{230}{g_{*S}(T_{\rm f}^{\widetilde{a}})}\right) \left(\frac{m_{\widetilde{a}}}{100\,{\rm eV}}\right), \tag{3.3}$$

$$\approx m_{\widetilde{a}}/(2\,{\rm keV}), \tag{3.4}$$

where $g_{*S}(T_{\rm f}^{\widetilde{a}})$ is the number of effectively massless degrees of freedom at decoupling. As $T_{\rm f}^{\widetilde{a}}$ is typically very high, all particles in the MSSM can be considered as relativistic at this time, and with the addition of the axion and the axino, $g_{*S}(T_{\rm f}) \approx 230$ can be used, which leads to (3.4) above. The constraint (3.2) thus translates into $m_{\widetilde{a}} \lesssim 0.2\,{\rm keV}$ [123]

†The updated values fitted to WMAP5 [121] and WMAP7 [19] data have also been published and are consistent with the WMAP3 value used here.

even in the most conservative case with $\Omega_{\widetilde{a}}^{\rm NTP} + \Omega_a \ll \Omega_{\rm dm}$. As will be shown in Sec. 3.2, this places thermal relic axinos in the 'hot' dark matter category, where even more restrictive constraints apply. It should however be noted that an axion cold dark matter scenario, $\Omega_a \approx \Omega_{\rm dm}$, in which thermal relic axinos with $m_{\widetilde{a}} \ll 0.2\,{\rm keV}$ provide a tolerable contribution to hot dark matter, is a viable option [125].

For $T_{\rm R} < T_{\rm f}^{\widetilde{a}}$, the axinos were never in thermal equilibrium with the thermal bath but can still be produced via scattering of coloured particles in the hot MSSM plasma [124–128]. Working within the framework of SUSY QCD, hard thermal loop (HTL) resummation and the Braaten–Yuan prescription [129] have been used to calculate the rate of this thermal axino production in a gauge–invariant way. The result is consistent to leading order in the strong coupling $\alpha_{\rm s} = g_{\rm s}^2/4\pi$ [125]. Considering $T_{\rm R}$ as the initial temperature of the radiation–dominated epoch, this rate leads to the following expression for the relic density [23, 125]

$$\Omega_{\widetilde{a}}^{\rm TP} h^2 = 5.5\, g_{\rm s}^6(T_{\rm R}) \log\left(\frac{1.211}{g_{\rm s}(T_{\rm R})}\right)\left(\frac{m_{\widetilde{a}}}{0.1\,{\rm GeV}}\right)\left(\frac{10^{11}\,{\rm GeV}}{f_{\rm a}}\right)^2\left(\frac{T_{\rm R}}{10^4\,{\rm GeV}}\right), \qquad (3.5)$$

where $g_s(T_{\rm R}) = \sqrt{4\pi\alpha_s(T_{\rm R})}$ is evaluated according to its 1–loop renormalisation group running within the MSSM from $\alpha_s(m_Z) = 0.1176$ at $m_Z = 91.1876$ GeV. In this study, (3.5) is used since it emerges from a gauge–invariant treatment that is consistent to leading order in g_s. Note however that this treatment relies on the weak coupling limit, $g_{\rm s} \ll 1$, and thus on high temperatures, $T \gg 10^4\,{\rm GeV}$ [125].‡

The TP relic density is sensitive to $T_{\rm R}$ and f_a and can therefore provide a means through which the reheating temperature and/or the Peccei–Quinn scale can be probed [130]. By constraining $\Omega_{\widetilde{a}}^{\rm TP}$ with (3.2), upper limits on $T_{\rm R}$ are obtained for given $m_{\widetilde{a}}$ and f_a (or equivalently lower limits on f_a for given $m_{\widetilde{a}}$ and $T_{\rm R}$) [23,118,125,126,128,130,131]. For (3.5) and $\Omega_{\widetilde{a}}^{\rm NTP} + \Omega_a \ll \Omega_{\rm dm}$, these limits are explored in Sec. 3.5. For example, insisting on a high reheating temperature of $T_{\rm R} \gtrsim 10^9\,{\rm GeV}$, which is desirable when considering the viability of standard thermal leptogenesis, and on axinos being cold dark matter, $m_{\widetilde{a}} \gtrsim 100\,{\rm keV}$ (explored more in Sec. 3.2), fairly high f_a values of $f_a > 3\times10^{12}\,{\rm GeV}$ [23] must be considered. Note however, that the study in this thesis is not constrained to any specific baryogenesis scenario or range of f_a values other than (1.26).

Along with the thermal relic or thermally produced axinos, there are also non–thermally produced axinos from out–of–equilibrium NLSP decays. Due to the highly suppressed coupling of the axino to MSSM particles, the stau NLSP is long–lived enough such that the other SUSY particles would have cascade–decayed to the stau by the time the staus themselves are decaying (see Chapter 2). This occurs typically after its freeze–out, i.e. when $T \ll T_{\rm f}^{\widetilde{\tau}}$. Thus only the yield of the stau NLSP after freeze–out has to

‡For alternative approaches that also consider thermal axion production at lower temperatures, see [127,128] where [128] also includes an additional squark–squark–gluino–axino vertex and a different $T_{\rm R}$ definition.

be considered,

$$Y_{\widetilde{\tau}} \equiv \frac{n_{\widetilde{\tau}_{\rm R}}}{s} = 2Y_{\widetilde{\tau}_{\rm R}^-}, \tag{3.6}$$

where s is the total entropy density of the universe and $n_{\widetilde{\tau}_{\rm R}}$ is the total number density for an equal number density of positively and negatively charged $\widetilde{\tau}_{\rm R}$ sleptons, that is, the number density that the stau NLSP would have today, if it had not decayed. As each stau decays into one axino, the relic density of the axino from this non–thermal production is given by the following expression [132]

$$\Omega_{\widetilde{a}}^{\rm NTP} h^2 = m_{\widetilde{a}}\, Y_{\widetilde{\tau}}\, s(T_0) h^2/\rho_{\rm c}, \tag{3.7}$$

where $\rho_{\rm c}/[s(T_0)h^2] = 3.6 \times 10^{-9}\,{\rm GeV}$ as obtained from the critical density $\rho_{\rm c}/h^2 = 8.1 \times 10^{-47}\,{\rm GeV}^4$, the present temperature $T_0 = 2.73\,{\rm K} \equiv 2.35 \times 10^{-13}\,{\rm GeV}$ and the number of effectively massless degrees of freedom governing the entropy density today $g_{*S}(T_0) = 3.91$.

The stau NLSP yield $Y_{\widetilde{\tau}}$ can be calculated numerically and is model–dependent. For the purposes of the work in this thesis, with the focus on the $\widetilde{\tau}_{\rm R}$ NLSP setting, the following three characteristic approximations are considered:

$$Y_{\widetilde{\tau}} \simeq \kappa \times 10^{-12} \left(\frac{m_{\widetilde{\tau}}}{1\ {\rm TeV}}\right), \quad \kappa = 0.7,\ 1.4,\ 2.0, \tag{3.8}$$

where κ quantifies representative differences in the yield due to possible mass degeneracies of the stau NLSP to other sparticles and hence the extent of coannihilation. The value $\kappa = 0.7$ corresponds to the case with $m_{\widetilde{B}} = 1.1\, m_{\widetilde{\tau}}$ and $m_{\widetilde{\tau}} \ll m_{\tilde{\rm e},\tilde{\mu}}$, in which primordial stau annihilation involves only (anti–)staus in the initial state [133].[§] The yield associated with $\kappa = 1.4$ is encountered if there is either additional stau–slepton coannihilation corresponding to $m_{\widetilde{\tau}} \lesssim m_{\tilde{\rm e},\tilde{\mu}} < 1.1\, m_{\widetilde{\tau}}$ [133] or additional stau–bino coannihilation corresponding to $m_{\widetilde{\tau}} \lesssim m_{\widetilde{B}} < 1.1\, m_{\widetilde{\tau}}$ (see $Y_{\widetilde{\tau}}$ contours close to the dashed line in the right panel of Fig. 3 in [97]). For an approximate degeneracy of $m_{\widetilde{\tau}}$ with both $m_{\tilde{\rm e},\tilde{\mu}}$ and $m_{\widetilde{B}}$, simultaneous stau–slepton–bino coannihilation can lead to an even larger yield with $\kappa = 2$ in (3.8) (see $Y_{\widetilde{\tau}}$ contours close to the dashed line in the left panel of Fig. 3 of [97]). These κ values have been checked to be easily obtainable for appropriate constrained MSSM (CMSSM) points using micrOMEGAs 2.4 [134, 135]. More details on this are given in Chapter 4.

Putting the above together, (3.2) can be rewritten to obtain the dark matter constraint on the stau abundance prior to decay, $Y_{\widetilde{\tau}} \leq Y_{\widetilde{\tau}\,{\rm dm}}^{\rm max}$ with

$$Y_{\widetilde{\tau}\,{\rm dm}}^{\rm max} = 4.5 \times 10^{-11} \left(\frac{\Omega_{\rm dm}^{\rm max} - \Omega_{\widetilde{a}}^{\rm TP} - \Omega_a}{0.126/h^2}\right) \left(\frac{10\ {\rm GeV}}{m_{\widetilde{a}}}\right). \tag{3.9}$$

Figure 3.1 shows the corresponding constraints on $m_{\widetilde{a}}$ and $m_{\widetilde{\tau}}$ that emerge when (3.8)

[§]The bino mass $m_{\widetilde{B}} = 1.1\, m_{\widetilde{\tau}}$ considered in [133] represents a typical mass splitting in regions with $m_{\widetilde{B}} > m_{\widetilde{\tau}}$ encountered in scenarios such as the constrained MSSM (CMSSM).

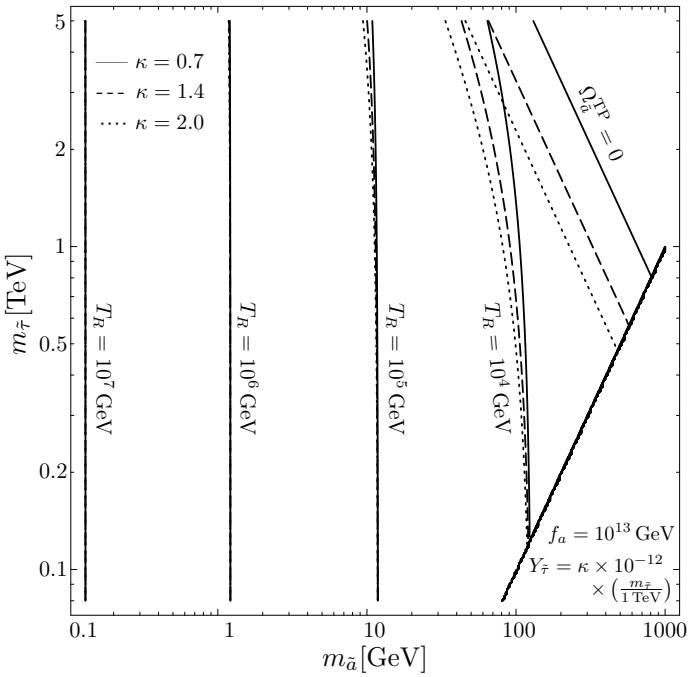

Figure 3.1: Constraint imposed by $\Omega_{\tilde{a}}^{\rm TP}h^2 + \Omega_{\tilde{a}}^{\rm NTP}h^2 \leq 0.126$ for $f_a = 10^{13}\,\text{GeV}$, $T_{\rm R} = 10^7$, 10^6, 10^5, $10^4\,\text{GeV}$, and $T_{\rm R}$ such that $\Omega_{\tilde{a}}^{\rm TP}$ is negligible. The solid, dashed, and dotted lines are obtained for the thermal relic stau yield (3.8) with $\kappa = 0.7$, 1.4 and 2.0, respectively. For given $T_{\rm R}$ and κ, the region to the right of the corresponding line is disfavoured by the dark matter constraint.

is confronted with (3.9) for $\Omega_{\rm dm}^{\rm max}h^2 = 0.126$, $\Omega_a \ll \Omega_{\rm dm}$, $f_a = 10^{13}\,\text{GeV}$, and $T_{\rm R} = 10^7$, 10^6, 10^5, $10^4\,\text{GeV}$, and a sufficiently small $T_{\rm R}$ value, where $\Omega_{\tilde{a}}^{\rm TP}$ can be neglected. The solid, dashed, and dotted lines are obtained for $\kappa = 0.7$, 1.4 and 2.0, respectively. The disfavoured region is the one to the right of the respective curve. Differences with respect to κ become visible/significant only for $m_{\tilde{a}} > 10$ GeV, which illustrates that $\Omega_{\tilde{a}}^{\rm NTP}$ is negligible for $m_{\tilde{a}} \lesssim 10$ GeV in the considered $m_{\tilde{\tau}}$ range. By increasing (decreasing) f_a by one order of magnitude, the $T_{\rm R}$ value at a given curve will increase (decrease) by two orders of magnitude. Note that the curves can also be read as the upper limits on $T_{\rm R}$ that are imposed by the dark matter constraint (3.2) for given $m_{\tilde{a}}$, $m_{\tilde{\tau}}$, and κ when $\Omega_a \ll \Omega_{\rm dm}$.

In this and the next three sections, the scenario with $T_{\rm f}^{\tilde{a}} > T_{\rm R}$ is focused on, taking the most conservative point of view with $\Omega_{\tilde{a}}^{\rm TP} + \Omega_a \ll \Omega_{\rm dm}$ (i.e. with sufficiently small $T_{\rm R}$ and Θ_i) when showing the dark matter constraint. By confronting (3.9) with $Y_{\tilde{\tau}}$, as described by (3.8), the associated constraint will then disfavour $m_{\tilde{a}}$ and $m_{\tilde{\tau}}$ combinations that are located above/to the right of the grey bands in the figures that follow. Note however, that the behaviour of the dark matter constraint for sizeable $T_{\rm R}$ leading to sizeable $\Omega_{\tilde{a}}^{\rm TP}$ can easily be inferred from Fig. 3.1.

A more phenomenologically–driven approach can also be considered where all of the

observed dark matter density is assumed to be composed of axinos from NLSP decays, $\Omega_{\rm dm} \simeq \Omega_{\widetilde{a}}^{\rm NTP}$. Irrespective of the freeze–out behaviour of the stau NLSP, this requires the following yield

$$Y_{\widetilde{\tau}} = 3.75 \times 10^{-11} \left(\frac{\Omega_{\rm dm}}{0.105/h^2} \right) \left(\frac{10 \text{ GeV}}{m_{\widetilde{a}}} \right), \tag{3.10}$$

(and again $T_{\rm R}$ and Θ_i sufficiently small such that $\Omega_{\widetilde{a}}^{\rm TP} + \Omega_a \ll \Omega_{\rm dm}$). For small values of $m_{\widetilde{a}}$, typical values of the thermal relic stau yield, as described by (3.8), cannot reach (3.10). The higher yield can however be accounted for by additional non–standard sources of staus such as late–decaying scalar fields. While the dark matter constraint in this case is fulfilled by construction, the region in which (3.10) agrees with typical thermal relic $Y_{\widetilde{\tau}}$ values are then indicated by grey bands. This will be referred to as the non–standard production scenario.

3.2 Constraints from Structure Formation

Let us now address the constraints on axino dark matter scenarios imposed by the matter power spectrum and related studies. Depending on details of their primordial origin, axinos can fall into the categories of cold, warm, and hot dark matter. As warm dark matter (WDM) or hot dark matter (HDM), they can be associated with significant suppression of structures on scales below a potentially sizeable comoving free–streaming scale $\lambda_{\rm FS}$. Studies of cosmic structures can thus provide upper limits on $\lambda_{\rm FS}$ or equivalently, on the present free–streaming velocity $v_{\rm FS}^0$ of axino dark matter. Various limits on $v_{\rm FS}^0$ obtained in WDM studies are compiled and confronted with the free–streaming velocities obtained for thermal relic axinos, thermally produced axinos, and axinos from stau NLSP decays.

In WDM investigations of cosmic structure formation, it is typically assumed that all dark matter consists of one species with mass $m_{\rm WDM}$ that was once in thermal equilibrium with the primordial plasma and freezes out while relativistic at $T_{\rm f}^{\rm WDM} \gg m_{\rm WDM}$. Correspondingly, for a Majorana fermion of spin 1/2, $\Omega_{\rm WDM}h^2$ is given by (3.3) after the obvious substitutions, where $g_{*S}(T_{\rm f}^{\rm WDM})$ is now fixed by the requirement $\Omega_{\rm WDM} = \Omega_{\rm dm}$ for a given $m_{\rm WDM}$. With an initial root mean squared momentum at freeze–out of $\langle p(T_{\rm f}^{\rm WDM})\rangle = 3.151\, T_{\rm f}^{\rm WDM}$, the present root mean squared free–streaming velocity is governed by $m_{\rm WDM}$:

$$(v_{\rm FS}^{\rm rms,0})^{\rm WDM} = 0.75\,{\rm km\,s^{-1}} \left(\frac{\Omega_{\rm dm}h^2}{0.105} \right)^{1/3} \left(\frac{100 \text{ eV}}{m_{\rm WDM}} \right)^{4/3}. \tag{3.11}$$

Using this expression, the upper limits on $v_{\rm FS}^0$ listed in Table 3.1 are obtained from the respective WDM constraints provided in the literature in terms of a lower limit on

Probe	$m_{\rm WDM}^{\rm min}$ [keV]	$(v_{\rm FS}^{\rm rms,0})^{\rm max}$ [km/s]	$(\lambda_{\rm FS})^{\rm max}$ [Mpc]	Reference
Number of MW satellites	2.1	0.01	0.12	[140]
Luminosity function of MW satellites	1	0.03	0.32	[141]
Phase space density in dSphs	0.7	0.06	0.59	[142]
Phase space density in dSphs	0.6–1.5	0.02–0.07	0.22–0.67	[143]
Lyman-α forest ($z \simeq 3$)	0.75	0.05	0.50	[144]
Lyman-α forest ($z \simeq 2-3$)	0.55	0.08	0.76	[145]
Lyman-α forest ($2.2 < z < 4.2$)	2	0.01	0.12	[146]
Lyman-α forest ($2.0 < z < 6.4$)	4	0.005	0.06	[147]

Table 3.1: A selection of constraints on WDM particles from observations and numerical simulations. The lower limits on $m_{\rm WDM}$ are taken from the corresponding references. The values for $(v_{\rm FS}^{\rm rms,0})^{\rm max}$ and $(\lambda_{\rm FS})^{\rm max}$ are derived from $m_{\rm WDM}^{\rm min}$ using (3.11) and (3.12), respectively.

$m_{\rm WDM}$. In Table 3.1 each limit is also given in terms of an upper limit on the free–streaming scale, which can be estimated by calculating the redshift of the velocity of the particle from the time of production to the time when the Jeans mass instability starts to take effect, i.e. at the time of matter–radiation equality [136]

$$\lambda_{\rm FS} \simeq \int_0^{t_{\rm eq}} dt\, \frac{v(t)}{a(t)} = 2 v_{\rm FS}^0\, t_{\rm eq}\, (1+z_{\rm eq})^2\, \log\left(\sqrt{1 + \frac{1}{(v_{\rm FS}^0)^2 (1+z_{\rm eq})^2}} + \frac{1}{v_{\rm FS}^0 (1+z_{\rm eq})} \right), \tag{3.12}$$

with the cosmic scale factor $a(t)$, the dark matter velocity $v(t) = |\vec{p}(t)|/\sqrt{|\vec{p}(t)|^2 + m_{\rm WDM}^2}$ and its present free–streaming velocity $v_{\rm FS}^0$, which is assumed to be non–relativistic. The time and redshift at matter–radiation equality are given, respectively, by

$$z_{\rm eq} = 3082 \quad \text{and} \quad t_{\rm eq} = 2.0 \times 10^{12}\,{\rm s}, \tag{3.13}$$

where the values have been calculated for a cosmological model with matter density $\Omega_{\rm m} = 0.24$, radiation density $\Omega_\gamma = 4.6 \times 10^{-5}$, and cosmological constant $\Omega_\Lambda = 0.73$, as derived from WMAP3 data. Note that the relation (3.12) between $\lambda_{\rm FS}$ and $v_{\rm FS}^0$ is obtained in the limit that the considered dark matter population was produced (or decoupled from the primordial plasma) at t_i much before radiation–matter equality, i.e. for $t_i \ll t_{\rm eq}$ [137–139]. The derivations of the above equations, as well as the expressions for the free–streaming velocity that follow, can be found in Appendix B.

Table 3.1 lists representative limits inferred from from various astrophysical observations and studies of structure formation in WDM cosmologies. Included are constraints from the number of Milky Way (MW) satellites [140] and their luminosity function [141].

Here insights into the number and properties of satellite galaxies around the MW are taken into account which became accessible due to the results of the Sloan Digital Sky Survey (SDSS) only recently. Another source for the $m_{\rm WDM}^{\rm min}$ constraint is the maximum observed phase space density in dwarf spheroidal galaxies (dSphs) [142,143]. Moreover, one of the most sensitive probes is the Lyman–α forest. Associated studies give some of the most constraining limits on the thermal WDM mass [144–147]. The data are available over a large range of redshifts z and allow for the study of the power spectrum down to very small scales. In particular, [147] uses High Resolution Echelle Spectrometer (HIRES) data in combination with data from SDSS to place a lower limit on the WDM mass of $m_{\rm WDM} \gtrsim 4$ keV. As can be seen in Table 3.1, this 4 keV limit is significantly larger than the limits coming from other observations. The spread in the $m_{\rm WDM}$ limits reflects that WDM constraints are subject to ongoing research. In the following, some focus is placed on

$$m_{\rm WDM} \gtrsim 1 \text{ keV} \quad \equiv \quad v_{\rm FS}^{\rm rms,0} \lesssim 0.03 \text{ km/s} \quad \text{(conservative)}, \tag{3.14}$$

$$m_{\rm WDM} \gtrsim 4 \text{ keV} \quad \equiv \quad v_{\rm FS}^{\rm rms,0} \lesssim 0.005 \text{ km/s} \quad \text{(most restrictive)}. \tag{3.15}$$

These two limits will also indicate the range into which most of the limits that are given in Table 3.1 fall.

For thermal relic axinos which freeze–out with a mean squared momentum of $\langle p(T_{\rm f}^{\widetilde{a}})\rangle = 3.151\, T_{\rm f}^{\widetilde{a}}$, the root mean squared value of their present free–streaming velocity is given by

$$(v_{\rm FS}^{\rm rms,0})_{\widetilde{a}}^{\rm therm} = 0.57\,{\rm km\,s^{-1}} \left(\frac{230}{g_{*S}(T_{\rm f}^{\widetilde{a}})}\right)^{1/3} \left(\frac{100 \text{ eV}}{m_{\widetilde{a}}}\right). \tag{3.16}$$

Thus, the axino mass limit derived from the dark matter density constraint in Sec. 3.1, $m_{\widetilde{a}} \lesssim 0.2\,{\rm keV}$, implies $(v_{\rm FS}^{\rm rms,0})_{\widetilde{a}}^{\rm therm} \gtrsim 0.3$ km/s which is an order of magnitude above the conservative limit (3.14), i.e. thermal relic axinos would suppress small–scale structure too much. They are thus considered too 'hot' and are disfavoured as the dominant component of today's dark matter density. Nevertheless, they can provide hot dark matter in addition to neutrinos and can coexist with some other species providing the cold dark matter such as axions. In such a setting, the limit from [145] on the mixed scenario can be adopted which in the thermal relic axino case becomes $m_{\widetilde{a}} \lesssim 36$ eV since $g_{*S}(T_{\rm f}^{\widetilde{a}}) \simeq 230$.

For thermally produced axinos, their mean squared momentum is estimated at the reheating temperature $T_{\rm R}$, where their production is most efficient, as $\langle p(T_{\rm R})\rangle = 3.151\, T_{\rm R}$. Although never in thermal equilibrium, this choice is motivated by the fact that these axinos are produced in the scattering of particles that are in thermal equilibrium with the primordial plasma. Accordingly $(v_{\rm FS}^{\rm rms,0})_{\widetilde{a}}^{\rm TP}$ is estimated by (3.16) after the substitution $T_{\rm f}^{\widetilde{a}} \to T_{\rm R}$. As mentioned in the previous section, $g_{*S} \approx 230$ can be

used for large $T_{\rm R}$. Clearly, for $m_{\widetilde{a}} \gtrsim 100\,\text{keV}$, the present free–streaming velocity of these thermally produced axinos is well below the constraints shown in Table 3.1, which places them into the category of cold dark matter. For 12 keV $\lesssim m_{\widetilde{a}} < 100\,\text{keV}$, thermally produced axinos can be considered as WDM but will still be compatible with the most restrictive limit in Table 3.1: $(v_{\rm FS}^{\rm rms,0})_{\widetilde{a}}^{\rm TP} \lesssim 0.005$ km/s. The more conservative limit (3.14) would even allow for $m_{\widetilde{a}}$ as light as about 2 keV. This can become relevant for models of inflation and baryogenesis in axino dark matter scenarios with $\Omega_{\widetilde{a}}^{\rm TP} \simeq \Omega_{\rm dm}$: the lighter the $m_{\widetilde{a}}$ allowed by structure formation the higher will be the $T_{\rm R}$ value allowed by the dark matter constraint (3.2) for a given f_a, see also Fig. 3.1 above and Sec. 3.5.

For axinos produced non–thermally in stau NLSP decays, the present free–streaming velocity $(v_{\rm FS}^0)_{\widetilde{a}}^{\rm NTP}$ can be inferred from the 2-body stau decay calculated in Chapter 2. Since the 2-body decay is the dominant decay channel, most non–thermally produced axinos have an initial momentum given by

$$|\vec{p}_{\widetilde{a}}(t_i)| = \frac{m_{\widetilde{\tau}}^2 - m_{\widetilde{a}}^2 - m_\tau^2}{2\,m_{\widetilde{\tau}}}. \tag{3.17}$$

By considering the redshift of (3.17) due to the expansion of the universe, their present free–streaming velocity [148] is then obtained

$$(v_{\rm FS}^0)_{\widetilde{a}}^{\rm NTP} = \frac{T_0}{m_{\widetilde{a}}}\,\frac{m_{\widetilde{\tau}}^2 - m_{\widetilde{a}}^2 - m_\tau^2}{2m_{\widetilde{\tau}}}\left(\frac{g_{*S}(T_0)}{g_{*S}(\tau_{\widetilde{\tau}})}\right)^{1/3}\left(\frac{4\pi^2 g_*(\tau_{\widetilde{\tau}})\tau_{\widetilde{\tau}}^2}{90\,\text{M}_{\rm Pl}^2}\right)^{1/4}, \tag{3.18}$$

which is valid in the usual case that they are produced during the radiation–dominated epoch, $t_i \ll t_{\rm eq}$, and that they are non–relativistic today, $|\vec{p}_{\widetilde{a}}(t_0)| = m_{\widetilde{a}} v_0$. Here $\text{M}_{\rm Pl} = 2.4 \times 10^{18}\,\text{GeV}$ is the reduced Planck mass, and $g_*(\tau_{\widetilde{\tau}})$ and $g_{*S}(\tau_{\widetilde{\tau}})$ are the effective number of relativistic degrees of freedom governing the energy density and entropy density, respectively, at the time the stau NLSP decays into the axino LSP. For example, if the staus decay after electrons and positrons become non–relativisic, $g_{*S}(\tau_{\widetilde{\tau}}) = g_{*S}(T_0) = 3.91$ and $g_*(\tau_{\widetilde{\tau}}) = g_*(T_0) = 3.36$. Note that the sudden decay approximation is used in which all staus are considered to simultaneously decay at time $t_i = \tau_{\widetilde{\tau}}$.[¶] In the following, the full result (2.14) is used to calculate $(v_{\rm FS}^0)_{\widetilde{a}}^{\rm NTP}$ in the limit $m_\tau \to 0$. Nevertheless, the main features are already described by the following estimate obtained with the LL approximation (2.32),

$$\begin{aligned}(v_{\rm FS}^0)_{\widetilde{a}}^{\rm NTP} \approx\; & 90\,\text{km}\,\text{s}^{-1}\left[\log\left(\frac{y^2 f_a^2}{2m_{\widetilde{\tau}}^2}\right)\right]^{-1}\left(\frac{1/3}{e_Q}\right)^2\left(\frac{f_a}{10^{13}\,\text{GeV}}\right)\left(\frac{1\,\text{GeV}}{m_{\widetilde{a}}}\right) \\ & \times\left(\frac{m_{\widetilde{\tau}}}{100\,\text{GeV}}\right)^{1/2}\left(\frac{110\,\text{GeV}}{m_{\widetilde{B}}}\right)\left(\frac{3.91}{g_{*S}(\tau_{\widetilde{\tau}_{\rm R}})}\right)^{1/3}\left(\frac{g_*(\tau_{\widetilde{\tau}_{\rm R}})}{3.36}\right)^{1/4}.\end{aligned} \tag{3.19}$$

[¶]For a treatment of the phase space distribution beyond the sudden decay approximation, see [149].

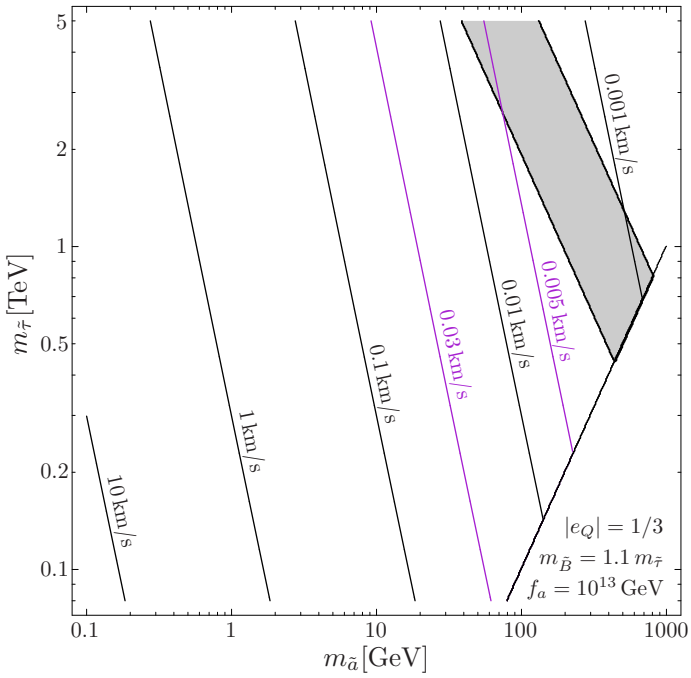

Figure 3.2: Contours of the present free–streaming velocity of axinos from stau NLSP decays, $(v^0_{\rm FS})^{\rm NTP}_{\tilde{a}}$, for $m_{\tilde{B}} = 1.1\, m_{\tilde{\tau}}$, $f_a = 10^{13}\,$GeV, $|e_Q| = 1/3$ and $y = 1$. For the case in which $\Omega_{\rm dm}$ is provided by $\Omega^{\rm NTP}_{\tilde{a}}$, the conservative limit (0.03 km/s) and the most restrictive limit (0.005 km/s) listed in Table 3.1 disfavour the regions to the left of the respective purple lines. The stau NLSP yield (3.10) satisfies $\Omega^{\rm NTP}_{\tilde{a}} = \Omega_{\rm dm}$ by construction everywhere in the shown parameter space. The grey band indicates the region with $\Omega^{\rm NTP}_{\tilde{a}} = \Omega_{\rm dm}$ for the yield (3.8) with $\kappa = 0.7$ or 1.4.

While a related estimate was given in [148], (3.19) illustrates explicitly and thus more clearly the dependence on the logarithmic factor and on e_Q.

Although axinos produced in primordial stau NLSP decays have a non–thermal distribution, $(v^0_{\rm FS})^{\rm NTP}_{\tilde{a}}$ can be confronted with the limits inferred from WDM studies such as the ones compiled in Table 3.1. This approach is motivated by the results of [137] which show that velocity limits derived with (3.11) from $m_{\rm WDM}$ limits can, to a reasonable extent, also be applied to the case with a monochromatic spectrum.

Figure 3.2 shows contours of the present free–streaming velocity of axinos from stau NLSP decays $(v^0_{\rm FS})^{\rm NTP}_{\tilde{a}}$ for $m_{\tilde{B}} = 1.1\, m_{\tilde{\tau}}$, $f_a = 10^{13}\,$GeV, $|e_Q| = 1/3$ and $y = 1$. The grey band indicates the region in which the axino density $\Omega^{\rm NTP}_{\tilde{a}}$ agrees with the present dark matter density $\Omega_{\rm dm}$ when using the thermal relic stau yield (3.8) with $\kappa = 0.7$ or 1.4, where the latter accounts for potential stau–slepton coannihilation. Scenarios within this band respect $(v^0_{\rm FS})^{\rm NTP}_{\tilde{a}} < 0.01$ km/s (corresponding to $m_{\rm WDM} > 2$ keV) and the most restrictive Lyman–α forest constraint, $(v^{\rm rms,0}_{\rm FS})^{\rm NTP}_{\tilde{a}} \lesssim 0.005$ km/s, starts to disfavour some of that region only for $m_{\tilde{\tau}} \gtrsim 3\,$TeV. For $\Omega^{\rm NTP}_{\tilde{a}} = \Omega_{\rm dm}$, as obtained with the stau NLSP yield (3.10), the regions to the left of the purple lines labelled with

0.03 km/s and 0.005 km/s are disfavoured by the respective limits (3.14) and (3.15) taken from Table 3.1.

As is evident from (3.19), the velocity contours are sensitive to e_Q and f_a. An increase in the charge of the heavy (s)quarks to $|e_Q| = 1$ reduces the velocities by one order of magnitude while an increase in f_a by an order of magnitude shifts the contours in the opposite way by the same amount. Thus, the constraints on non–thermally produced axino dark matter from the study of WDM cosmologies and effects of the associated matter power spectrum become less restrictive for higher e_Q and lower f_a values.

3.3 Constraints from Primordial Nucleosynthesis

Standard BBN has proven to be a great tool for probing the early universe, making predictions of the abundances of primordial light elements as functions of only the baryon–to–photon ratio η. From analyses of the CMB anisotropies, the value of η can be extracted and it has shown these predictions to be in good agreement with observations. However, when dealing with particle physics scenarios that are beyond the standard model, non–standard processes may spoil this success. In the scenario studied in this thesis, long–lived stau NLSPs can generate energetic particles when they decay, that could scatter off and/or dissociate the background nuclei. The charged staus can also catalyse certain processes which can lead to enhanced production of some primordial light elements. Depending on the size of these reaction rates and/or the amount of energy injected, the predictions of SBBN can change substantially. The mechanisms of these effects are explained in more detail in Secs. 1.2.3 and 1.2.4.

First, the effects of catalysed BBN are considered. At times $t > 10^3$s, the presence of negatively–charged $\widetilde{\tau}_{\rm R}^-$ sleptons can allow for catalysed primordial ^{6}Li and ^{9}Be production via the formation of $(^4{\rm He}\widetilde{\tau}_{\rm R}^-)$ and $(^8{\rm Be}\widetilde{\tau}_{\rm R}^-)$ bound states (see Sec. 1.2.3).[‖] The catalysis occurs via the processes given by (1.59) and (1.62). Observationally–inferred limits on the primordial abundances of both ^{6}Li and ^{9}Be can thus be used to extract $\tau_{\widetilde{\tau}}$–dependent upper bounds on $Y_{\widetilde{\tau}}$. In this study, those bounds are adopted directly from Fig. 5 of [89], relying on observationally–inferred limits on the following primordial fractions of ^{6}Li [91–93] and ^{9}Be [89]

$$^6{\rm Li/H}|_{\rm obs} \leq 10^{-11} - 10^{-10}, \tag{3.20}$$

$$^9{\rm Be/H}|_{\rm obs} \leq 2.1 \times 10^{-13}. \tag{3.21}$$

Confronting the $\tau_{\widetilde{\tau}}$–dependent $Y_{\widetilde{\tau}}$ bounds with (3.8), the CBBN constraints shown in Figs. 3.3 and 3.4 are obtained. In Fig. 3.3, these constraints are shown for $Y_{\widetilde{\tau}}$ given

[‖] At $t \lesssim 10^3$ s when CBBN is not efficient, injection of energy may have a noticeable effect on the ^{6}Li abundance and could even allow for a solution of the ^{7}Li problem that is consistent with ^{6}Li in the observationally inferred range (3.20) [104, 108, 150, 151].

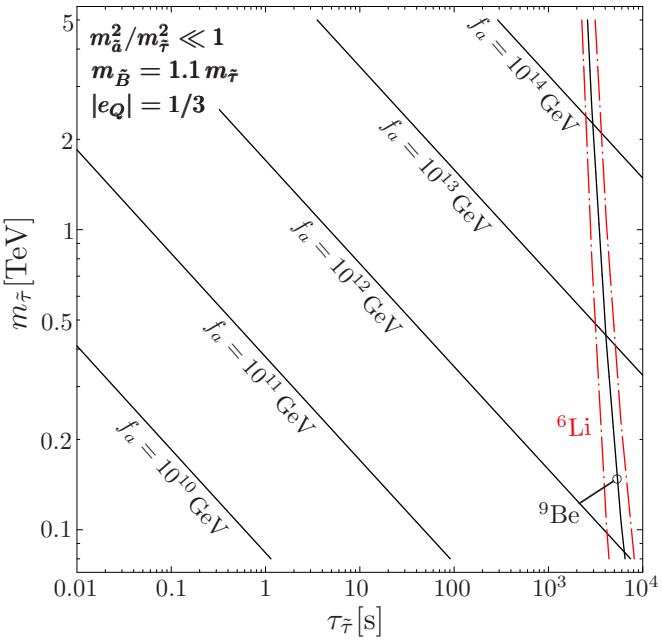

Figure 3.3: The lifetime of the $\widetilde{\tau}_{\rm R}$ NLSP, $1/\Gamma(\widetilde{\tau}_{\rm R} \to \tau \widetilde{a}) \approx \tau_{\widetilde{\tau}}$ in relation to its mass $m_{\widetilde{\tau}}$ for $m_{\widetilde{a}}^2/m_{\widetilde{\tau}}^2 \ll 1$, $m_{\widetilde{B}} = 1.1\, m_{\widetilde{\tau}}$, $|e_Q| = 1/3$, $y = 1$, and f_a values from 10^{10} to 10^{14} GeV. For a stau yield $Y_{\widetilde{\tau}}$ given by (3.8) with $\kappa = 0.7$, $\tau_{\widetilde{\tau}}$ values to the right of the nearly vertical solid and dash–dotted red lines are disfavoured by the constraints (3.21) and (3.20) on CBBN of ^{9}Be and ^{6}Li, respectively [89].

by (3.8) with $\kappa = 0.7$, $m_{\widetilde{a}}^2/m_{\widetilde{\tau}}^2 \ll 1$, $m_{\widetilde{B}} = 1.1\, m_{\widetilde{\tau}}$, $|e_Q| = 1/3$ and $y = 1$, in relation to the lifetime of the stau $\tau_{\widetilde{\tau}} \approx 1/\Gamma(\widetilde{\tau}_{\rm R} \to \tau\, \widetilde{a})$. The range (3.20) is indicated by pairs of long–dash–dotted red (^{6}Li) lines and (3.21) by solid black (^{9}Be) lines, where the regions to the right of those lines are disfavoured by an excess of ^{6}Li and ^{9}Be above the respective limits. In this way, it can clearly be seen that the observed ^{6}Li abundance implies that axino dark matter scenarios with $\tau_{\widetilde{\tau}} \gtrsim 4 \times 10^3$ s are excluded.

Figure 3.4 shows CBBN constraints for f_a values from 10^{12} up to 10^{14} GeV, considered for $Y_{\widetilde{\tau}}$ given by (3.8) with $\kappa = 0.7$, $m_{\widetilde{B}} = 1.1\, m_{\widetilde{\tau}}$, $|e_Q| = 1/3$, and $y = 1$. Again, the range (3.20) is indicated by pairs of long–dash–dotted red (^{6}Li) lines and (3.21) by solid black (^{9}Be) lines, with the regions below the lines indicating areas of ^{6}Li and ^{9}Be overproduction. For $Y_{\widetilde{\tau}}$ given by (3.8) with $\kappa = 0.7$, $\Omega_{\widetilde{a}}^{\rm NTP} h^2$ is within the nominal 3σ range (3.1) for $(m_{\widetilde{a}}, m_{\widetilde{\tau}})$ combinations indicated by the grey band. While $m_{\widetilde{\tau}}$ values above this band are disfavoured by $\Omega_{\widetilde{a}}^{\rm NTP} > \Omega_{\rm dm}$, $\Omega_{\widetilde{a}}^{\rm NTP}$ is only a minor fraction ($\lesssim 1\%$) of $\Omega_{\rm dm}$ for $m_{\widetilde{a}} \lesssim 1$ GeV and $m_{\widetilde{\tau}} \lesssim 5$ TeV, see Fig. 3.1. For $f_a \lesssim 10^{12}$ GeV and $m_{\widetilde{a}}^2/m_{\widetilde{\tau}}^2 \ll 1$, the $m_{\widetilde{\tau}}$ values disfavoured by CBBN are already excluded by the limit $m_{\widetilde{\tau}} \gtrsim 80$ GeV [27] from searches for long–lived staus at LEP. Thus, for $f_a < 10^{12}$ GeV and $m_{\widetilde{\tau}} \gtrsim 80$ GeV, CBBN constraints can only be effective if $m_{\widetilde{a}}$ and $m_{\widetilde{\tau}}$ are degenerate leading to a significant phase space suppression resulting in $\tau_{\widetilde{\tau}} > 10^3$ s. For $|e_Q| = 1$,

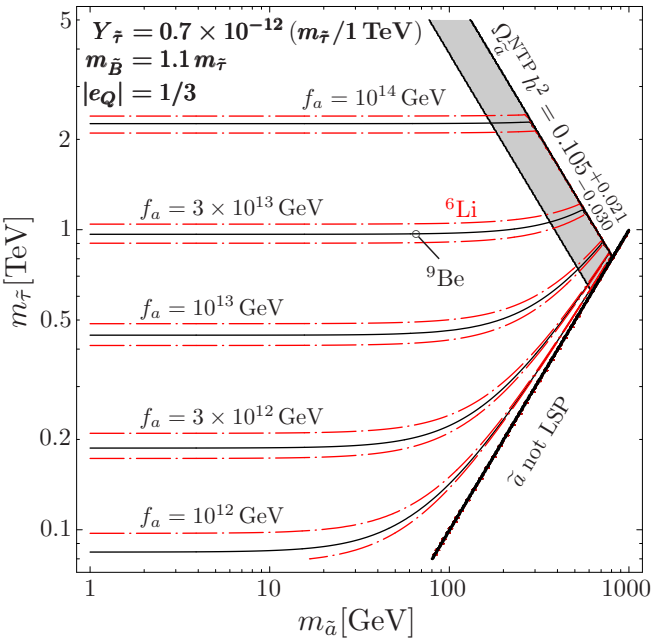

Figure 3.4: Cosmological constraints on the masses of the $\widetilde{a}$ LSP and the $\widetilde{\tau}_{\mathrm{R}}$ NLSP for $Y_{\widetilde{\tau}}$ given by (3.8) with $\kappa = 0.7$. The grey band indicates where $\Omega_{\widetilde{a}}^{\mathrm{NTP}} h^2$ lies within the region (3.1). Above this band, $\Omega_{\widetilde{a}}^{\mathrm{NTP}} h^2 > 0.126$. Because of the CBBN reactions (1.59)–(1.62) becoming efficient, the regions below the solid black and the dash–dotted red lines are disfavoured by the observationally inferred limits on primordial ^{9}Be (3.21) and ^{6}Li (3.20), respectively, for f_a as indicated, $m_{\widetilde{B}} = 1.1\,m_{\widetilde{\tau}}$, $|e_Q| = 1/3$, and $y = 1$. The shown CBBN constraints thus provide upper limits on f_a as a function of $m_{\widetilde{a}}$ and $m_{\widetilde{\tau}}$. Focusing on the $\widetilde{a}$ LSP case, the region in which $m_{\widetilde{a}} > m_{\widetilde{\tau}}$ is not considered.

the CBBN constraints agree basically with the contours shown in Fig. 3.4 but with f_a values shifted upwards by one order of magnitude.

The CBBN constraints approximately follow contours of constant $\tau_{\widetilde{\tau}}$. Indeed, for $m_{\widetilde{a}}^2/m_{\widetilde{\tau}}^2 \ll 1$, the CBBN constraints also become insensitive to $m_{\widetilde{a}}$. Moreover, for given f_a, $m_{\widetilde{a}}$, and $m_{\widetilde{\tau}}$, larger values of $\tau_{\widetilde{\tau}}$ and thereby more restrictive CBBN constraints are encountered at smaller values of $|e_Q|$, $m_{\widetilde{B}}$, or y. By decreasing $m_{\widetilde{B}}$ towards $m_{\widetilde{\tau}}$, the CBBN constraints become more restrictive because of both a larger $\tau_{\widetilde{\tau}}$ and a yield $Y_{\widetilde{\tau}}$ that is enhanced by stau–bino coannihilation. However, the effect is dominated by the change in $\tau_{\widetilde{\tau}}$ due to the relatively mild impact of $Y_{\widetilde{\tau}}$ on the CBBN processes in the relevant region, see Fig. 5 of [89].

It must be stressed that each set of CBBN constraints in Fig. 3.4 – such as the ^{9}Be contours – imposes an upper limit on the PQ scale f_a as a function of $m_{\widetilde{a}}$ and $m_{\widetilde{\tau}}$. Since those f_a limits become only more restrictive for $m_{\widetilde{a}} \to m_{\widetilde{\tau}}$, their $m_{\widetilde{a}}$–independent values at $m_{\widetilde{a}}^2/m_{\widetilde{\tau}}^2 \ll 1$ are conservative limits. In the considered $\widetilde{a}$ LSP case, those are relevant for studies and searches of axions even without further knowledge of $m_{\widetilde{a}}$. This

conservative limit is further explored in Secs. 3.4 and 3.5.

Next the effects of late hadronic energy injection on the BBN constraints, which start becoming important at $\tau_{\widetilde{\tau}} \gtrsim 100\,\mathrm{s}$, must be considered. As the mesons produced from the τ leptons emitted in the 2–body decay $\widetilde{\tau}_{\mathrm{R}} \to \tau\widetilde{a}$ typically decay too quickly to interact hadronically, the main contribution to the injection of hadronic energy comes from the 4–body decay $\widetilde{\tau}_{\mathrm{R}} \to \tau\widetilde{a}q\bar{q}$ with the average amount of energy released per decay characterised by

$$\epsilon_{\mathrm{had}} \equiv \frac{1}{\Gamma_{\mathrm{tot}}^{\widetilde{\tau}_{\mathrm{R}}}} \int_{m_{q\bar{q}}}^{m_{\widetilde{\tau}}-m_{\widetilde{a}}-m_{\tau}} \mathrm{d}m_{q\bar{q}}\, m_{q\bar{q}} \frac{\mathrm{d}\Gamma(\widetilde{\tau}_{\mathrm{R}} \to \tau\widetilde{a}q\bar{q})}{\mathrm{d}m_{q\bar{q}}}. \tag{3.22}$$

The mesons from this process also decay before they can interact with the background nuclei. Therefore a cut must be placed on the invariant mass of the produced $q\bar{q}$ pairs, $m_{q\bar{q}} > m_{q\bar{q}}^{\mathrm{cut}} = 2\,\mathrm{GeV}$, so as to consider only those that hadronise into nucleons. This was already discussed in Sec. 2.3. Note that a more precise calculation of the constraints would require, in addition to $\mathrm{d}\Gamma(\widetilde{\tau}_{\mathrm{R}} \to \tau\widetilde{a}q\bar{q})/\mathrm{d}m_{q\bar{q}}$, a treatment of the fragmentation of the quarks into hadrons and of the propagation of the resulting hadron spectra when computing the abundances of primordial light elements, see [99, 109, 151, 152].

Figure 3.5 shows the hadronic energy release as calculated with (3.22) (solid lines) along with the lifetime contours of the stau (dotted lines). The dependency of ϵ_{had} on $m_{\widetilde{a}}$ is as weak as that of $\tau_{\widetilde{\tau}}$, until $m_{\widetilde{a}}$ is large enough. As f_a increases, the average hadronic energy release decreases, although not as drastically as the increase in the lifetime. This is due to $\Gamma_{\mathrm{tot}} \propto 1/f_a^2$ while the normalisation of ϵ_{had} to Γ_{tot} means that at most, $\epsilon_{\mathrm{had}} \propto 1/\log^2\left(\frac{y^2 f_a^2}{2m_{\widetilde{\tau}}^2}\right)$. The parameter that produces the stronger effect is the $m_{\widetilde{B}}/m_{\widetilde{\tau}}$ ratio, which when reduced to ~ 1, results in a much faster increase in ϵ_{had} with increasing $m_{\widetilde{\tau}}$. This is due to $\Gamma(\widetilde{\tau}_{\mathrm{R}} \to \tau\widetilde{a}q\bar{q}) \propto m_{\widetilde{\tau}}^2$ while the dominant, logarithmically–enhanced part of $\Gamma(\widetilde{\tau}_{\mathrm{R}} \to \tau\widetilde{a}) \propto m_{\widetilde{\tau}}\, m_{\widetilde{B}}^2$ only.

The observationally–inferred primordial abundance of D

$$\mathrm{D/H}|_{\mathrm{mean}} = (2.78^{+0.44}_{-0.38}) \times 10^{-5} \quad \text{(severe)}, \tag{3.23}$$

$$\mathrm{D/H}|_{\mathrm{high}} = (3.98^{+0.59}_{-0.67}) \times 10^{-5} \quad \text{(conservative)}, \tag{3.24}$$

can be used to derive $\tau_{\widetilde{\tau}}$–dependent upper limits (95%) on the quantity $\xi_{\mathrm{had}} \equiv \epsilon_{\mathrm{had}} Y_{\widetilde{\tau}\,\mathrm{had}}$ [99]. Then, using ϵ_{had} as calculated in (3.22), this gives the upper limits on the yield of the staus before they decay

$$Y_{\widetilde{\tau}\,\mathrm{had}}^{\mathrm{max}} = \xi_{\mathrm{had}}^{\mathrm{max}}/\epsilon_{\mathrm{had}}\ . \tag{3.25}$$

Figures 3.6 and 3.7 show these upper limits as functions of $m_{\widetilde{\tau}}$ and $m_{\widetilde{a}}$ as obtained from the severe (3.23) and conservative (3.24) limits, respectively. The darker shadings represent the stronger constraints with the contours shown ranging from 10^{-9}, to 2×10^{-13} for the smallest $Y_{\widetilde{\tau}\,\mathrm{had}}^{\mathrm{max}}$ (lower right panel in Fig. 3.6). The progression of the panels

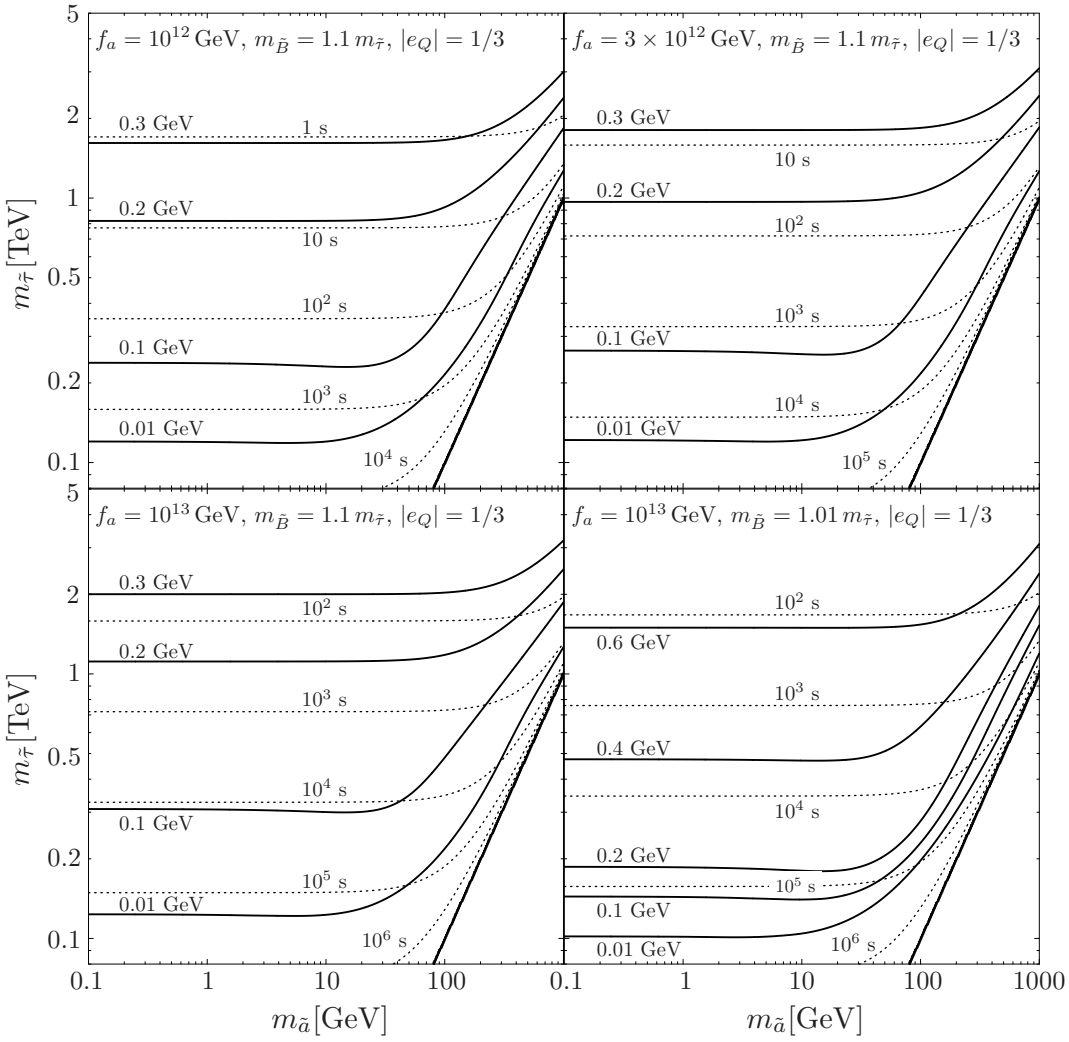

Figure 3.5: Hadronic energy release $\epsilon_{\rm had}$ from the 4–body decay $\widetilde{\tau}_R \to \tau\widetilde{a}q\bar{q}$ (solid lines) and lifetime contours of $\widetilde{\tau}_R$ (dashed lines). Starting from the top left panel and going row by row, the parameters are $f_a = 10^{12}\,\mathrm{GeV}$, $m_{\widetilde{B}} = 1.1\,m_{\widetilde{\tau}}$; $f_a = 3\times10^{12}\,\mathrm{GeV}$, $m_{\widetilde{B}} = 1.1\,m_{\widetilde{\tau}}$; $f_a = 10^{13}\,\mathrm{GeV}$, $m_{\widetilde{B}} = 1.1\,m_{\widetilde{\tau}}$; and $f_a = 10^{13}\,\mathrm{GeV}$, $m_{\widetilde{B}} = 1.01\,m_{\widetilde{\tau}}$. In all the panels, $|e_Q| = 1/3$ and $y = 1$.

(left to right, and top to bottom) follows combinations of parameters where increasingly tighter constraints are imposed by the hadronic energy injection. Varying $m_{\widetilde{B}}/m_{\widetilde{\tau}}$ to an almost degenerate ratio of 1.01 results in the tightest limits on the yield $Y^{\rm max}_{\widetilde{\tau}\,\rm had}$ shown.

Now by confronting the maximum yield with that of the thermal relic of the staus $Y_{\widetilde{\tau}}$ (3.8), limits in the $m_{\widetilde{\tau}}$ and $m_{\widetilde{a}}$ plane can be placed, as illustrated in Fig. 3.8. The regions enclosed by the blue short–dash–dotted lines are excluded by the conservative/severe hadronic D constraints, as labelled. The region with $\Omega^{\rm NTP}_{\widetilde{a}} \in \Omega^{3\sigma}_{\rm dm}$ is indicated by the grey band, where the region above that band is the one excluded by (3.9). The dotted

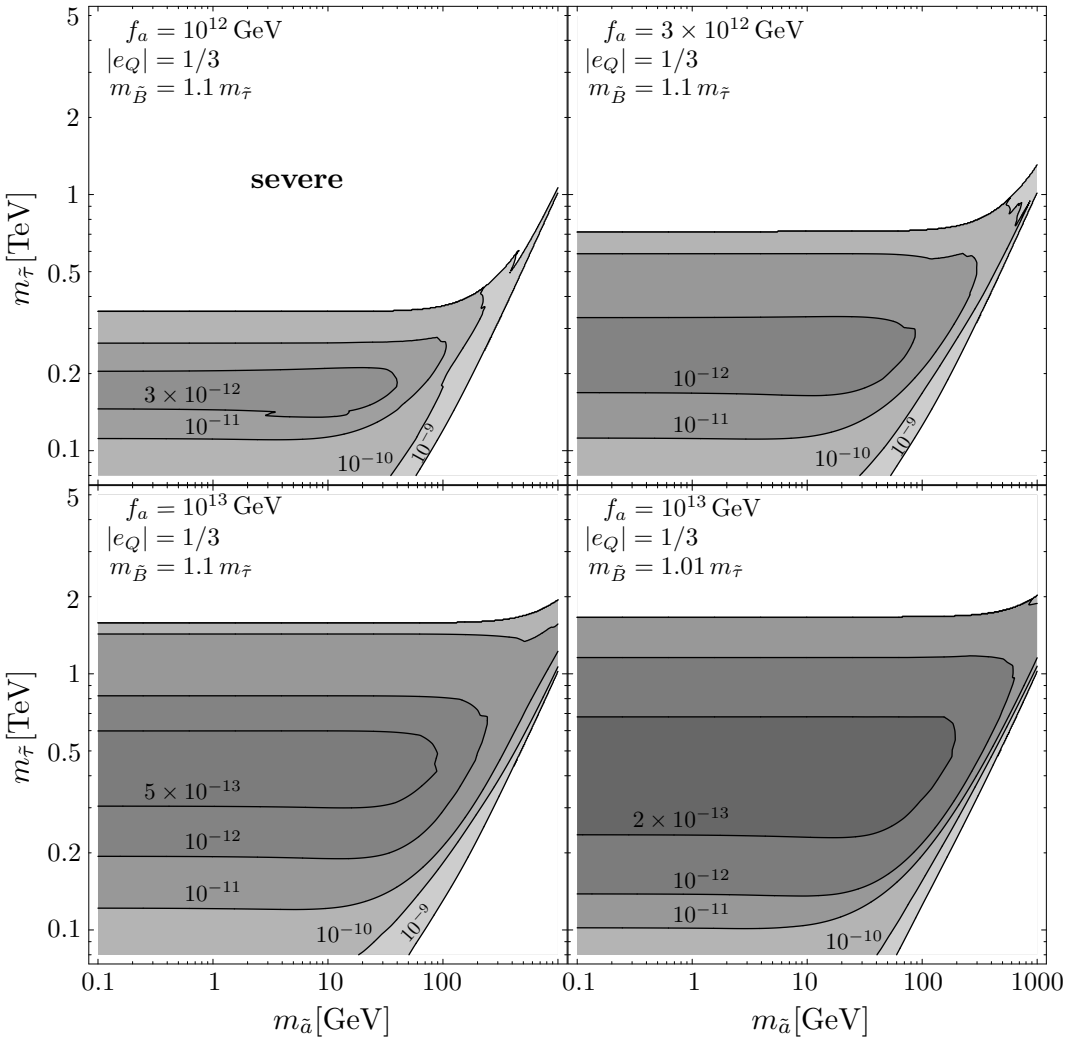

Figure 3.6: Upper limits on the yield of $\widetilde{\tau}$ before their decay, obtained with the severe limits on late hadronic energy injection (3.23). The contour shading darkens with stronger limits. Again, starting from the top left panel and going row by row, the parameters $f_a = 10^{12}\,\mathrm{GeV}$, $m_{\widetilde{B}} = 1.1\,m_{\widetilde{\tau}}$; $f_a = 3 \times 10^{12}\,\mathrm{GeV}$, $m_{\widetilde{B}} = 1.1\,m_{\widetilde{\tau}}$; $f_a = 10^{13}\,\mathrm{GeV}$, $m_{\widetilde{B}} = 1.1\,m_{\widetilde{\tau}}$; and $f_a = 10^{13}\,\mathrm{GeV}$, $m_{\widetilde{B}} = 1.01\,m_{\widetilde{\tau}}$. In all panels, $|e_Q| = 1/3$ and $y = 1$.

lines are contours of $\tau_{\widetilde{\tau}} = 10^2$, 5×10^3, and $10^5\,\mathrm{s}$.

Again, the parameters are chosen such that the constraints shown in the panels become progressively more limiting. For the generic case of $m_{\widetilde{B}} = 1.1\,m_{\widetilde{\tau}}$ and a yield characterised by $\kappa = 0.7$, both the severe and conservative hadronic BBN limits vanish for $f_a = 10^{13}\,\mathrm{GeV}$. For a larger stau relic yield given by $\kappa = 1.4$, accounting for possible stau–slepton coannihilation, more severe constraints are obtained, excluding stau masses between 300 and 900 GeV for $m_{\widetilde{a}} \lesssim 200\,\mathrm{GeV}$. Decreasing $m_{\widetilde{B}}$ has the same

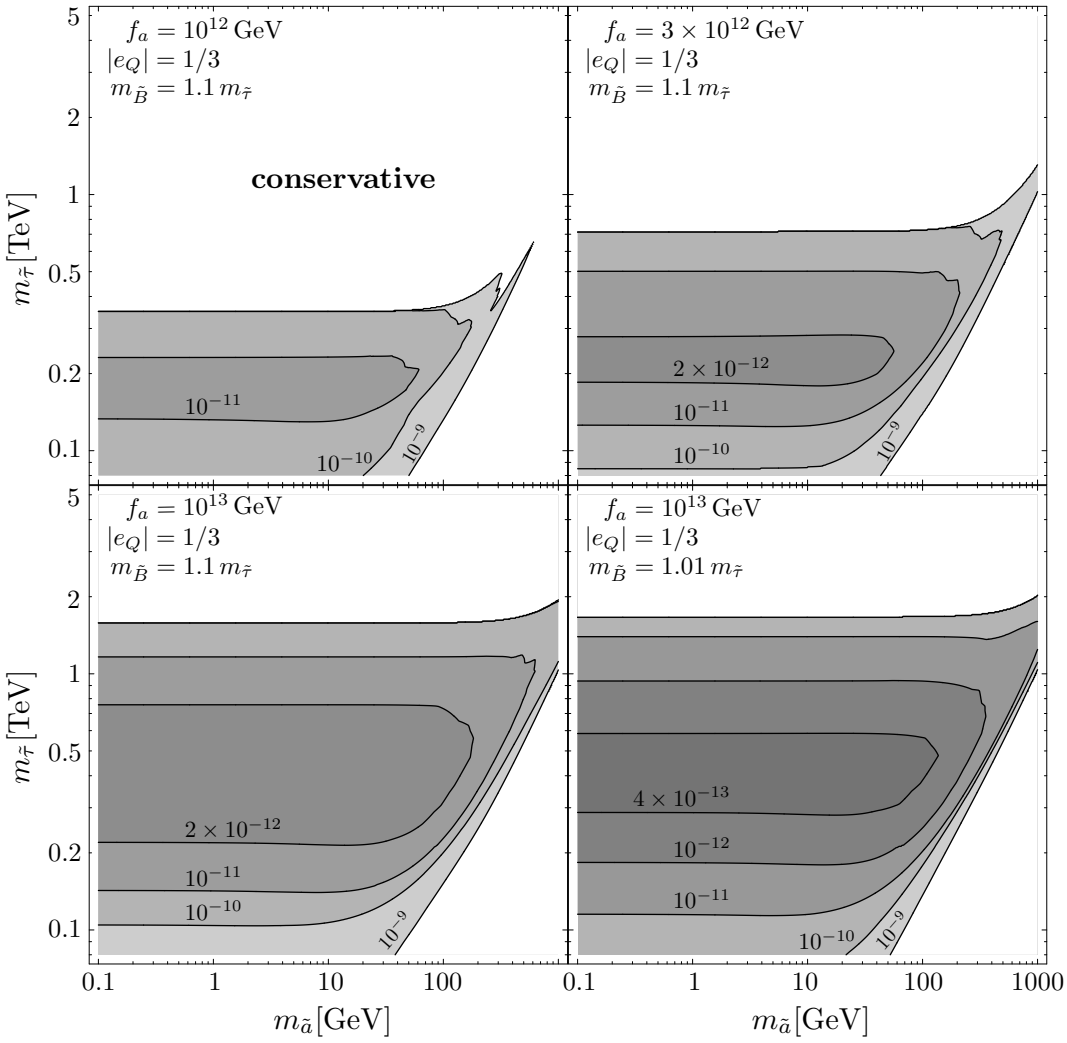

Figure 3.7: The same as Fig. 3.6 but using the conservative limits on late hadronic energy injection (3.24).

effect in excluding larger regions of parameter space, due to the increase in ϵ_{had}, as illustrated in Fig. 3.5. Here (lower left panel of Fig. 3.8), the conservative constraints appear for the first time. Taking the extreme case of having simultaneous bino–stau–slepton coannihilation and therefore $\kappa = 2.0$ results in the most restrictive case shown in the figure (lower right panel). There the severe D limit disfavours almost the entire parameter space for lifetimes $10^2\,\mathrm{s} \lesssim \tau_{\tilde{\tau}} \lesssim 10^5\,\mathrm{s}$.

Also shown in Fig. 3.8 are the CBBN constraints associated with (3.20) (long-dash-dotted red lines) and (3.21) (solid black lines), where the regions below the lines are excluded due to overproduction of the respective nuclei. Where the hadronic BBN constraints are present, they provide additional constraints to the corresponding ones

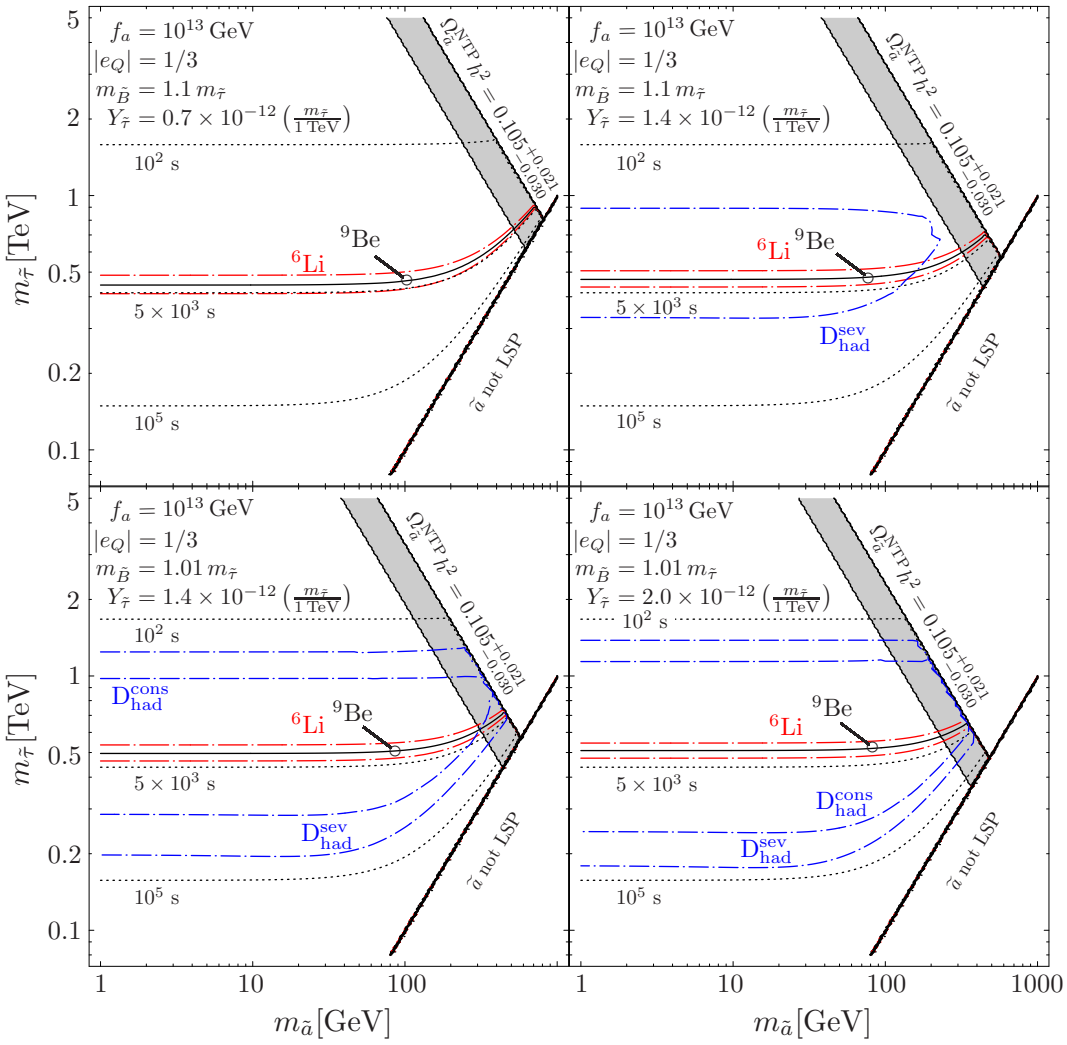

Figure 3.8: Cosmological constraints on the masses of the axino LSP and stau NLSP for $f_a = 10^{13}$ GeV and $Y_{\tilde{\tau}}$ given by (3.8). Starting from the top left panel and going row by row, the parameters are $m_{\tilde{B}} = 1.1\, m_{\tilde{\tau}}$, $\kappa = 0.7$; $m_{\tilde{B}} = 1.1\, m_{\tilde{\tau}}$, $\kappa = 1.4$; $m_{\tilde{B}} = 1.01\, m_{\tilde{\tau}}$, $\kappa = 1.4$; and $m_{\tilde{B}} = 1.01\, m_{\tilde{\tau}}$, $\kappa = 2.0$. In all panels, $|e_Q| = 1/3$ and $y = 1$. The CBBN constraints from ^{6}Li and ^{9}Be abundances exclude the regions below the long–dash–dotted red and the solid black lines. Hadronic BBN constraints from D exclude the regions enclosed by the respective short–dash–dotted blue lines. Contours of $\tau_{\tilde{\tau}} = 10^2, 5 \times 10^3$ and 10^5 s are shown by the dotted lines. On (above) the grey band, $\Omega_{\tilde{a}}^{\mathrm{NTP}} \in \Omega^{3\sigma}_{\mathrm{dm}}$ ($\Omega_{\tilde{a}}^{\mathrm{NTP}} h^2 > 0.126$).

from CBBN. However, the hadronic BBN constraints are not always there. In this case the CBBN constraints would give the exclusion limits on $m_{\tilde{\tau}}$ and $m_{\tilde{a}}$. The next section shows this more explicitly and also shows that the limits from CBBN remain until $f_a \lesssim 10^{12}$ GeV for $m_{\tilde{\tau}} \gtrsim 80$ GeV.

For $\tau_{\tilde{\tau}} \gtrsim 10^4$ s, the injection of energy from electromagnetic decays of the staus must

be taken into account. The derivation of the electromagnetic BBN constraints proceeds as outlined for the hadronic constraints but relies on a conservative estimate of $\epsilon_{\rm em}$. The electromagnetic energy release is governed by the tau emitted in the 2–body decay with an energy

$$E_\tau = \frac{m_{\widetilde{\tau}}^2 - m_{\widetilde{a}}^2 + m_\tau^2}{2m_{\widetilde{\tau}}}, \tag{3.26}$$

in the rest frame of the $\widetilde{\tau}_{\rm R}$. As each τ decays into at least one ν, which does not interact electromagnetically, only a fraction of E_τ contributes to the total electromagnetic energy injection [139, 153]. The conservative estimate

$$\epsilon_{\rm em} = 0.3\, E_\tau = 0.3\, \frac{m_{\widetilde{\tau}}^2 - m_{\widetilde{a}}^2 + m_\tau^2}{2m_{\widetilde{\tau}}}\ , \tag{3.27}$$

is used to avoid that the electromagnetic BBN constraints presented are overly restrictive.

Upper limits on

$$\xi_{\rm em} \equiv \epsilon_{\rm em}\, Y_{\widetilde{\tau}}, \tag{3.28}$$

are then relied on to derive constraints on $Y_{\widetilde{\tau}}$. Accordingly, the $\mathrm{D}_{\rm em}^{\rm sev}$ and ^{3}He/D constraints from the respective limits given in Fig. 42 of [99] and the $\mathrm{D}_{\rm em}^{\rm cons}$ constraint from the respective limit given in Fig. 6 of [91] are obtained. However, these limits are typically much weaker than the ones from bound–state formation of long–lived stau NLSPs and are absent altogether from the scenarios depicted in Fig. 3.8.

Figure 3.9 shows the mass bounds for the non–standard production scenario where $\Omega_{\widetilde{a}}^{\rm NTP} = \Omega_{\rm dm}$ is satisfied everywhere in the shown parameter space by the stau yield (3.10). As in Fig. 3.8, the long–dash–dotted red and the solid black lines disfavour the regions below the lines due to overabundances of ^{6}Li and ^{9}Be, respectively. Conservative and severe hadronic BBN constraints from D exclude the regions enclosed by the respective short–dash–dotted blue lines, as labelled. Contours of $\tau_{\widetilde{\tau}} = 10^2, 5\times10^3$ and 10^5 s are shown by the dotted lines. Additionally, the constraints from electromagnetic energy injection associated with D given in (3.23) and (3.24) are shown by the dashed blue lines, excluding all regions enclosed by them while those associated with ^{3}He/D [99] disfavour the regions enclosed by the double–dash–dotted green lines. It can be explicitly seen in this figure that these constraints only show up in the regions well within those already excluded by the CBBN constraints and are absent altogether for $f_a < 3\times10^{12}\,$GeV.

Note that the grey band in this case indicates where the stau yield (3.10), required for the axinos to make up the entire dark matter density, coincides with that of the stau thermal relic yield (3.8). In each panel, a range spanning over two possible values of κ is used in (3.8) in order to take into account any possible coannihilating processes. The

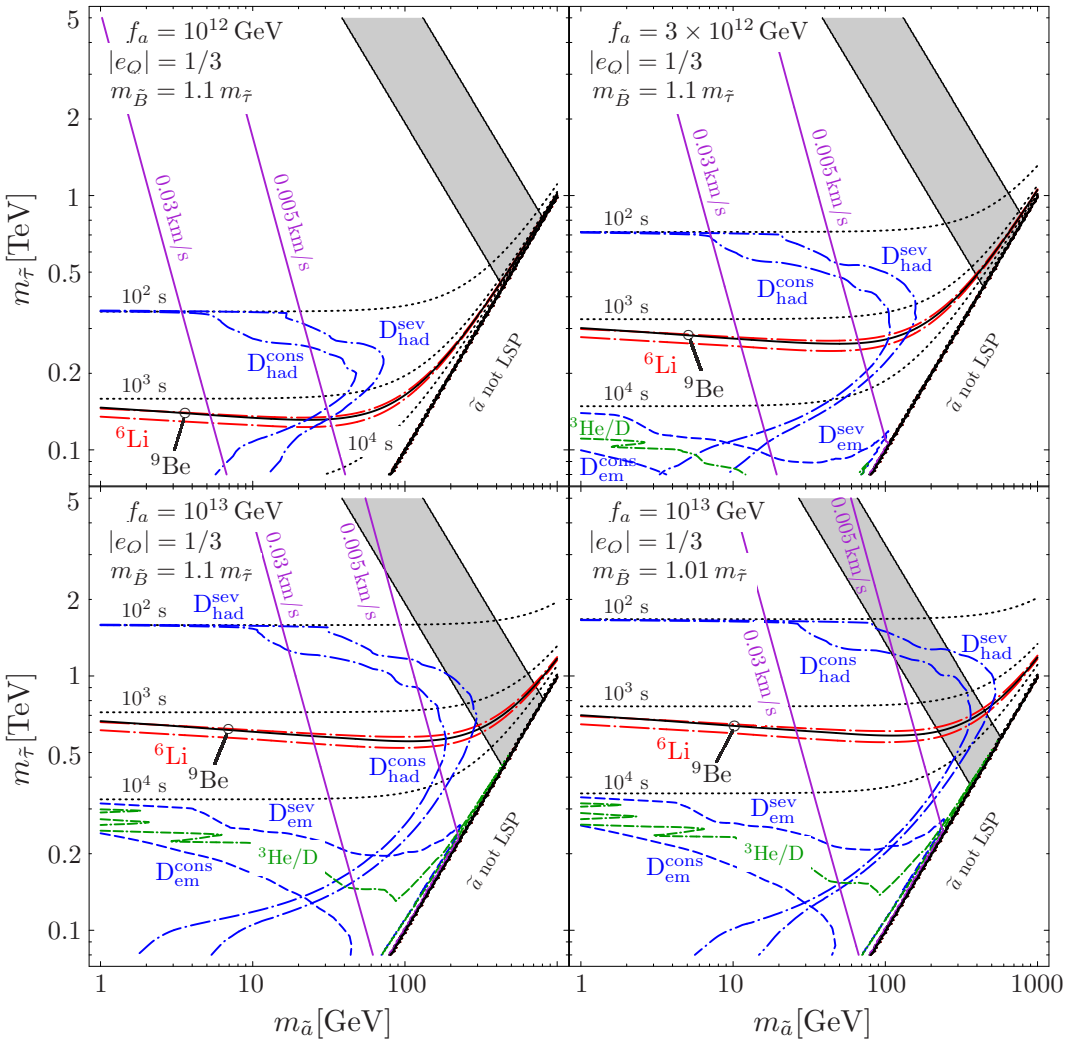

Figure 3.9: Cosmological constraints on the masses of the axino LSP and stau NLSP in the non–standard production scenario. Starting from the top left panel and going row by row, the parameters are $f_a = 10^{12}\,\text{GeV}$, $m_{\widetilde{B}} = 1.1\, m_{\tilde{\tau}}$; $f_a = 3 \times 10^{12}\,\text{GeV}$, $m_{\widetilde{B}} = 1.1\, m_{\tilde{\tau}}$; $f_a = 10^{13}\,\text{GeV}$, $m_{\widetilde{B}} = 1.1\, m_{\tilde{\tau}}$; and $f_a = 10^{12}\,\text{GeV}$, $m_{\widetilde{B}} = 1.01\, m_{\tilde{\tau}}$. In all panels, $|e_Q| = 1/3$ and $y = 1$. The CBBN constraints from ^{6}Li and ^{9}Be abundances exclude the regions below the long–dash–dotted red and the solid black lines. Hadronic (electromagnetic) BBN constraints from D exclude the regions enclosed by the respective short–dash–dotted blue (dashed blue) lines. Electromagnetic BBN constraints from ^{3}He/D exclude regions enclosed by the double–dash–dotted green lines. The constraints from free–streaming velocity disfavour the regions to the left of the purple lines, denoting the conservative limit $(v^0_{\rm FS})^{\rm NTP}_{\tilde{a}} \lesssim 0.03\,\text{km/s}$ and the most restrictive limit $(v^0_{\rm FS})^{\rm NTP}_{\tilde{a}} \lesssim 0.005\,\text{km/s}$. Contours of $\tau_{\tilde{\tau}} = 10^2, 5 \times 10^3$ and 10^5 s are shown by the dotted lines. The stau NLSP yield (3.10) satisfies $\Omega^{\rm NTP}_{\tilde{a}} = \Omega_{\rm dm}$ by construction everywhere in the shown parameter space. On (above) the grey band, $\Omega^{\rm NTP}_{\tilde{a}} \in \Omega^{3\sigma}_{\rm dm}$ ($\Omega^{\rm NTP}_{\tilde{a}} h^2 > 0.126$) for the yield given by (3.8), using the appropriate values for κ.

first three panels use the values $\kappa = 0.7$ (for no coannihilation) and also $\kappa = 1.4$ (for a possible stau–slepton coannihilation) while the last panel (lower right) uses $\kappa = 1.4$ (for stau–bino coannihilation) and $\kappa = 2.0$ (to also take into account possible simultaneous stau–bino–slepton coannihilation).

Clearly, there are more severe constraints below the grey bands in this case compared to the constraints in Fig. 3.8, with both the severe and the conservative hadronic BBN constraints already showing up at $f_a = 10^{12}\,\mathrm{GeV}$ and excluding far larger areas of parameter space in the panels for $f_a = 10^{13}\,\mathrm{GeV}$. This is due to the rather large yields that must be assumed for small $m_{\widetilde{a}}$ in this region to fulfil $\Omega_{\mathrm{dm}} = \Omega_{\widetilde{a}}^{\mathrm{NTP}}$. It is interesting to note the rather different behaviour of both the CBBN and hadronic BBN constraints as compared to scenarios relying on the thermal relic values of $Y_{\widetilde{\tau}}$ given in (3.8). There is a greater dependency on the axino mass in the non–standard production scenario, leading to CBBN constraints that deviate from the approximate $\tau_{\widetilde{\tau}} = 5 \times 10^3\,\mathrm{s}$ constraint derived in the other case. This can be seen to come about from the extra $m_{\widetilde{a}}$ dependency that enters in (3.9).

Also indicated in the figure are the conservative and most restrictive free–streaming velocity limits discussed in Sec. 3.2 and given by (3.14) and (3.15), respectively. The regions to the left of the respective limits, shown by the purple lines, are disfavoured due to too much suppression of small–scale structure. For $\tau_{\widetilde{\tau}} > 100\,\mathrm{s}$, only the most restrictive constraint, which places a limit of $(v_{\mathrm{FS}}^{0})_{\widetilde{a}}^{\mathrm{NTP}} \lesssim 0.005\,\mathrm{km/s}$, adds to those from CBBN and hadronic BBN to further tighten the constraints on the parameter space. For $\tau_{\widetilde{\tau}} < 100\,\mathrm{s}$, both the conservative and restrictive constraints significantly reduce the parameter space.

Let us comment on the potential interplay between late energy injection and CBBN. The CBBN limits adopted from [89] have been derived for an abundance of D obtained with standard BBN. For an increased D abundance from hadrodissociation of ^{4}He, CBBN of ^{6}Li and ^{9}Be becomes more efficient. This is evident for ^{6}Li since its catalysis proceeds via $(^4\mathrm{He}\,\widetilde{\tau}_{\mathrm{R}}^{-}) + \mathrm{D} \rightarrow {}^6\mathrm{Li} + \widetilde{\tau}_{\mathrm{R}}^{-}$ [87] and since the primordial abundance of D stays significantly below the one of ^{4}He at the relevant times (even for a maximum of observationally tolerable hadrodissociation of ^{4}He), see Fig. 2.4 in [154]. An increased output of ^{9}Be results from the final step of its catalysis, $(^8\mathrm{Be}\,\widetilde{\tau}_{\mathrm{R}}^{-}) + n \rightarrow {}^9\mathrm{Be} + \widetilde{\tau}_{\mathrm{R}}^{-}$ [88,89], which becomes more efficient since an enhanced abundance of D increases the number of neutrons n at the relevant times [81], see Fig. 4 in [89]. Moreover, the debris of hadrodissociated ^{4}He can hit ambient ^{4}He and thereby fuse additional ^{6}Li [99,104,105]. The interplay of late energy injection and CBBN will thus lead to constraints that can only be stronger than the ones presented in this thesis. Aiming at conservative limits allows those intricacies to be neglected, but they will have to be faced in future refinements of the presented constraints.

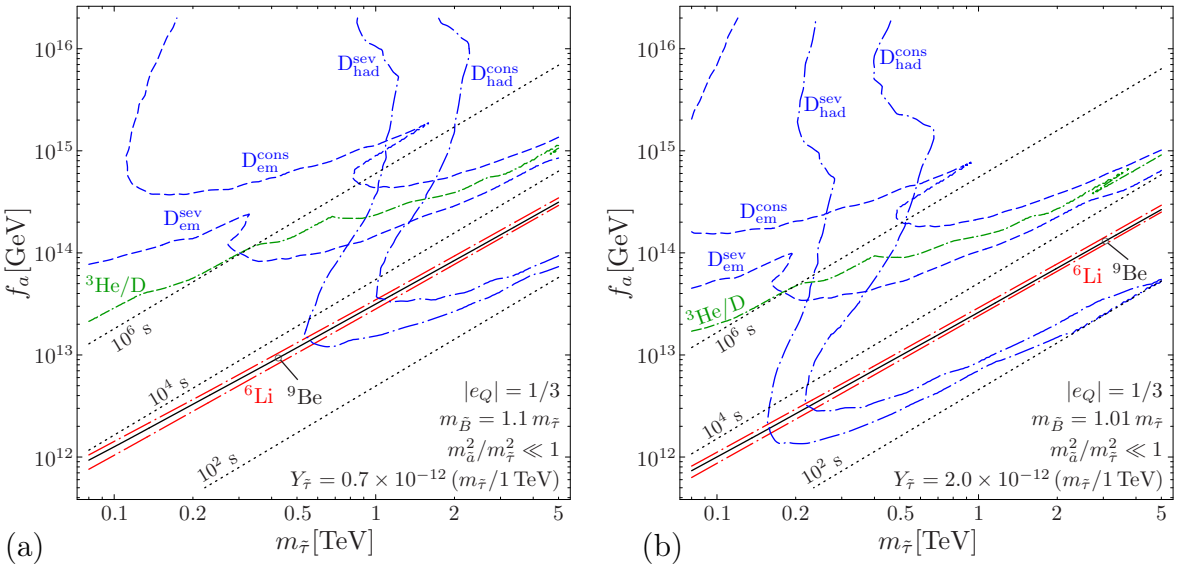

Figure 3.10: BBN constraints on the PQ scale f_a, shown for (a) $m_{\widetilde{B}} = 1.1\, m_{\widetilde{\tau}}$, $Y_{\widetilde{\tau}}$ given by (3.8)) with $\kappa = 0.7$ and (b) $m_{\widetilde{B}} = 1.01\, m_{\widetilde{\tau}}$, $Y_{\widetilde{\tau}}$ given by (3.8) with $\kappa = 2.0$. In both panels, $m_{\widetilde{a}}^2/m_{\widetilde{\tau}}^2 \ll 1$, $|e_Q| = 1/3$, and $y = 1$. The hadronic BBN constraints associated with (3.23) and (3.24) disfavour the regions in the upper right–hand corner enclosed by the respective short–dash–dotted blue lines. Electromagnetic BBN constraints associated with D disfavour the upper regions enclosed by the respective dashed blue lines and the ones associated with ^{3}He/D the region above the double–dash–dotted green line. The regions above the long–dash–dotted red and the solid black lines are disfavoured by the CBBN constraints associated with (3.20) and (3.21). Contours of $\tau_{\widetilde{\tau}} = 10^2$, 10^4, and 10^6 s are shown by the dotted lines.

3.4 BBN Constraints on the PQ Scale

The above CBBN constraints and BBN constraints associated with hadronic and electromagnetic energy release are combined to derive upper limits on the PQ scale f_a as functions of the stau mass $m_{\widetilde{\tau}}$. In agreement with the results of the previous section, it is found that the hadronic BBN limits can be substantially more restrictive than those imposed by the CBBN constraints.

Figure 3.10 presents the f_a limits for $m_{\widetilde{a}}^2/m_{\widetilde{\tau}}^2 \ll 1$, $|e_Q| = 1/3$, and $y = 1$. Panel (a) shows the generic case of $m_{\widetilde{B}} = 1.1\, m_{\widetilde{\tau}}$ and $Y_{\widetilde{\tau}}$ given by (3.8) with $\kappa = 0.7$ while panel (b) shows the case with $m_{\widetilde{B}} = 1.01\, m_{\widetilde{\tau}}$ and $\kappa = 2.0$ where there occurs simultaneous stau–slepton–bino coannihilation. Contours of $\tau_{\widetilde{\tau}} = 10^2$, 10^4, and 10^6 s are shown by the dotted lines. Above the long–dash–dotted red and the black solid lines, CBBN of ^{6}Li and ^{9}Be are in excess of the respective limits (3.20) and (3.21). The hadronic BBN constraints associated with (3.23) and (3.24) disfavour the regions in the upper right–hand corner enclosed by the respective short–dash–dotted blue lines. Note that those constraints are only provided for $\tau_{\widetilde{\tau}} \geq 100$ s since the typically milder limits associated with proton–neutron interconversion processes [100], which become relevant for smaller

$\tau_{\widetilde{\tau}}$ [99, 105, 109], are not considered. Nevertheless, the hadronic BBN constraints place limits on the PQ scale f_a that become clearly more restrictive than the CBBN–induced limits towards large $m_{\widetilde{\tau}}$ and/or large $Y_{\widetilde{\tau}}$. In fact, the hadronic BBN constraint on f_a can already be dominant in the mass range that is promising for a discovery of a long–lived stau at the LHC, $m_{\widetilde{\tau}} < 1$ TeV.

The electromagnetic BBN constraints imposed by primordial D, whose primordial abundance is given in (3.23) and (3.24), are shown by the dashed blue lines. The constraints associated with ^{3}He/D [99] are indicated by the double-dash-dotted green lines, where the regions above these lines are excluded. The figure shows that the electromagnetic BBN constraints appear only for $\tau_{\widetilde{\tau}} > 10^4$ s thereby excluding regions already disfavoured by CBBN. Nevertheless, they support the finding that values of the PQ scale at the scale of grand unification, $f_a \sim 10^{16}$ GeV, will be in conflict with successful BBN in the considered scenarios once a long–lived charged slepton is observed at the LHC.

Let us briefly discuss the robustness of the shown f_a limits and address important sensitivities. By considering $m_{\widetilde{a}}^2/m_{\widetilde{\tau}}^2 \ll 1$, the CBBN–imposed f_a limits are conservative limits. Those constraints become more restrictive for $m_{\widetilde{a}} \to m_{\widetilde{\tau}}$. This is different for constraints associated with late energy injection, where any bound can be evaded for a finely tuned $m_{\widetilde{a}}$–$m_{\widetilde{\tau}}$ degeneracy leading to $\epsilon_{\mathrm{had/em}} \to 0$. The f_a limits are sensitive to $Y_{\widetilde{\tau}}$ and in settings with a sizeable left–right stau mixing, an exceptionally small $Y_{\widetilde{\tau}}$ is possible such that even the CBBN constraints may be respected [155, 156]. The f_a limits depend on the quantum numbers of the heavy KSVZ fields. While $\epsilon_{\mathrm{had/em}}$ are independent of e_Q, $\tau_{\widetilde{\tau}} \propto 1/e_Q^4$. The f_a limits can thus be relaxed, e.g. by one order of magnitude for $|e_Q| = 1$. The CBBN and hadronic BBN constraints in the case of the $\widetilde{\mathrm{e}}_R$ or $\widetilde{\mu}_R$ NLSP are identical to the ones shown. The electromagnetic BBN constraints however will be more restrictive in the $\widetilde{\mathrm{e}}_R$ NLSP case since all of the electron energy E_e released in the $\widetilde{\mathrm{e}}_R$ NLSP decay will contribute, i.e. $\epsilon_{\mathrm{em}} = E_e$.

3.5 Limits on the Reheating Temperature

In this section the limits that can be derived on the reheating temperature T_{R} are studied. In Sec. 3.1, it was shown in (3.5) that the relic density of thermally produced axinos $\Omega_{\widetilde{a}}^{\mathrm{TP}}$ is sensitive to the post–inflationary reheating temperature T_{R} and the Peccei–Quinn scale f_a, providing a way through which these two parameters can be probed.

As a first step, an upper limit on $\Omega_{\widetilde{a}}^{\mathrm{TP}}$ can be placed by requiring $\Omega_{\widetilde{a}}^{\mathrm{TP}} \leq \Omega_{\mathrm{dm}}$. This places upper limits on T_{R} [118, 125, 126, 130, 131]. These T_{R} limits – which depend on the axino mass $m_{\widetilde{a}}$ and on the PQ scale f_a – can be very restrictive for models of inflation and of baryogenesis. For example, $T_{\mathrm{R}} \lesssim 10^6$ GeV is found for $f_a = 10^{11}$ GeV and $m_{\widetilde{a}} = 100$ keV [125]. The scenario $\Omega_{\widetilde{a}}^{\mathrm{NTP}} + \Omega_a \ll \Omega_{\mathrm{dm}}$ is considered in this section,

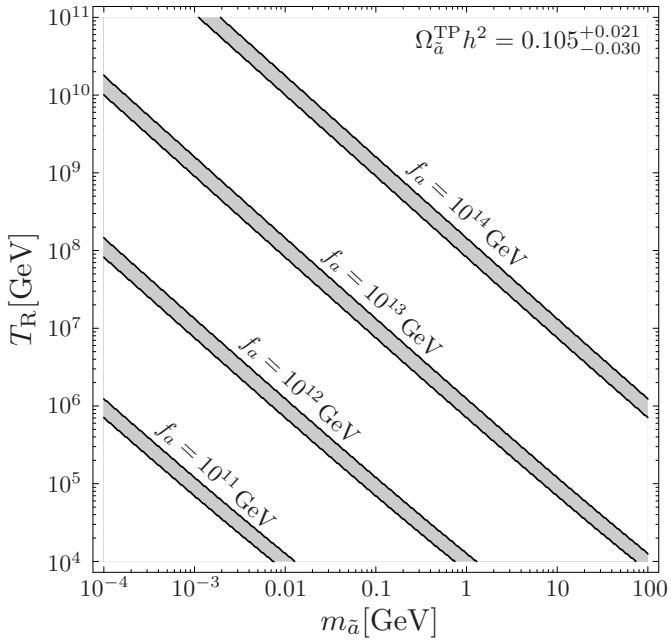

Figure 3.11: Upper limits on the reheating temperature $T_{\rm R}$ as a function of the axino mass $m_{\tilde{a}}$ in scenarios with axino cold dark matter for $f_a = 10^{11}$, 10^{12}, 10^{13}, and 10^{14} GeV (as labelled). For $(m_{\tilde{a}}, T_{\rm R})$ combinations within the grey bands, the thermally produced axino density $\Omega_{\tilde{a}}^{\rm TP}h^2$ is within the nominal 3σ range (3.1). For given f_a, the region above the associated band is disfavoured by $\Omega_{\tilde{a}}^{\rm TP}h^2 > 0.126$.

with (3.5) constrained by (3.2). For $m_{\tilde{a}} \lesssim 1$ GeV, the $T_{\rm R}$ limits shown in Fig. 3.11 will shift only marginally by taking $\Omega_{\tilde{a}}^{\rm NTP}$ into account, see Fig. 3.1.

As discussed in Sec. 3.1, the temperature $T_f^{\tilde{a}}$ at which axinos decouple from the thermal plasma in the early universe can be very high. Accordingly, axinos decouple as a relativistic species in scenarios with $T_{\rm R} > T_f^{\tilde{a}}$. The resulting relic density, given by (3.3), is then insensitive to the precise value of $T_{\rm R}$. Thus, in this section, scenarios with $T_{\rm R} < T_f^{\tilde{a}}$ where the axino dark matter can be efficiently produced via thermal scattering processes of particles that are in thermal equilibrium [124–127] are considered. For ease of reference, the relic density of the thermally produced axinos (3.5) [125] is reprinted here from Sec. 3.1

$$\Omega_{\tilde{a}}^{\rm TP}h^2 \simeq 5.5\, g_{\rm s}^6(T_{\rm R}) \log\left(\frac{1.211}{g_{\rm s}(T_{\rm R})}\right)\left(\frac{10^{11}\,{\rm GeV}}{f_a}\right)^2\left(\frac{m_{\tilde{a}}}{0.1\ {\rm MeV}}\right)\left(\frac{T_R}{10^7\,{\rm GeV}}\right). \quad (3.29)$$

In Fig. 3.11, $(m_{\tilde{a}}, T_{\rm R})$ regions in which the thermally produced axino density (3.29) is within the nominal 3σ range (3.1) are indicated for f_a values between 10^{11} GeV and 10^{14} GeV by grey bands (as labelled). For given values of $m_{\tilde{a}}$ and f_a, $T_{\rm R}$ values above the corresponding band are disfavoured by $\Omega_{\tilde{a}}^{\rm TP} > \Omega_{\rm dm}$, see also [118, 125, 126, 130, 131].

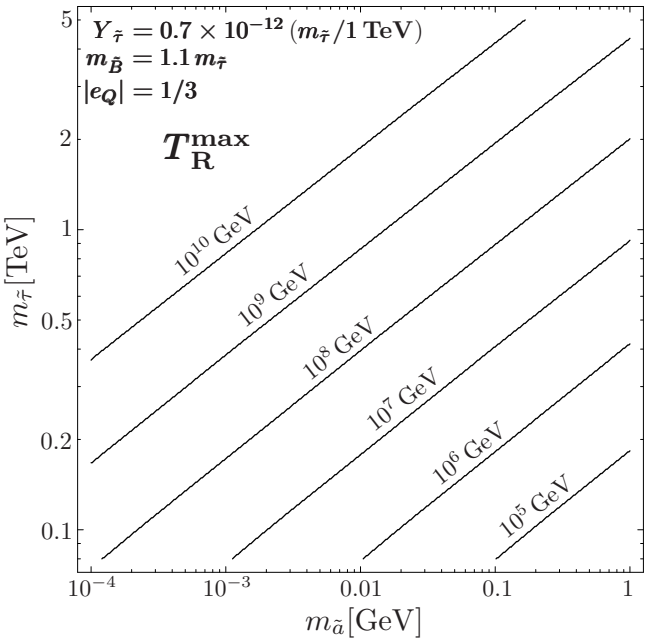

Figure 3.12: Upper limits on the reheating temperature T_R imposed by $\Omega_{\tilde{a}}^\mathrm{TP}h^2 \leq 0.126$ and by the CBBN limit on f_a given by the upper solid black line (^{9}Be) in Fig. 3.4, i.e. for $m_{\widetilde{B}} = 1.1\,m_{\tilde{\tau}}$, $Y_{\tilde{\tau}}$ given by (3.8) with $\kappa = 0.7$, $|e_Q| = 1/3$ and $y = 1$.

From (3.29) and Fig. 3.11, it can be seen that the viability of temperatures above $10^9\,\mathrm{GeV}$ points to $f_a > 3 \times 10^{12}\,\mathrm{GeV}$ if one insists that cold axino dark matter, $m_{\widetilde{a}} \gtrsim 100$ keV, provides the dominant component of Ω_dm. Those f_a values and $m_{\widetilde{a}} \lesssim 1$ GeV are thereby favoured by the viability of standard thermal leptogenesis with hierarchical right–handed neutrinos [157–161].

However, the preceding sections have shown restrictive constraints on f_a originating from CBBN effects. Thereby, more severe limits on T_R would come from these CBBN constraints. Figure 3.12 presents upper limits on T_R as imposed by $\Omega_{\widetilde{a}}^\mathrm{TP}h^2 \leq 0.126$ and by the ^{9}Be CBBN limit on f_a given in Fig. 3.4, i.e. for $|e_Q| = 1/3$, $m_{\widetilde{B}} = 1.1\,m_{\tilde{\tau}}$, $Y_{\tilde{\tau}}$ given by (3.8) with $\kappa = 0.7$, and $y = 1$. By considering $m_{\widetilde{a}} \leq 1\,\mathrm{GeV}$, the condition $\Omega_{\widetilde{a}}^\mathrm{NTP} \ll \Omega_\mathrm{dm}$ is fulfilled. The shown limits range from $T_\mathrm{R}^\mathrm{max} = 10^5\,\mathrm{GeV}$ up to $10^{10}\,\mathrm{GeV}$ (as labelled). Once $m_{\tilde{\tau}}$ is determined at colliders, this figure allows $(m_{\widetilde{a}}, T_\mathrm{R})$ combinations that are disfavoured by CBBN and Ω_dm to be inferred. The ^{6}Li CBBN limits on f_a are in close vicinity to the ^{9}Be limit, as can be seen in Fig. 3.4. Thus, the associated $T_\mathrm{R}^\mathrm{max}$ lines are not shown since they agree basically with the ones shown in Fig. 3.12. For $|e_Q| = 1$, $T_\mathrm{R}^\mathrm{max}$ becomes less restrictive by almost exactly two orders of magnitude. For example, the $T_\mathrm{R}^\mathrm{max} = 10^9\,\mathrm{GeV}$ line for $|e_Q| = 1$ is in close vicinity to the $T_\mathrm{R}^\mathrm{max} = 10^7\,\mathrm{GeV}$ line in Fig. 3.12.

The obtained upper limits on f_a and T_R are conservative ones. BBN constraints

from hadronic energy emitted in 4–body decays $\widetilde{\tau}_{\rm R} \to \tau \widetilde{a} q \bar{q}$ can become relevant for $\tau_{\widetilde{\tau}} \gtrsim 100$ s. Fig. 3.10 shows how these hadronic BBN constraints – imposed mainly by observationally inferred limits on primordial deuterium – result in more restrictive f_a limits than obtained from CBBN alone, and thereby $T_{\rm R}^{\rm max}$ values that are more restrictive than the ones in Fig. 3.12. The hadronic constraints are shown to start becoming more restrictive for $m_{\widetilde{\tau}} \gtrsim 500\,{\rm GeV}$ and $f_a \gtrsim 10^{13}\,{\rm GeV}$. Effects of late energy injection on ^{6}Li from CBBN have been included in the gravitino LSP case, e.g. in [93, 95, 108, 162], where the resulting constraints differ only marginally from the ones obtained without taking this effect into account [89, 96, 163]. A similar outcome is expected for the $\widetilde{a}$ LSP case.

The limits on f_a and $T_{\rm R}$ that are presented in Figs. 3.4 and 3.12, respectively, do not rely on a measurement of $\tau_{\widetilde{\tau}}$. They result from upper limits $\tau_{\widetilde{\tau}}^{\rm max}$ imposed by the CBBN constraints,

$$\tau_{\widetilde{\tau}} \leq \tau_{\widetilde{\tau}}^{\rm max} < 10^4\,{\rm s}, \tag{3.30}$$

which show only a very mild dependence on $m_{\widetilde{\tau}}$ for typical yields such as (3.8) with $\kappa = 0.7$, see Fig. 3.3. In fact, based on (3.30), it is possible to derive analytic expressions for the upper limits on f_a and $T_{\rm R}$ in a conservative way.

Aiming at an instructive derivation, the LL part of the stau lifetime (2.32) is used

$$\tau_{\widetilde{\tau}} \approx \tau_{\widetilde{\tau}\,{\rm LL}} \equiv \Gamma(\widetilde{\tau}_{\rm R} \to \tau \widetilde{a})^{-1}_{\rm LL} \tag{3.31}$$

$$\gtrsim \frac{512\pi^5 c_W^8}{81\,\alpha^4 e_Q^4}\,\frac{f_a^2}{m_{\widetilde{\tau}}\,m_{\widetilde{B}}^2}\left[\log\left(\frac{y^2 f_a^2}{2m_{\widetilde{\tau}}^2}\right)\right]^{-2} \tag{3.32}$$

$$\gtrsim 3.78\times 10^3\,{\rm s}\left(\frac{1/3}{e_Q}\right)^4\left(\frac{f_a}{10^{12}\,{\rm GeV}}\right)^2\left(\frac{100\,{\rm GeV}}{m_{\widetilde{\tau}}}\right)\left(\frac{100\,{\rm GeV}}{m_{\widetilde{B}}}\right)^2, \tag{3.33}$$

where (3.32) underestimates $\tau_{\widetilde{\tau}\,{\rm LL}}$ by at most 2% (15%) for $m_{\widetilde{a}} \lesssim 0.1 m_{\widetilde{\tau}}$ ($m_{\widetilde{a}} \lesssim 0.25 m_{\widetilde{\tau}}$). Focusing on the collider–friendly region $m_{\widetilde{\tau}} \lesssim 1$ TeV, $f_a \lesssim 3\times 10^{13}\,{\rm GeV}$ is imposed by CBBN for $|e_Q| = 1/3$ and $y = 1$. Based on this and on the LEP bound $m_{\widetilde{\tau}} \gtrsim 80$ GeV, $\log(y^2 f_a^2/2m_{\widetilde{\tau}}^2) \lesssim 52.6$ is used to get from (3.32) to (3.33). Accordingly, $\tau_{\widetilde{\tau}\,{\rm LL}}$ can be underestimated by (3.33) by a factor of $\mathcal{O}(1)$ at $f_a \ll 3\times 10^{13}\,{\rm GeV}$ and/or 80 GeV $\ll m_{\widetilde{\tau}} \lesssim 1$ TeV. Nevertheless, (3.33) allows the constraint (3.30) to be translated in a conservative way into the following upper limit:

$$f_a \lesssim 1.63\times 10^{12}\,{\rm GeV}\left(\frac{e_Q}{1/3}\right)^2\left(\frac{\tau_{\widetilde{\tau}}^{\rm max}}{10^4\,{\rm s}}\right)^{1/2}\left(\frac{m_{\widetilde{\tau}}}{100\,{\rm GeV}}\right)^{1/2}\left(\frac{m_{\widetilde{B}}}{100\,{\rm GeV}}\right) \equiv f_a^{\rm max}. \tag{3.34}$$

A comparison with the numerically obtained ^{9}Be limits at $m_{\widetilde{a}}^2/m_{\widetilde{\tau}}^2 \ll 1$ shows a good overall agreement for $\tau_{\widetilde{\tau}}^{\rm max} \approx 5\times 10^3$ s. The associated analytical expression however is less restrictive (i.e. more conservative) than the numerically obtained limits towards larger $m_{\widetilde{\tau}}$. In fact, there the actual $\tau_{\widetilde{\tau}}^{\rm max}$ value imposed by CBBN becomes more restrictive as can be seen in Fig. 3.3.

Turning to $T_{\rm R}$, a conservative limit can be imposed on it

$$T_{\rm R} \lesssim 1.7 \times 10^6\,{\rm GeV} \left(\frac{\Omega_{\rm dm}h^2}{0.1}\right) \left(\frac{f_a}{10^{11}\,{\rm GeV}}\right)^2 \left(\frac{0.1\,{\rm MeV}}{m_{\widetilde{a}}}\right), \tag{3.35}$$

by

$$\begin{aligned}\Omega_{\rm dm}h^2 &\geq \Omega_{\widetilde{a}}^{\rm TP}h^2 \\ &\gtrsim 0.6 \left(\frac{10^{11}\,{\rm GeV}}{f_a}\right)^2 \left(\frac{m_{\widetilde{a}}}{0.1\ {\rm MeV}}\right) \left(\frac{T_R}{10^7\,{\rm GeV}}\right).\end{aligned} \tag{3.36}$$

Here the constant "conservative" prefactor 0.6 accounts for the $T_{\rm R}$–dependent prefactor in (3.5), which stays in the range $0.6 < 5.5\,g_{\rm s}^6(T_{\rm R})\log[1.211/g_{\rm s}(T_{\rm R})] < 1.06$ for $10^4\,{\rm GeV} \leq T_{\rm R} \leq 10^{12}\,{\rm GeV}$ if the MSSM 1–loop renormalisation group running of g_s is considered. Using the upper limit (3.34) in (3.35), one arrives immediately at an analytic expression for the CBBN–imposed limit,

$$\begin{aligned}T_{\rm R} \lesssim 4.4 \times 10^8\,{\rm GeV} &\left(\frac{e_Q}{1/3}\right)^4 \left(\frac{\Omega_{\rm dm}h^2}{0.1}\right) \left(\frac{0.1\,{\rm MeV}}{m_{\widetilde{a}}}\right) \\ &\times \left(\frac{\tau_{\widetilde{\tau}}^{\rm max}}{10^4\,{\rm s}}\right) \left(\frac{m_{\widetilde{\tau}}}{100\,{\rm GeV}}\right) \left(\frac{m_{\widetilde{B}}}{100\,{\rm GeV}}\right)^2 \equiv T_{\rm R}^{\rm max},\end{aligned} \tag{3.37}$$

which is conservative. For $\tau_{\widetilde{\tau}}^{\rm max} \approx 5 \times 10^3\,{\rm s}$, a good overall agreement is again found with the limits obtained numerically. However, as expected from its derivation, the associated analytic expression can be by a factor of $\mathcal{O}(1)$ less restrictive than the numerical results shown in Fig. 3.12.

Since $\tau_{\widetilde{\tau}}$ depends on the ratio f_a/e_Q^2, the limits (3.34) and (3.37) depend on e_Q and thus on the specific axion model. It would therefore be particularly valuable to discover the axion and its mass since the relation between m_a and f_a does not depend on e_Q, see (1.21). If f_a can thus be determined, $T_{\rm R}^{\rm max}$ would be given by (3.35) directly. In addition, e_Q could be found in a $\tau_{\widetilde{\tau}}$ measurement or a lower limit on it derived from the CBBN constraints (3.30).

In this respect, it is noted that most axion searches probe the axion–photon–coupling $g_{a\gamma\gamma} = \alpha C_{a\gamma\gamma}/(2\pi f_a)$ in certain ranges of the axion mass m_a, see [50] and references therein. In the models considered, $C_{a\gamma\gamma}$ is given by (1.34)) so that $g_{a\gamma\gamma}$ does also depend on f_a and e_Q [164]. An axion discovery at an $(m_a, g_{a\gamma\gamma})$ combination would thus be associated with an (f_a, e_Q) combination in the considered models. The e_Q value from axion searches could then be compared to the one inferred from a $\tau_{\widetilde{\tau}}$ measurement at colliders or, if this is not possible, to its lower limit imposed by CBBN.

The region in which the presented BBN constraints are expected to become relevant is explored by the ADMX experiment which searches for resonant conversion of dark matter axions into photons in a microwave cavity. Axion searches of this type are

sensitive to $g_{a\gamma\gamma}$ only in the combination $g^2_{a\gamma\gamma}\rho_a$, where ρ_a denotes the local halo density of axions. If axinos provide the dominant component of cold dark matter, ρ_a can be very small so that no signals will appear at the expected $g_{a\gamma\gamma}$ values. An axion signal in such a direct search would in turn imply a sizeable axion density, $\Omega_a \sim \Omega_{\rm dm}$, and thereby a restrictive $T_{\rm R}$ limit in the considered $m_{\widetilde{a}}$ range, $m_{\widetilde{a}} \gtrsim 0.1$ MeV, given by (3.35) or (3.37) with $\Omega_{\rm dm} \to \Omega_{\rm dm} - \Omega_a$. Alternatively, evidence for solar axions could appear in the Tokyo Axion Helioscope or CAST. This would imply $\Omega_a \ll \Omega_{\rm dm}$, $f_a \lesssim 10^9\,{\rm GeV}$ and thus $T_{\rm R} \ll 10^6\,{\rm GeV}$ in the considered axino cold dark matter scenarios, see (3.35) with $m_{\widetilde{a}} \gtrsim 0.1$ MeV. Here the CBBN constraints will be relevant only in the exceptional cases with $e_Q \to 0$ and/or $m_{\widetilde{a}} \to m_{\widetilde{\tau}}$.

Chapter 4

Axinos at Colliders

Although cosmological considerations such as BBN can significantly constrain the parameter space of the hadronic axion model, in order to investigate and determine the properties of axinos, or indeed, discover them, one must look towards laboratory experiments. Due to the axino's highly suppressed interactions, its production cross sections at various colliders are very small. Instead, one would look for the NLSPs, the staus, either from direct pair production or cascade decays of heavier sparticles. A first hint towards axino dark matter would come from the appearance of quasi-stable staus at the Tevatron or future colliders. Collider studies of CHAMPs, a category to which the staus belong, can be found for example in [165–170].

The most straightforward property of the stau to determine would be its mass $m_{\tilde{\tau}}$, which can be measured using time-of-flight (TOF) data from the muon chambers. At the LHC, it is estimated that this can be done to $< 1\%$ accuracy [171, 172]. In order to measure other properties, such as the stau lifetime $\tau_{\tilde{\tau}}$ and the axino mass $m_{\tilde{a}}$, it is important to be able to study the stau decays. The approach that should be taken to analyse these decays depends on $\tau_{\tilde{\tau}}$. If the lifetime is very short such that the decay length $c\tau_{\tilde{\tau}} \ll \mathcal{O}(\text{cm})$ then the staus would effectively decay immediately after production. This decay length corresponds to $\tau_{\tilde{\tau}} \ll 10^{-10}\,\text{s}$. For the axino model considered in this paper, a stau with such a short lifetime can only be achieved with a very low f_a and a very heavy stau, as well as e_Q larger than what has so far been considered here. For example, with the lowest f_a value allowed (see Sec. 1.1.2), $f_a \approx 10^9\,\text{GeV}$, one would need $m_{\tilde{\tau}} \gtrsim 2\,\text{TeV}$, along with $m_{\tilde{a}} = 10\,\text{GeV}$, $m_{\widetilde{B}}/m_{\tilde{\tau}} = 2$, $y = 1$ and $|e_Q| = 1$, to obtain $\tau_{\tilde{\tau}} \approx 6 \times 10^{-9}\,\text{s}$. This very high stau mass is out of the reach of current and near future colliders. If one considers a stau mass that is more likely to be probed at colliders, $m_{\tilde{\tau}} = 300\,\text{GeV}$ while keeping $f_a \approx 10^9\,\text{GeV}$, along with the selection of $m_{\widetilde{B}}/m_{\tilde{\tau}} = 1.1$, $y = 1$ and $|e_Q| = 1/3$ as in Chapter 3, one obtains a lifetime of $\tau_{\tilde{\tau}} \approx 3 \times 10^{-4}\,\text{s}$.

If the lifetime is such that the decay length is $\mathcal{O}(\text{cm}) \lesssim c\tau_{\tilde{\tau}} \lesssim L$, where L is the size of the detector, then the staus will decay with a displaced vertex within the

beam pipe or the detectors. For a decay length $c\tau_{\tilde{\tau}} \gtrsim L$, there would be no in–flight decays and most of the staus would escape the detector. In fact, the last two scenarios are not necessarily so well separated. In [173, 174] it has been shown that even with $\tau_{\tilde{\tau}} \sim 10^{-(3-5)}$s (corresponding to decay lengths well over L), a substantial number of decays can be observed within the detectors. For the scenario where most of the staus would escape the detector, it is possible to study the decays of the staus by placing a heavy material stopper–detector around the main detector [175,176]. Through large ionisation losses, many staus can be trapped inside the material and their decays studied. The surrounding rock can also be used in this manner. For very long lifetimes, there was a suggestion to place a water tank around the detector to trap the staus, such that the water can be moved to a different location at a later date for further analyses [175]. Note that this method is not limited to staus with long lifetimes, and indeed can also be used to study staus with very short lifetimes but highly boosted momenta.

The focus in this thesis is placed on the third scenario with the decay length $c\tau_{\tilde{\tau}} \gtrsim L$, but without the inclusion of additional stopping detectors. Instead the fraction of staus that are produced with small values of $\beta\gamma$ such that they lose enough kinetic energy through ionisation to be stopped within the detectors are studied. In principle, the following discussion can be applied to either the LHC or future linear colliders. A linear collider has the advantage of being able to fine–tune the centre of mass energy such that the number of staus stopped in the detectors can be maximised. However, depending on the particle mass spectrum and the lifetime of the stau, it could also be possible to extract some (s)particles' properties from LHC phenomenology [177]. The authors of [177] suggest the possibility of having a trigger for a beam dump should such a stau be detected to have stopped, so that its subsequent decay can be observed, or of studying the decays of the staus during beam downtime. Recently there was also a study [178] on measuring the lifetime of staus trapped in the ATLAS detector at the LHC. However, in this study, the decays of the staus are only measured during scheduled shutdown periods and it is thus more suitable for investigating very long–lived staus.

In the next section, the prospects of studying stopped staus at both the LHC and the ILC are explored. For the LHC part of this work, the approach of [177] is closely followed for the stau lifetime measurements. In the case of a study at a linear collider, [179] is used as a basis. For concreteness, four SUSY benchmark points are chosen to illustrate the arguments. To simplify matters and minimise the number of parameters that have to be specified, the study is done in the framework of CMSSM, employing the spectrum calculator SuSpect [180] in micrOMEGAs 2.4 [134, 135] to calculate the mass spectra and verify that the accelerator constraints are respected for these chosen points. The relevant parameters are summarised in Table 4.1.

The axino mass remains a free parameter which is chosen to be $m_{\tilde{a}} = 10\,\text{GeV}$. Furthermore the following parameters are set to $f_a = 10^{11}\,\text{GeV}$, $y = 1$ and $|e_Q| = 1/3$. The left–right mixing of the lightest stau was kept to a minimum, and all the scenarios

Scenario	M_0	$M_{1/2}$	$\tan\beta$	$m_{\widetilde{\tau}}$ [GeV]	$m_{\widetilde{B}}$ [GeV]	$m_{\widetilde{e}_{\rm R}}$ [GeV]	κ
A	170	560	30	210.3	232.4	270.1	0.73
B	50	550	8	207.6	226.8	212.4	1.34
C	138	435	25	174.3	177.7	215.6	1.42
D	135	700	6	290.2	292.6	292.8	1.94

Table 4.1: Model points in CMSSM that emulate some of the scenarios explored in Chapter 3. The mass spectra are produced using micrOMEGAs 2.4 [134,135] and the spectrum calculator SuSpect [180]. The other input parameters are set to $A_0 = 0$, $\mathrm{sgn}(\mu) = 1$ and $m_t = 172.5\,\mathrm{GeV}$.

outlined in Table 4.1 have $\lesssim 35\%$ left–handed component in $\widetilde{\tau}_1$. This can easily be reduced by fine–tuning the parameters or considering other SUSY scenarios that offer greater flexibility in choosing parameters. The CMSSM points are chosen such that the scenarios outlined in Chapter 3 are reproduced. For the purpose of comparison, the values of κ as defined in (3.8) are also included.

4.1 Collider signatures of Axino DM Scenarios

Using Pythia 6.4 [181] and the cuts 1–4 outlined in [177], events were generated using LHC–compatible parameters with a centre of mass energy $\sqrt{s} = 14\,\mathrm{TeV}$ and an integrated luminosity $\mathcal{L} = 10\,\mathrm{fb}^{-1}$. The resulting $|\vec{p}_{\widetilde{\tau}}|/m_{\widetilde{\tau}}$ spectra are shown in Fig. 4.1.

Following the strategy outlined in [177], only the staus produced with $\beta\gamma \leq 0.45$ are considered as trapped in the calorimeter of the detector. The lifetime of the trapped staus is determined by measuring the time between when the stau is stopped and when its subsequent decay is detected. In [177], details on the different techniques one would use for different stau lifetimes can be found. By extrapolating the results of [177] to the parameter points considered here, the expected statistical precisions of the stau lifetime determination listed in Table 4.2 are obtained.

Scenario	$m_{\tilde{u}_R}$	$m_{\tilde{g}}$ [GeV]	$\sigma_{\rm SUSY}$ [pb]	$N_{\widetilde{\tau}}^{\rm stopped}$	$\tau_{\widetilde{\tau}}$ [s]
A	1127.2	1272.8	0.66	119	5.4 ± 0.8
B	1097.5	1250.3	0.76	182	5.8 ± 0.6
C	896.4	1008.3	2.60	522	10.8 ± 0.7
D	1372.1	1563.6	0.185	58	2.5 ± 0.5

Table 4.2: Expected number of staus to be stopped in the calorimeter of the detector at the LHC and the resulting statistical accuracy of the determination of $\tau_{\widetilde{\tau}}$. These numbers are obtained for centre of mass energy $\sqrt{s} = 14\,\mathrm{TeV}$ and integrated luminosity $\mathcal{L} = 10\,\mathrm{fb}^{-1}$. Also shown are $m_{\tilde{g}}$ and $\sigma_{\rm SUSY}$, which are relevant parameters in the study.

Clearly the statistical accuracy depends on the number of events that can be ob-

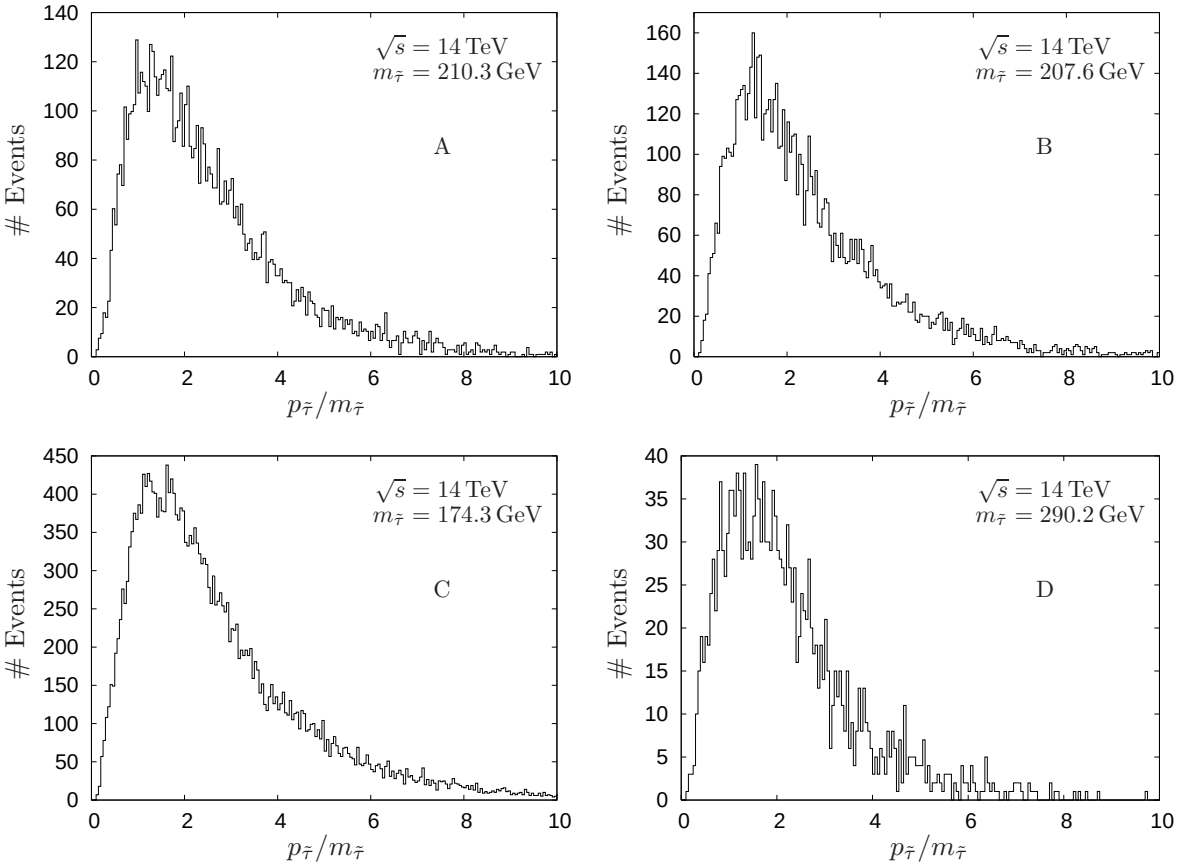

Figure 4.1: $|\vec{p_{\tilde{\tau}}}|/m_{\tilde{\tau}}$ distribution of the staus corresponding to the CMSSM points in Table 4.1 generated using LHC–compatible parameters with centre of mass energy $\sqrt{s} = 14\,\text{TeV}$ and normalised to the integrated luminosity $\mathcal{L} = 10\,\text{fb}^{-1}$. The cuts 1–4 outlined in [177] have been applied.

served, and at the LHC, this is very much dictated by the mass spectrum of the SUSY scenario that is realised. With the conditions assumed for the generation of the above events, light squarks and gluinos with masses $m_{\tilde{q},\tilde{g}} \lesssim 1\,\text{TeV}$ would be preferred for a statistical accuracy of $\lesssim 10\%$. Note that a change in $m_{\widetilde{a}}$ is not likely to affect the stau lifetimes and the associated errors derived above, as long as $m_{\widetilde{a}}^2/m_{\widetilde{\tau}}^2 \ll 1$. However, the same is not true for a change in f_a, on which the stau lifetime strongly depends (see (2.14)). After also factoring in systematic and theoretical uncertainties, a precise measurement of the stau lifetime at the LHC appears very challenging.

A similar analysis can be done for a future linear collider. In [179] it has been proposed that the LDC [182] can be used at the ILC to study the decays of the trapped staus. The staus produced in the collisions can become trapped either in the hadronic calorimeter or the yoke. The strategy of [179] is followed closely to determine the statistical accuracy with which the properties of the stau and/or axino can be determined. Again using Pythia 6.4 [181], events are generated using ILC–compatible parameters

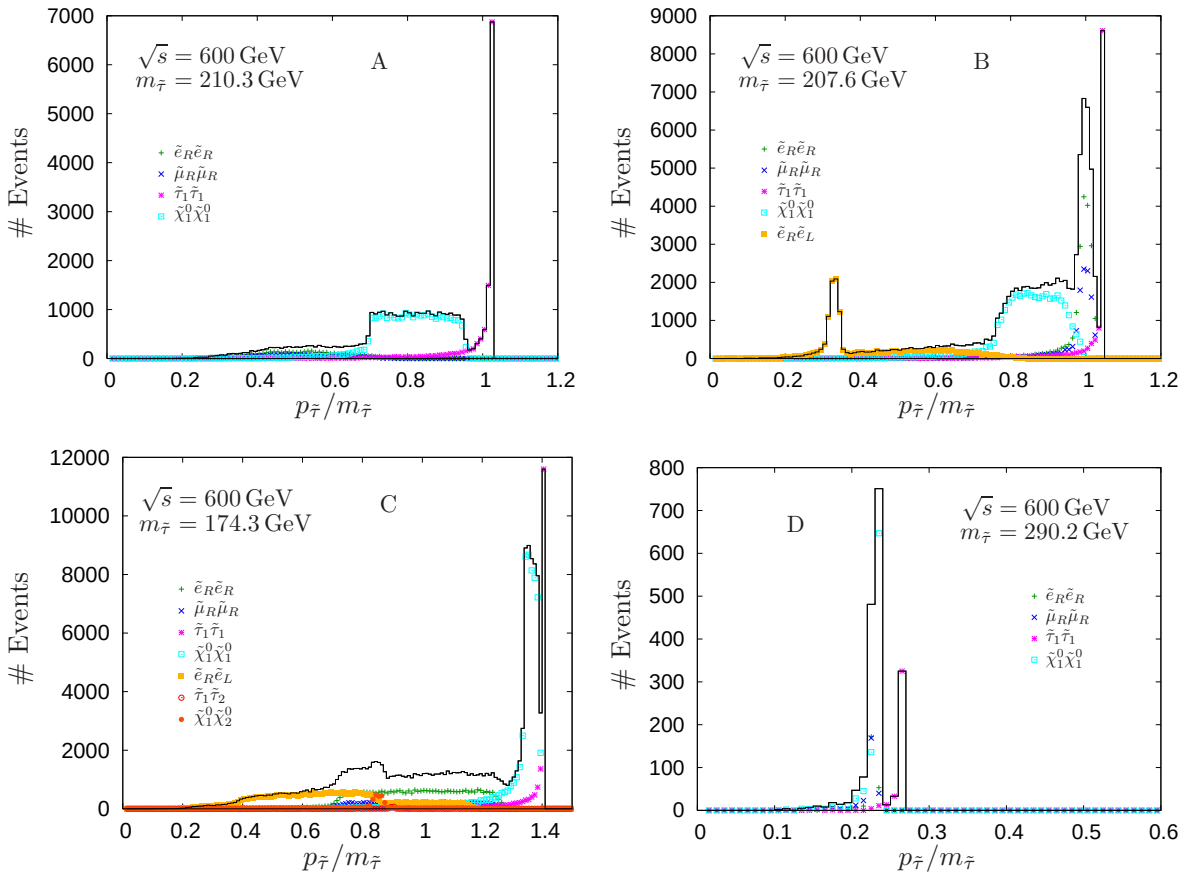

Figure 4.2: $|\vec{p_{\tilde{\tau}}}|/m_{\tilde{\tau}}$ spectra of the CMSSM points in Table 4.1 generated using ILC–compatible parameters with centre of mass energy $\sqrt{s} = 600\,\text{GeV}$ and normalised to the integrated luminosity $\mathcal{L} = 250\,\text{fb}^{-1}$. There are contributing processes from $\widetilde{\text{e}}_R\widetilde{\text{e}}_R$ (green), $\widetilde{\mu}_R\widetilde{\mu}_R$ (blue), $\widetilde{\tau}_1\widetilde{\tau}_1$ (magenta), $\tilde{\chi}_1^0\tilde{\chi}_1^0$ (cyan), $\widetilde{\text{e}}_R\widetilde{\text{e}}_L$ (yellow), $\widetilde{\tau}_1\widetilde{\tau}_2$ (black) and $\tilde{\chi}_1^0\tilde{\chi}_2^0$ (orange).

with centre of mass energy $\sqrt{s} = 600\,\text{GeV}$ and integrated luminosity $\mathcal{L} = 250\,\text{fb}^{-1}$. From analyses of the staus trapped in the calorimeter, it is possible to extract the axino mass using the endpoints of the energy distribution of the tau emitted in the subsequent 2–body decay $\widetilde{\tau}_\text{R} \to \tau\widetilde{a}$. The measurement of the stau lifetime utilises the staus trapped in both the calorimeter and the yoke. The kinematics from the direct production of stau pairs allow for the determination of the stau mass. The $|\vec{p_{\tilde{\tau}}}|/m_{\tilde{\tau}}$ distributions for the produced staus are illustrated in Fig. 4.2 and a summary of the result is tabulated in Table 4.3.

For scenario D, the staus are produced with such low momenta that they do not have enough energy to reach the hadronic calorimeter. One can see in the lower right plot of Fig. 4.2 that almost all the events are clustered around the $|\vec{p_{\tilde{\tau}}}|/m_{\tilde{\tau}} \approx 0.2 - 0.3$ region. However, they are energetic enough to travel out of the beam pipe and become trapped in the inner detectors. For this scenario all the staus produced, 1814, are thus

Scenario	$\sigma_{\widetilde{\tau}}$ [fb]	$N_{\widetilde{\tau}}^{\text{hcal}}$	$N_{\widetilde{\tau}}^{\text{yoke}}$	$m_{\widetilde{\tau}}$ [GeV]	$\tau_{\widetilde{\tau}}$ [s]	$m_{\widetilde{a}}$ [GeV]
A	84	508	1362	210.3 ± 0.2	5.4 ± 0.2	10 ± 64
B	190	681	1311	207.6 ± 0.2	5.8 ± 0.2	10 ± 58
C	310	1569	2933	174.3 ± 0.1	10.8 ± 0.3	10 ± 35
D	3.6	0	0	290.2 ± 0.2	2.5 ± 0.1	10 ± 53

Table 4.3: Expected number of staus to be stopped in the detector of a future ILC and the resulting expected accuracy of the determination of $m_{\widetilde{\tau}}$, $\tau_{\widetilde{\tau}}$ and $m_{\widetilde{a}}$ for $\sqrt{s} = 600\,\text{GeV}$ and integrated luminosity $\mathcal{L} = 250\,\text{fb}^{-1}$, as extrapolated from [179].

treated as stopped to derive the respective measurement accuracies.

The effects of the small mass degeneracies between the stau and the sleptons and/or the lightest neutralino can be seen in the breakdown of the contributing processes to the production of the staus shown in Fig. 4.2. This can be seen most clearly in the plot for scenario B, where $m_{\widetilde{e}_R}/m_{\widetilde{\tau}} \approx 1.02$. Two of the peaks visible in the plot come from cascade decays of $\widetilde{\text{e}}_R\widetilde{\text{e}}_R$, $\widetilde{\mu}_R\widetilde{\mu}_R$ and $\widetilde{\text{e}}_R\widetilde{\text{e}}_L$. In addition, a significant fraction of the staus that are produced in all four plots come from the decays of the lightest neutralino $\tilde{\chi}_1^0$. This indicates that a neutralino that is not too much heavier than the stau would be preferred for phenomenological studies. Table 4.3 shows that the most accurate measurement that could be done at the ILC in this framework would be of the stau mass, where the errors for all four CMSSM points remain below 1%. This can perhaps be further improved if combined with a mass extraction using TOF data. The stau lifetime measurements are not as accurate, but greatly improve with increasing numbers of trapped staus.

Note that these scenarios have not been optimised and it would certainly be favourable to tune the centre of mass energy $\sqrt{s}$ such that the number of trapped staus is maximised. The statistical accuracy achieved here is already very promising with the exception of that obtained for $m_{\widetilde{a}}$. Unfortunately, the smaller the ratio $m_{\widetilde{a}}/m_{\widetilde{\tau}}$, the less accurate it becomes to determine the value of $m_{\widetilde{a}}$ from the energy distribution of the τ. A large $m_{\widetilde{a}}/m_{\widetilde{\tau}}$ ratio is therefore favourable for collider measurements of $m_{\widetilde{a}}$.

Measurements of the values of $\tau_{\widetilde{\tau}}$, $m_{\widetilde{\tau}}$, $m_{\widetilde{B}}$ and $m_{\widetilde{a}}$ can be used to approximately constrain the PQ scale f_a using the leading log formula given in (2.32)

$$\frac{f_a^2}{e_Q^4}\log^2\left(\frac{y^2 f_a^2}{2m_{\widetilde{\tau}}^2}\right) \approx \left(\frac{\tau_{\widetilde{\tau}}^{\text{LL}}}{52\,\text{s}}\right)\left(\frac{m_{\widetilde{\tau}}}{100\,\text{GeV}}\right)\left(\frac{m_{\widetilde{B}}}{110\,\text{GeV}}\right)^2\left(1-\frac{m_{\widetilde{a}}^2}{m_{\widetilde{\tau}}^2}\right) \times (10^{11}\,\text{GeV})^2\left[\log\left(\frac{10^{11}\,\text{GeV}}{\sqrt{2}\times 100\,\text{GeV}}\right)^2\right]^{-2} . \tag{4.1}$$

Note that it is not possible to constrain f_a alone as it always appears as the ratio e_Q^4/f_a^2 in the prefactor of the decay widths, and as the product yf_a in the large logarithm, see (2.15) and (2.24).

4.2 Distinguishing between $\widetilde{a}$ LSP and $\widetilde{G}$ LSP

Should a long–lived charged massive particle be detected at a collider, it is not a given that its decay products include an axino. Despite being able to accurately determine the lifetime of the NLSP and its other properties, there can remain ambiguities over the identities of its non–SM decay products, i.e. the LSP. In particular, the gravitino can be the LSP in several supersymmetric models, and similarly to the axino it is very weakly interacting, leading to long lifetimes of the stau NLSP. The gravitino mass strongly depends on the model and the SUSY breaking mechanism and can thus often be treated as a free parameter. In gauge–mediated breaking schemes, it is very easy to obtain a very light gravitino in the eV range [183–185] while gravity–mediated SUSY breaking schemes give gravitinos typically in the GeV to TeV range [20, 186, 187].

One way in which one can try to distinguish between an axino LSP and a gravitino LSP is by studying the 3–body decay of the stau $\widetilde{\tau}_{\mathrm{R}} \to \tau\gamma + \not{E}$ [115, 188, 189]. In [115, 188], the authors focused on the double differential distribution of the 3–body decays while in [189] the total 3–body branching ratios was considered in more detail.

First an updated comparison of [115, 188] using the result of the full calculation of the 2– and 3–body decays of the stau into the axino is presented, which eliminates the previously unknown ξ factor, as discussed in Chapter 2. The discussion from [115, 188] about the lifetime of the stau remains valid.

Figure 4.3 shows the normalised double differential distributions of the 3–body $\widetilde{\tau}_{\mathrm{R}} \to \tau\gamma\widetilde{a}/\widetilde{G}$ decays as a function of x_γ and $\cos\theta$, with $x_\gamma^{\mathrm{cut}} = 0.2$ and $x_\theta^{\mathrm{cut}} = 0.134$

$$\frac{1}{\Gamma(\widetilde{\tau}_{\mathrm{R}} \to \tau\, X\, \gamma; x_\gamma^{\mathrm{cut}} = 0.2, x_\theta^{\mathrm{cut}} = 0.134)} \frac{\mathrm{d}^2\Gamma(\widetilde{\tau}_{\mathrm{R}} \to \tau\, X\, \gamma)}{\mathrm{d}x_\gamma\, \mathrm{d}\cos\theta}, \qquad X = \widetilde{a}, \widetilde{G}. \tag{4.2}$$

The darker shadings correspond to higher number of events, with the contours representing the values 0.2, 0.4, 0.6, 0.8, 1.0, 1.5 and 2.0. The first three panels show the axino LSP case for different values of $m_{\widetilde{B}}/m_{\widetilde{\tau}}$ while the lower right panel shows the gravitino LSP case. The chosen values for the parameters are $m_{\widetilde{\tau}} = 100\,\mathrm{GeV}$ for all the panels and $f_a = 10^{11}\,\mathrm{GeV}$ and $m_{\widetilde{a}}^2/m_{\widetilde{\tau}}^2 \ll 1$ for the axino panels.

To varying degrees, all the panels show a preference for producing soft and collinear photons. The top right panel is the scenario most closely resembling the first of the two plots illustrated in Fig. 5 of [115]. Here an excess of events for highly energetic photons produced back–to–back to the staus is seen, in agreement with the result found in [115], and one now notes how this excess region changes with different stau–bino mass degeneracy. For $m_{\widetilde{B}} \approx m_{\widetilde{\tau}}$, the excess events cover a larger phase space to also include photons produced at up to $\cos\theta \approx 0$. As $m_{\widetilde{B}}/m_{\widetilde{\tau}}$ increases, the excess region shrinks such that for $m_{\widetilde{B}}/m_{\widetilde{\tau}} = 2.0$ (lower left panel) the excess region vanishes altogether. This is due to the one–loop decay mode being more dominant over the two–loop decay mode as the $\widetilde{B}$ becomes more and more on–shell. In contrast, as $m_{\widetilde{B}}/m_{\widetilde{\tau}}$ increases in the

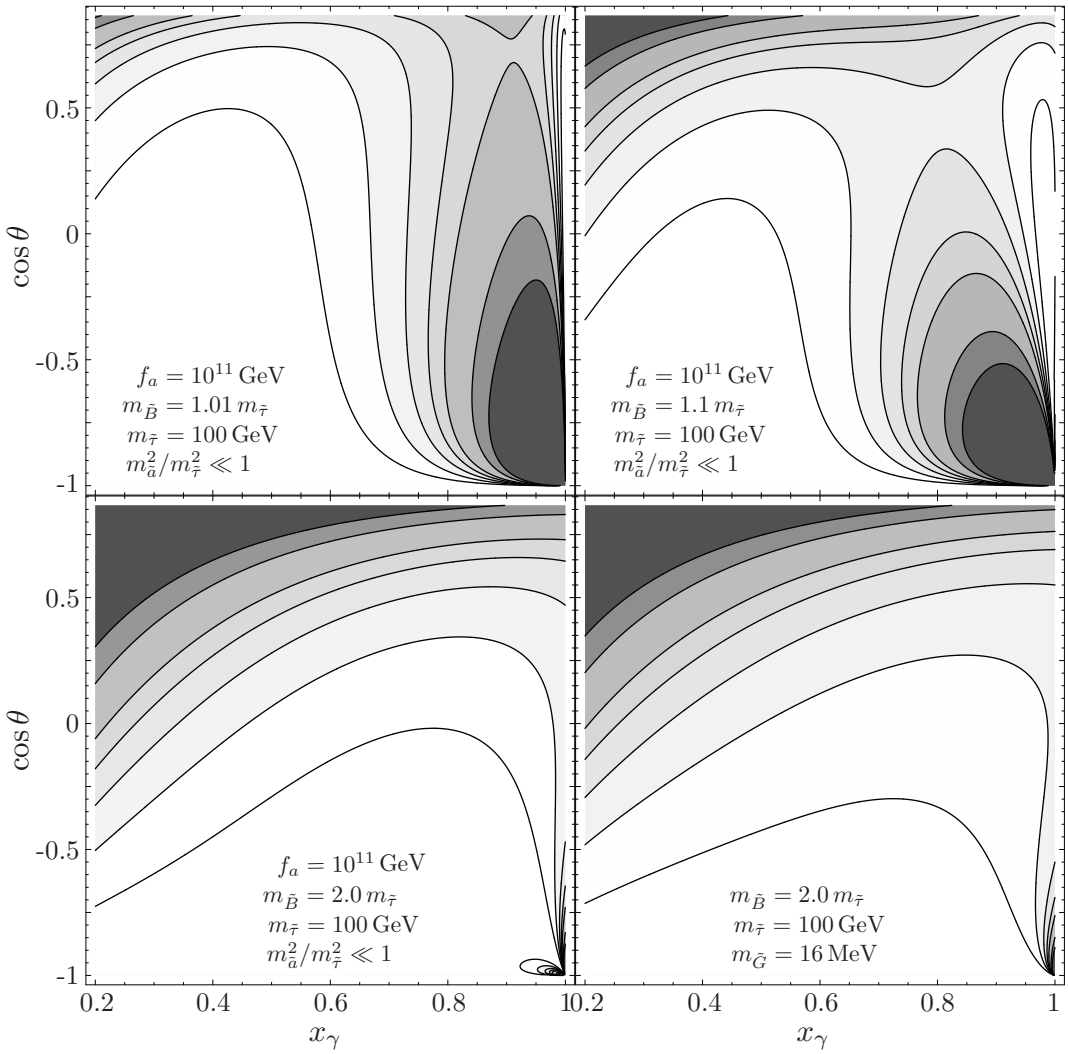

Figure 4.3: The normalised double differential distribution of the 3–body decay $\widetilde{\tau}_{\mathrm{R}} \to \tau\widetilde{a}\gamma$. The lower right panel shows the distribution for $\widetilde{\tau}_{\mathrm{R}} \to \tau\widetilde{G}\gamma$, where the lifetime of the stau is similar to the lifetime of the stau producing the distribution shown in the lower left panel. The contours shown in the plots represent the values 0.2, 0.4, 0.6, 0.8, 1.0, 1.5 and 2.0. The cut parameters are set to $x_\gamma^{\mathrm{cut}} = 0.2$ and $x_\theta^{\mathrm{cut}} = 0.134$. The other parameters are set to $m_{\tilde{\tau}} = 100\,\mathrm{GeV}$, $f_a = 10^{11}\,\mathrm{GeV}$, $m_{\tilde{a}}^2/m_{\tilde{\tau}}^2 \ll 1$, $|e_Q| = 1/3$, $y = 1$.

gravitino LSP case, more events are produced in the very hard photon region. It must be noted however that this increase is very marginal and would require high statistics to be noticeable. Changes in $m_{\widetilde{G}}$, while significantly altering the stau lifetime, do not greatly affect the differential distribution shown in the figure as long as $m_{\widetilde{G}}^2/m_{\tilde{\tau}}^2 \ll 1$. Likewise, increases in the values of f_a and $m_{\tilde{\tau}}$ cause only very slight increases of the normalised double differential 3–body decays.

The lower right panel showing the distribution for the gravitino shows that the larger the $m_{\widetilde{B}}/m_{\widetilde{\tau}}$ ratio, the more difficult it becomes to differentiate an axino LSP scenario from a gravitino LSP scenario. In fact, the parameters for the gravitino case have been chosen to most closely resemble the axino case to its left to illustrate the most difficult situation that can be encountered when trying to distinguish between an axino and a gravitino LSP case. These correspond to $m_{\widetilde{B}}/m_{\widetilde{\tau}} = 2.0$ and a gravitino mass that gives a similar stau lifetime to the one obtained for the stau in the lower left panel. Looking closely at these lower two distributions, small differences are noted, with the axino LSP scenario having a larger phase space area in which no events are produced. However, these differences are small and large statistics and precise measurements would be needed to rely on them for a distinction between the two scenarios.

To give an idea of the numbers that can be expected, 5000 trapped staus whose decays can be observed are assumed, which would be feasible at the ILC. For consistency, the same cuts on the photon energy and the production angle are used as in [189], $x_\gamma^{\rm cut} = 20/m_{\widetilde{\tau}}$ and $x_\theta^{\rm cut} = 0.134$, which is discussed more below. First the whole phase space within the cuts are looked at and the plots are considered in the sequence of left to right and top to bottom. For 5000 trapped staus, the expected number of 3–body events to be seen are 149±12, 58±8, 26±5 and 28±5, respectively. Looking at the region in which the excess can be found, $\cos\theta < -0.5$ and $x_\gamma > 0.8$, it is expected that 53±7 (36% of the total number of 3–body events), 19±4 (33%), 0.3±0.6 (1.4%), 0.4±0.6 (1.4%) events are seen, respectively. This looks very pessimistic for distinguishing between the axino LSP and gravitino LSP scenario with $m_{\widetilde{B}}/m_{\widetilde{\tau}} = 2.0$. If the phase space region is enlarged to $\cos\theta < 0$ while keeping $x_\gamma > 0.8$, the numbers of events change to 0.7±0.8 (3.5%) and 1.5±1.2 (5.2%), respectively, for these two cases. Admittedly the improvement is not large, but in lieu of other signals, this discrepancy could be indicative.

While in principle a distinction between the two scenarios using the same method is also possible at the LHC, the low numbers of staus expected to be trapped within the existing detectors there (see Table 4.2) mean that this line of study would be ambitious, unless the bino and stau masses are almost degenerate. In the LHC related study presented in [189], the authors proposed installing massive stoppers next to the CMS detector at the LHC, in which the staus would be trapped and subsequently, decay. With this stopper detectors set–up, it is possible that more staus are stopped, as a larger $\beta\gamma$ range can be accessed. However, the increase in the number of trapped staus has to be more than tenfold to make this distinction between an axino LSP and a gravitino LSP scenario feasible, especially if $m_{\widetilde{B}} = 2.0\, m_{\widetilde{\tau}}$ is realised, as illustrated above by the numbers calculated in the context of the ILC.

Instead of the differential distributions of the 3–body decay of the $\widetilde{\tau}_{\rm R}$, one can instead focus on the total 3–body branching ratios, as in [189]. Using the results from [115], it was shown in [189] that the success of the distinction between the axino LSP and the gravitino LSP depends on the fudge factor ξ (see Sec. 2.2). With the calculation

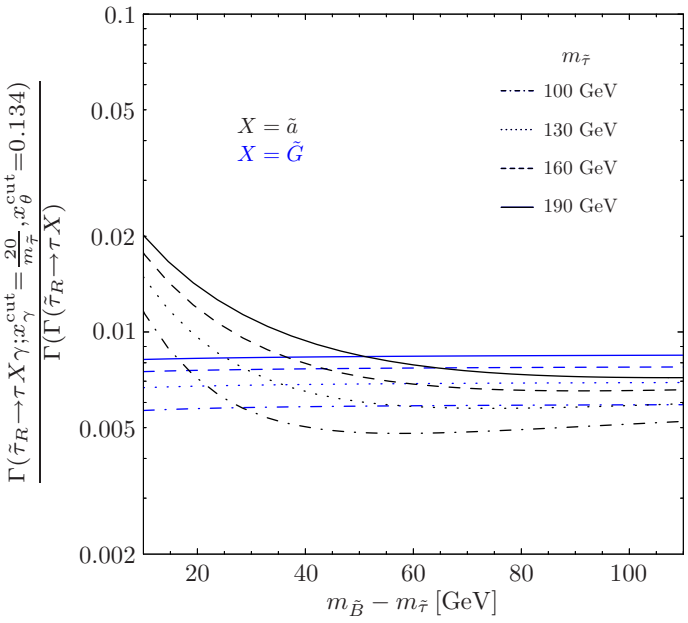

Figure 4.4: The branching ratio of the 3–body decay $\widetilde{\tau}_{\rm R} \to \tau\widetilde{a}\gamma$ and $\widetilde{\tau}_{\rm R} \to \tau\widetilde{G}\gamma$ as a function of $m_{\widetilde{B}} - m_{\widetilde{\tau}}$ for four different $m_{\widetilde{\tau}}$, as labelled. The black lines represent the branching ratios into the axino while the blue lines represent the branching ratios into the gravitino. The parameters in the hadronic KSVZ model are set to $f_a = 10^{11}\,\text{GeV}$, $|e_Q| = 1/3$, $y = 1$.

presented in this thesis, the ambiguity related to the ξ factor is eliminated and the different scenarios presented in [189] can be related to different values of f_a.

In Fig. 4.4 a plot corresponding to Fig. 16 in [189] is presented showing the branching ratio

$$\frac{\Gamma(\widetilde{\tau}_{\rm R} \to \tau X\gamma; x_\gamma^{\rm cut} = \frac{20}{m_{\widetilde{\tau}}}, x_\theta^{\rm cut} = 0.134)}{\Gamma(\widetilde{\tau}_{\rm R} \to \tau X)}, \qquad X = \widetilde{a}, \widetilde{G}, \tag{4.3}$$

as a function of $(m_{\widetilde{B}} - m_{\widetilde{\tau}})$. The same values for the cut parameters, $x_\gamma^{\rm cut} = 20/m_{\widetilde{\tau}}$ and $x_\theta^{\rm cut} = 0.134$, are adopted. The blue lines represent the branching ratios of the staus decaying into the gravitino for $m_{\widetilde{\tau}} = 100, 130, 160, 190\,\text{GeV}$, shown by the dot–dashed, dotted, dashed and solid curves, respectively. The black curves that increase towards smaller $(m_{\widetilde{B}} - m_{\widetilde{\tau}})$ correspond to $X = \widetilde{a}$ for $\xi = 1$ in [189]. From the presented calculation, it can be determined that this in fact corresponds to a combination of values of $f_a = 10^{11}\,\text{GeV}$, $|e_Q| = 1/3$ and $y = 1$. An enhancement in the 3–body branching ratios for the decay into the axino is observed at small $(m_{\widetilde{B}} - m_{\widetilde{\tau}})$ due to the 2–body decay being proportional to the bino mass squared, $\Gamma(\widetilde{\tau}_{\rm R} \to \tau\widetilde{a}) \propto m_{\widetilde{B}}^2$, while the 3–body decay is not. Clearly, this is not so different from the stau decays into the gravitino, unless $(m_{\widetilde{B}} - m_{\widetilde{\tau}})$ is small. The difference in the 3–body branching ratios between an axino LSP and a gravitino LSP scenario also becomes larger for smaller

values of y or f_a if the other parameters are fixed.

While collider experiments can certainly allow us to determine the lifetime and mass of the stau fairly accurately, determining the properties, or indeed the identity, of the LSP that it decays into is more challenging. Due to the very similarly weak couplings of the gravitino, it is highly difficult to eliminate the ambiguity over whether the LSP is an axino or a gravitino in collider experiments. As such, a discovery of axions would greatly help in determining and/or constraining the parameters of the underlying model.

Chapter 5

Scenarios with $m_{\widetilde{a}}, m_{\widetilde{G}} < m_{\widetilde{\tau}}$

Now the possibility of the existence of the gravitino in the mass spectrum of the models studied in this thesis is considered. The gravitino is the gauge field associated with local SUSY transformations. Its mass $m_{\widetilde{G}}$ – which depends on the SUSY breaking mechanism and the SUSY breaking scale – governs the strength of its interactions, which are suppressed by inverse powers of the reduced Planck scale $\mathrm{M_{Pl}} = 2.4 \times 10^{18}\,\mathrm{GeV}$ but can be enhanced by the goldstino components. In fact, the gravitino is another extremely weakly interacting particle that can be thermally produced in the early universe. The mass of the gravitino $m_{\widetilde{G}}$ determines its place in the spectrum with respect to the $\widetilde{a}$ and the $\widetilde{\tau}_{\mathrm{R}}$ and thereby its possible implications.

In the above chapters, the scenario where $m_{\widetilde{a}} < m_{\widetilde{\tau}}$, i.e. an axino LSP and a stau NLSP was considered. Equivalently, the study can be generalised to the scenario $m_{\widetilde{a}} < m_{\widetilde{\tau}} \ll m_{\widetilde{G}}$. It can be realised, e.g. in a scenario with gravity–mediated SUSY breaking leading to $m_{\widetilde{G}} = \mathcal{O}(1\ \mathrm{TeV})$. Such a heavy gravitino decays typically during or after BBN such that its decay products can affect the primordial abundances of deuterium and of other light nuclei. Successful BBN does thereby impose additional constraints on T_{R} that can be more restrictive than the ones presented in Sec. 3.5: $T_{\mathrm{R}} \lesssim 10^{8}\,\mathrm{GeV}$ for $m_{\widetilde{G}} \lesssim 5\,\mathrm{TeV}$ and $T_{\mathrm{R}} \gtrsim 10^{9}\,\mathrm{GeV}$ becomes typically viable only for $m_{\widetilde{G}} \gtrsim 5\,\mathrm{TeV}$ [152,162].

In Chapter 4 the hierarchy $m_{\widetilde{G}} < m_{\widetilde{\tau}} < m_{\widetilde{a}}$ (or equivalently, a supersymmetric scenario with no PQ extension) was considered in the context of differentiating the experimental signatures of an axino LSP and a gravitino LSP. This is the gravitino LSP scenario for which CBBN constraints on T_{R} have already been explored [89, 96, 97, 163, 190] and for which the CBBN–imposed f_a limit does not exist. It has already been shown in Chapter 4 that the axino and gravitino LSP scenarios have very similar collider signatures and distinguishing one from the other can be highly non–trivial. This gravitino LSP scenario can also be associated with different upper limits on T_{R}. For example, it has been found that $T_{\mathrm{R}} \gtrsim 10^{9}\,\mathrm{GeV}$ can be associated with an upper limit on the gluino–slepton mass ratio of $m_{\tilde{g}}/m_{\tilde{l}} \lesssim 3$ for $m_{\tilde{l}} \lesssim 1\,\mathrm{TeV}$ in the $\widetilde{G}$ LSP case [190].

Limiting the study in this chapter to the hierarchy $m_{\widetilde{a}} < m_{\widetilde{\tau}}$, yet another two orderings of the masses are possible, $m_{\widetilde{a}} < m_{\widetilde{G}} < m_{\widetilde{\tau}}$ and $m_{\widetilde{G}} < m_{\widetilde{a}} < m_{\widetilde{\tau}}$, and the consequences of both of these are explored in this chapter. This can occur, for example, in a hadronic axion model with gauge–mediated SUSY breaking [191]. Of course, these ranges also imply the decays $\widetilde{a} \to \widetilde{G}X$ and $\widetilde{G} \to \widetilde{a}X$. Given that their rates suffer from a suppression by the Planck scale, these decays are assumed to occur too late to affect CBBN or hadronic BBN.

Naturally, the question arises on how the above cosmological constraints and phenomenological signatures look should not just one or the other, but both particles are lighter than the long–lived stau. Without making any statements as to which of the gravitino and axino is the LSP, the effects this may have on the constraints and analyses performed in the preceding sections can be explored.

Let us first take a look at how the lifetime of the stau is affected. As in Sec. 2.4, the lifetime of the stau is approximated to the the inverse of the 2–body decay width,

$$\tau_{\widetilde{\tau}}^{\mathrm{comb}} = \frac{1}{\Gamma_{\mathrm{tot}}^{\widetilde{\tau}}} \approx \frac{1}{\Gamma_{\mathrm{tot}}^{\widetilde{\tau},2\mathrm{b}}} = \frac{1}{\Gamma(\widetilde{\tau}_{\mathrm{R}} \to \tau\widetilde{G}) + \Gamma(\widetilde{\tau}_{\mathrm{R}} \to \tau\widetilde{a})} \,. \tag{5.1}$$

The result from [115] is used for the width of the 2–body decay of the stau into the gravitino $\Gamma(\widetilde{\tau}_{\mathrm{R}} \to \tau\widetilde{G})$

$$\Gamma(\widetilde{\tau}_{\mathrm{R}} \to \tau\widetilde{G}) = \frac{m_{\widetilde{\tau}}^5}{48\pi m_{\widetilde{G}}^2 \mathrm{M}_{\mathrm{Pl}}^2} \left(1 - \frac{m_{\widetilde{G}}^2}{m_{\widetilde{\tau}}^2}\right)^4 \,. \tag{5.2}$$

The decay into the gravitino is governed mainly by $m_{\widetilde{G}}$, while working in the limit of $m_{\widetilde{a}}^2/m_{\widetilde{\tau}}^2 \ll 1$ minimises the dependency of the decay into the axino on $m_{\widetilde{a}}$. Thus the behaviour of the stau lifetime can be parameterised in terms of $m_{\widetilde{G}}$ and f_a. Figure 5.1 shows lifetime contours of the stau as a function of $m_{\widetilde{G}}$ and f_a (dotted lines). The solid magenta lines indicate the fractional contribution of the partial 2–body decay width into the axino to the total 2–body decay width of the stau

$$\Gamma_{\widetilde{a}}^{2\mathrm{b}} \equiv \Gamma(\widetilde{\tau}_{\mathrm{R}} \to \tau\widetilde{a}) = x\,\Gamma_{\mathrm{tot}}^{\widetilde{\tau},2\mathrm{b}}, \qquad x = 0.01, 0.1, 0.5, 0.9, 0.99. \tag{5.3}$$

There are clear turning points in the lifetime contours indicating the region in which the lifetime is governed by the decay into the gravitino and that in which it is governed by the decay into the axino.

Figure 5.2 is the corresponding plot for the 3–body branching ratio

$$\mathrm{BR}(3\text{–body}; x_\gamma^{\mathrm{cut}}; x_\theta^{\mathrm{cut}}) \equiv \frac{\Gamma_{\mathrm{tot}}^{\widetilde{\tau},3\mathrm{b}}}{\Gamma_{\mathrm{tot}}^{\widetilde{\tau},2\mathrm{b}}} = \frac{\Gamma(\widetilde{\tau}_{\mathrm{R}} \to \tau\widetilde{a}\gamma; x_\gamma^{\mathrm{cut}}; x_\theta^{\mathrm{cut}}) + \Gamma(\widetilde{\tau}_{\mathrm{R}} \to \tau\widetilde{G}\gamma; x_\gamma^{\mathrm{cut}}; x_\theta^{\mathrm{cut}})}{\Gamma_{\mathrm{tot}}^{\widetilde{\tau},2\mathrm{b}}}. \tag{5.4}$$

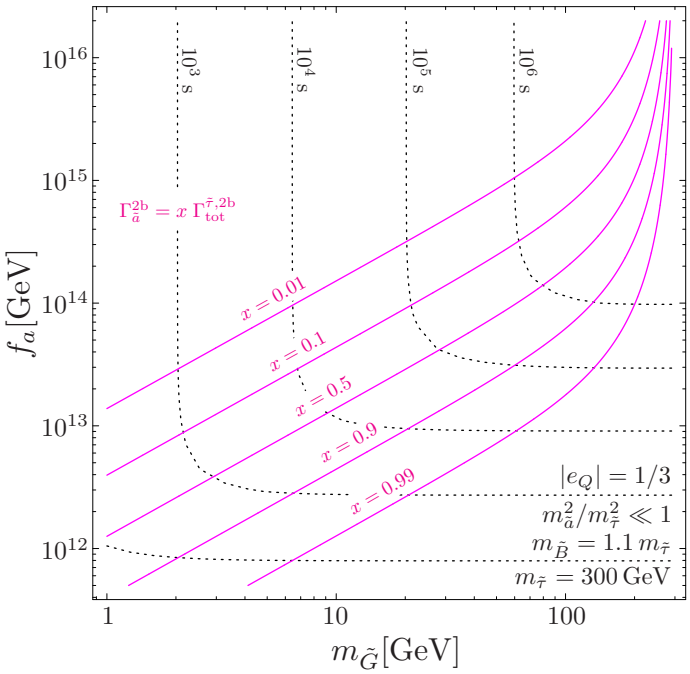

Figure 5.1: Behaviour of the stau lifetime when it can undergo 2–body decays into both the axino and the gravitino ($m_{\widetilde{a}}, m_{\widetilde{G}} < m_{\widetilde{\tau}}$), as a function of $m_{\widetilde{G}}$ and the Peccei–Quinn scale, f_a. The dotted lines show lifetime contours while the solid lines indicate the partial decay width of the stau into the axino as a fraction of the total decay width (5.3). The limit $m_{\widetilde{a}}^2/m_{\widetilde{\tau}}^2 \ll 1$ is taken such that the lifetime's dependence on the axino mass is minimised. The other parameters are set to $m_{\widetilde{\tau}} = 300\,\text{GeV}$, $m_{\widetilde{B}} = 1.1\,m_{\widetilde{\tau}}$, $|e_Q| = 1/3$ and $y = 1$.

The dotted lines represent the 3–body branching ratio while the solid magenta lines indicate the 3–body analogue of (5.3)

$$\Gamma^{3b}_{\widetilde{a}} \equiv \Gamma(\widetilde{\tau}_R \to \tau\widetilde{a}\gamma) = x\,\Gamma^{\widetilde{\tau},3b}_{tot}, \qquad x = 0.01, 0.1, 0.5, 0.9, 0.99. \tag{5.5}$$

Again, the result from [115] is used for $\Gamma(\widetilde{\tau}_R \to \tau\widetilde{G}\gamma)$. For consistency $x_\gamma^{cut} = 20/300 \approx 0.07$ and $x_\theta^{cut} = 0.134$ are used, as in Chapter 4.

The combined 4–body branching ratio of the stau decaying into the axino and gravitino is shown in Fig. 5.3

$$\text{BR(4–body)} \equiv \frac{\Gamma^{\widetilde{\tau},4b}_{tot}}{\Gamma^{\widetilde{\tau},2b}_{tot}} = \frac{\Gamma(\widetilde{\tau}_R \to \tau\widetilde{a}q\bar{q}) + \Gamma(\widetilde{\tau}_R \to \tau\widetilde{G}q\bar{q})}{\Gamma^{\widetilde{\tau},2b}_{tot}}, \tag{5.6}$$

where the expression for the decay into the gravitino is taken from [115]. Again, the solid magenta lines indicate contours of the contribution of the decay into the axino to the total decay width

$$\Gamma^{4b}_{\widetilde{a}} \equiv \Gamma(\widetilde{\tau}_R \to \tau\widetilde{a}q\bar{q}) = x\,\Gamma^{\widetilde{\tau},4b}_{tot}, \qquad x = 0.01, 0.1, 0.5, 0.9, 0.99. \tag{5.7}$$

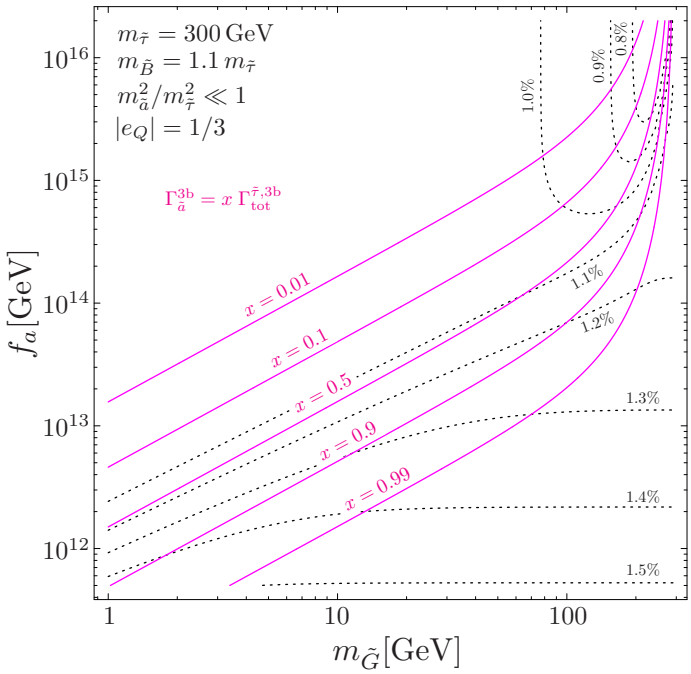

Figure 5.2: Branching ratio of the 3–body decay of the stau $\widetilde{\tau}_{\mathrm{R}} \to \tau\gamma\widetilde{a}/\widetilde{G}$ ($m_{\widetilde{a}}, m_{\widetilde{G}} < m_{\widetilde{\tau}}$), as a function of $m_{\widetilde{G}}$ and the Peccei–Quinn scale, f_a. The dotted lines show contours of the branching ratio (5.4) while the solid magenta lines indicate the partial decay width of the stau into the axino as a fraction of the total decay width (5.5), similar to Fig. 5.1. The limit $m_{\widetilde{a}}^2/m_{\widetilde{\tau}}^2 \ll 1$ is taken where the lifetime loses its dependence on the axino mass. The other parameters are set to $m_{\widetilde{\tau}} = 300\,\mathrm{GeV}$, $m_{\widetilde{B}} = 1.1\,m_{\widetilde{\tau}}$, $|e_Q| = 1/3$ and $y = 1$.

where the dotted lines show values of the 4–body branching ratio. It can be seen that the inclusion of the decay into the gravitino modifies the stau branching ratios in non–trivial ways.

The effects of this scenario on the constraints considered in Chapter 3 are straightforward. The combined lifetime given by (5.1) is used for the stau lifetime, which affects all aspects of the considered cosmological constraints. For the constraints stemming from late hadronic energy injection, the effects from the decay into the gravitino and the axino are combined in an additive manner

$$\epsilon_{\mathrm{had}}^{\mathrm{tot}} = \frac{1}{\Gamma_{\mathrm{tot}}^{\widetilde{\tau}}} \left[\int_{m_{q\bar{q}}}^{m_{\widetilde{\tau}} - m_{\widetilde{a}} - m_\tau} \mathrm{d}m_{q\bar{q}}\, m_{q\bar{q}} \frac{\mathrm{d}\Gamma(\widetilde{\tau}_{\mathrm{R}} \to \tau\widetilde{a}q\bar{q})}{\mathrm{d}m_{q\bar{q}}} + \int_{m_{q\bar{q}}}^{m_{\widetilde{\tau}} - m_{\widetilde{G}} - m_\tau} \mathrm{d}m_{q\bar{q}}\, m_{q\bar{q}} \frac{\mathrm{d}\Gamma(\widetilde{\tau}_{\mathrm{R}} \to \tau\widetilde{G}q\bar{q})}{\mathrm{d}m_{q\bar{q}}} \right], \tag{5.8}$$

where $\Gamma_{\mathrm{tot}}^{\widetilde{\tau}} = 1/\tau_{\widetilde{\tau}}^{\mathrm{comb}}$ with $\tau_{\widetilde{\tau}}^{\mathrm{comb}}$ given by (5.1). The energy injected from the 2–body decay is only slightly more involved. The combined electromagnetic energy injection is

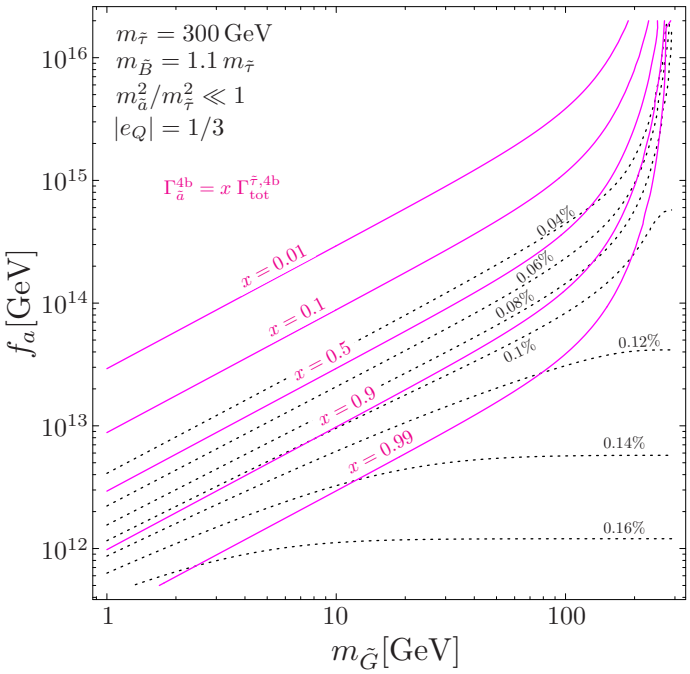

Figure 5.3: Branching ratio of the 4–body decay of the stau $\widetilde{\tau}_{\mathrm{R}} \to \tau q \bar{q} \widetilde{a}/\widetilde{G}$ ($m_{\widetilde{a}}, m_{\widetilde{G}} < m_{\widetilde{\tau}}$), as a function of $m_{\widetilde{G}}$ and the Peccei–Quinn scale, f_a. The dotted lines show contours of the branching ratio (5.6) while the solid magenta lines indicate the partial decay width of the stau into the axino as a fraction of the total decay width (5.7), similar to Fig. 5.1. The limit $m_{\widetilde{a}}^2/m_{\widetilde{\tau}}^2 \ll 1$ is taken where the lifetime's dependency on the axino mass is minimised. The other parameters are set to $m_{\widetilde{\tau}} = 300\,\mathrm{GeV}$, $m_{\widetilde{B}} = 1.1\,m_{\widetilde{\tau}}$, $|e_Q| = 1/3$ and $y = 1$.

defined by

$$\epsilon_{\mathrm{em}}^{\mathrm{tot}} = 0.3 \left[\frac{\Gamma(\widetilde{\tau}_{\mathrm{R}} \to \tau \widetilde{a})}{\Gamma_{\mathrm{tot}}^{\widetilde{\tau},2b}} \frac{m_{\widetilde{\tau}}^2 - m_{\widetilde{a}}^2}{2m_{\widetilde{\tau}}} + \frac{\Gamma(\widetilde{\tau}_{\mathrm{R}} \to \tau \widetilde{G})}{\Gamma_{\mathrm{tot}}^{\widetilde{\tau},2b}} \frac{m_{\widetilde{\tau}}^2 - m_{\widetilde{G}}^2}{2m_{\widetilde{\tau}}} \right]. \tag{5.9}$$

The resulting constraints are illustrated in the $m_{\widetilde{G}}$–f_a plane in Fig. 5.4 for $m_{\widetilde{\tau}} = 1\,\mathrm{TeV}$, $m_{\widetilde{B}} = 1.1\,m_{\widetilde{\tau}}$, $m_{\widetilde{a}}^2/m_{\widetilde{\tau}}^2 \ll 1$ and yield $Y_{\widetilde{\tau}} = 0.7 \times 10^{-12}$. As usual, $|e_Q| = 1/3$ and $y = 1$. As in the previous plots, contours of $\tau_{\widetilde{\tau}} = 10^2$, 10^4, and $10^6\,\mathrm{s}$ are shown by the dotted lines. The magenta lines indicating the proportion of the total decay width of the stau that is the decay into the axino are included for informational purposes. The regions to the right of and above the long–dash–dotted (red) and the solid lines are disfavoured by the CBBN constraints associated with (3.20) and (3.21), respectively. Again, this follows the $\tau_{\widetilde{\tau}} \approx 5 \times 10^3\,\mathrm{s}$ contour. This can be compared to the constraints discussed in Chapter 3, which is summarised in Fig. 3.10. For the purposes of comparison, the constraints obtained at $m_{\widetilde{\tau}} = 1\,\mathrm{TeV}$ are looked at. The effect of the decay mode into the gravitino can be seen starting to dominate the constraints for $m_{\widetilde{G}} \lesssim 100\,\mathrm{GeV}$, where the values of $f_a \gtrsim 3 \times 10^{13}\,\mathrm{GeV}$ are no longer disfavoured, and

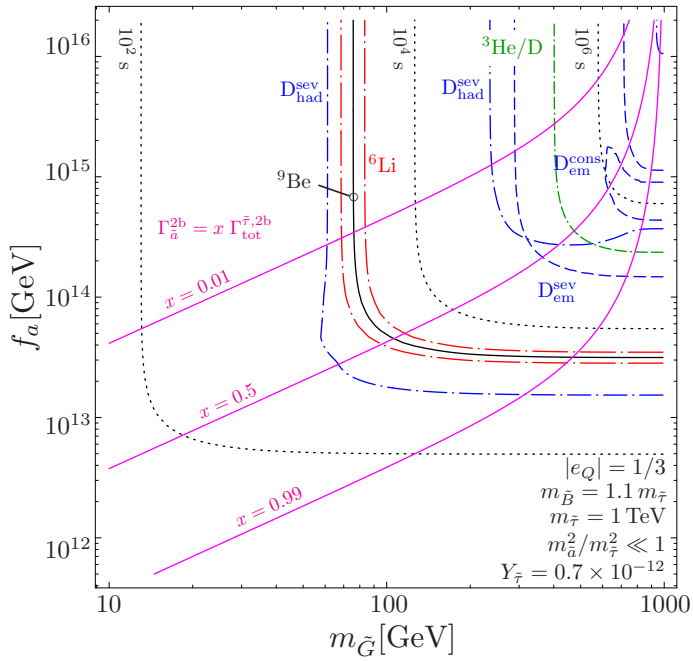

Figure 5.4: Cosmological constraints on the Peccei–Quinn scale f_a as a function of $m_{\widetilde{G}}$. The hadronic BBN constraints associated with (3.23) disfavour the regions in the upper right–hand corner enclosed by the respective short–dash–dotted (blue) lines. Electromagnetic BBN constraints associated with D disfavour the upper regions enclosed by the respective dashed (blue) lines and the ones associated with ^{3}He/D the region above the double–dash–dotted (green) line. The regions to the right of and above the long–dash–dotted (red) and the solid lines are disfavoured by the CBBN constraints associated with (3.20) and (3.21). Contours of $\tau_{\widetilde{\tau}} = 10^2$, 10^4, and 10^6 s are shown by the dotted lines. The other parameters are set to $m^2_{\widetilde{a}}/m^2_{\widetilde{\tau}} \ll 1$, $m_{\widetilde{\tau}} = 1\,\text{TeV}$, $m_{\widetilde{B}} = 1.1\,m_{\widetilde{\tau}}$, $Y_{\widetilde{\tau}} = 0.7 \times 10^{-12}$, $|e_Q| = 1/3$ and $y = 1$.

the CBBN constraints can be evaded altogether. This happens at approximately the point where $\Gamma^{\widetilde{\tau},2b}_{\widetilde{a}} = 0.5\Gamma^{\widetilde{\tau}}_{tot}$.

The hadronic BBN constraints associated with (3.23) and (3.24) are shown by the short–dash–dotted (blue) lines. The conservative constraints are in fact absent in this scenario, in agreement with Fig. 3.10. The severe constraints disfavour the region enclosed in the L–shaped strip of parameter space, bounded by the two long short–dash–dotted blue lines. This shows that the region $2 \times 10^{13}\,\text{GeV} \lesssim f_a \lesssim 4 \times 10^{14}\,\text{GeV}$ is in fact disfavoured for $m_{\widetilde{G}} \gtrsim 60\,\text{GeV}$ rather than for very heavy gravitinos as thought previously (see Fig. 3.10). However, $f_a \gtrsim 3 \times 10^{13}\,\text{GeV}$ is additionally constrained for $60\,\text{GeV} \lesssim m_{\widetilde{G}} \lesssim 300\,\text{GeV}$.

Electromagnetic BBN constraints associated with D disfavour the upper regions enclosed by the respective dashed (blue) lines and the ones associated with ^{3}He/D the region above the double–dash–dotted (green) line. The same pattern as for the hadronic BBN constraints are also observed here, but as already mentioned, they are

of little significance as they lie well within the region already disfavoured by CBBN. So in comparison to the $m_{\widetilde{a}} < m_{\widetilde{\tau}} < m_{\widetilde{G}}$ scenario considered earlier, this scenario opens up previously disfavoured regions of parameter space but also disfavours regions that were previously free of constraints. For $m_{\widetilde{a}}^2/m_{\widetilde{\tau}}^2 \ll 1$ and $m_{\widetilde{\tau}} = 1\,\mathrm{TeV}$, the constraints can be completely evaded if $m_{\widetilde{G}} \lesssim 60\,\mathrm{GeV}$.

In short, the CBBN–induced f_a limit will exist if $\Gamma(\widetilde{\tau}_\mathrm{R} \to \tau\widetilde{a}) \gg \Gamma(\widetilde{\tau}_\mathrm{R} \to \tau\widetilde{G})$. The $T_\mathrm{R}^\mathrm{max}$ contours presented in Sec. 3.5 will then remain as conservative limits in the axino LSP. The restrictive BBN constraints usually associated with an unstable $\widetilde{G}$ can be evaded since the gravitino can decay only into EWIPs [124]: $\widetilde{G} \to \widetilde{a}a$. However, if $m_{\widetilde{a}}$ is not much smaller than $m_{\widetilde{G}}$, there can be a sizeable additional contribution to the axino density, $\Omega_{\widetilde{a}}^{\widetilde{G}\to\widetilde{a}a} = (m_{\widetilde{a}}/m_{\widetilde{G}})\,\Omega_{\widetilde{G}}^\mathrm{TP}$, where $\Omega_{\widetilde{G}}^\mathrm{TP}$ denotes the thermally produced density that the gravitino would have today, if it had not decayed. This leads to more restrictive T_R limits which are now governed by $\Omega_{\widetilde{a}}^\mathrm{TP} + \Omega_{\widetilde{a}}^{\widetilde{G}\to\widetilde{a}a} \leq \Omega_\mathrm{dm}$. In the gravitino LSP case, the upper limit on f_a imposes a lower limit on the thermally produced axino abundance which decays via $\widetilde{a} \to \widetilde{G}a$ into the gravitino density $\Omega_{\widetilde{G}}^{\widetilde{a}\to\widetilde{G}a} = (m_{\widetilde{G}}/m_{\widetilde{a}})\,\Omega_{\widetilde{a}}^\mathrm{TP}$, where $\Omega_{\widetilde{a}}^\mathrm{TP}$ is now the relic density that the axino would have today, if it had not decayed. The T_R limits in this case will be governed accordingly by $\Omega_{\widetilde{G}}^\mathrm{TP} + \Omega_{\widetilde{G}}^{\widetilde{a}\to\widetilde{G}a} \leq \Omega_\mathrm{dm}$. Note however that the CBBN constraints presented in [89, 96, 97, 163, 190] can be evaded since $\tau_{\widetilde{\tau}}$ can be reduced by the new dominant decay mode $\widetilde{\tau}_\mathrm{R} \to \tau\widetilde{a}$. For $\Gamma(\widetilde{\tau}_\mathrm{R} \to \tau\widetilde{a}) \ll \Gamma(\widetilde{\tau}_\mathrm{R} \to \tau\widetilde{G})$, the above discussion can be repeated with one difference: since $\tau_{\widetilde{\tau}}$ is governed by $\widetilde{\tau}_\mathrm{R} \to \tau\widetilde{G}$, the f_a limit can be evaded while the CBBN constraints discussed in [89, 96, 97, 163, 190] and its implications for $\Omega_{\widetilde{G}}^\mathrm{TP}$ become relevant.

There can also be interesting phenomenological consequences of this hierarchy. Should the decays of the staus trapped within the detector at the ILC be studied, there are now two decay modes to consider. Depending on the degeneracy of the axino and gravitino masses, the two modes could be observed very distinctively.

Chapter 6

Conclusions

A KSVZ axion extension of the standard model embedded in supersymmetry has been considered. In the realisation with conserved R–parity, the supersymmetric partner of the axion, the axino, can be the lightest stable supersymmetric particle and thus a dark matter candidate. A simple form of the superpotential that is generic for SUSY hadronic axion models has been considered, in which the axion multiplet interacts with the MSSM multiplets through loops of heavy (s)quarks. While the case with a minimum number of $SU(2)_L$–singlet KSVZ multiplets and with the lightest slepton $\tilde{l}_1$ being a purely right–handed stau $\widetilde{\tau}_{\mathrm{R}}$ has been explored, the study can be generalised to more complicated settings in a straightforward way.

The large scale hierarchy between the Peccei–Quinn scale and the SUSY scale $m_Q \gg m_{\mathrm{SUSY}}$ has been exploited and the method of heavy mass expansion applied to calculate the 2–, 3– and 4–body decays of the stau NLSP into the axino LSP. In the two–loop diagrams, large logarithms of the form $\log\left(y^2 f_a^2/2m_{\widetilde{\tau}}^2\right)$ occur that make these diagrams of the same order of magnitude as the one–loop diagrams and therefore relevant to the leading order calculation. The lifetime $\tau_{\widetilde{\tau}}$ has also been shown to be governed by the 2–body decay $\widetilde{\tau}_{\mathrm{R}} \to \tau\widetilde{a}$, which first occurs at the two–loop level.

Furthermore, cosmological constraints coming from the dark matter density, free–streaming velocity and modified BBN in axino cold dark matter scenarios with a long–lived charged $\widetilde{\tau}_{\mathrm{R}}$ NLSP have been explored. It is found that the $\widetilde{\tau}_{\mathrm{R}}$ can be sufficiently long–lived to allow for efficient catalysis of ^{6}Li and ^{9}Be via bound–state formation with primordial nuclei. Observationally inferred abundances of ^{6}Li and ^{9}Be thus impose upper limits on the stau lifetime $\tau_{\widetilde{\tau}_{\mathrm{R}}}$ for typical thermal relic abundances of the long–lived $\widetilde{\tau}_{\mathrm{R}}$. Additionally, BBN constraints associated with hadronic and electromagnetic energy release has been considered. While the region with $f_a \lesssim 10^{12}\,\mathrm{GeV}$ is typically not affected, those constraints become significant for larger f_a such that models with f_a towards the grand unification scale are disfavoured. It is found that the hadronic BBN constraints on f_a can be more restrictive than those obtained from CBBN constraints. The upper limits on the stau lifetime then allowed for the derivation of upper limits on

the PQ scale f_a that depend mainly on the masses of the stau $m_{\widetilde{\tau}}$ and of the lightest neutralino $m_{\widetilde{\chi}_1^0}$ and on the electric charge of the heavy (s)quarks e_Q.

Using only the CBBN constraints, the obtained limits on f_a imply upper limits on the reheating temperature $T_{\rm R}$ since f_a governs not only $\tau_{\widetilde{\tau}_{\rm R}}$ but also the efficiency of thermal axino production and thereby the $T_{\rm R}$ constraints imposed by $\Omega_{\widetilde{a}}^{\rm TP} \leq \Omega_{\rm dm}$. Both numerical results and analytical approximations has been presented for those BBN–imposed limits and their dependence on $m_{\widetilde{a}}$, $m_{\widetilde{\tau}}$, $m_{\widetilde{\chi}_1^0}$, and e_Q has also been discussed. For example, for $m_{\widetilde{\tau}} = 500\,{\rm GeV}$, $m_{\widetilde{\chi}_1^0} = 1.1\ m_{\widetilde{\tau}}$, and $|e_Q| = 1/3$, it is found that $f_a \lesssim 10^{13}\,{\rm GeV}$ and that $T_{\rm R} \gtrsim 10^9\,{\rm GeV}$ is viable only for $m_{\widetilde{a}} \lesssim 1\,{\rm MeV}$. The even tighter upper limits that can be imposed on the reheating temperature from the hadronic BBN constraints, which are relevant for models of inflation and baryogenesis, were also discussed.

In the study carried out in this thesis, saxion effects were assumed to be negligible, and the results depend crucially on this assumption. In situations in which the saxion dominates the energy density before its decay, the entropy per comoving volume can be enhanced by a factor $\Delta > 1$. If this additional entropy production takes place before $\widetilde{\tau}_{\rm R}$ decoupling, the BBN constraint on f_a will not be affected but the thermally produced axino density can be diluted so that $\Omega_{\widetilde{a}}^{\rm TP} \to \Omega_{\widetilde{a}}^{\rm TP}/\Delta$ and $T_{\rm R}^{\rm max} \to \Delta T_{\rm R}^{\rm max}$. If entropy increases by a large factor of $\Delta > 10^3$ after $\widetilde{\tau}_{\rm R}$ decoupling and before BBN, the $\widetilde{\tau}_{\rm R}$ abundance can be diluted such that catalysed BBN of ^{6}Li and ^{9}Be cannot become efficient. Then the CBBN–imposed constraints on f_a and $T_{\rm R}$ would not exist. Nevertheless, $\Omega_{\widetilde{a}}^{\rm TP} \to \Omega_{\widetilde{a}}^{\rm TP}/\Delta$ so that the $\Omega_{\rm dm}$–imposed limit on $T_{\rm R}$ would be relaxed by a factor of Δ. However note that the baryon asymmetry would also be diluted by a factor of Δ and therefore a larger asymmetry would be needed before its dilution, see [97] for a related discussion in the $\widetilde{G}$ LSP case.

The phenomenological signatures at colliders that can be studied in the framework of the model examined in this thesis were also considered. Four CMSSM points were generated with the focus on scenarios in which the lifetime of the stau NLSP is $\mathcal{O}(10\,{\rm s})$. The possibilities of studying the decays of the staus without installing stopping detectors were explored, which restricts the study to a small sample of the produced staus. At the LHC with centre of mass energy $\sqrt{s} = 14\,{\rm TeV}$ and integrated luminosity $\mathcal{L} = 10\,{\rm fb}^{-1}$, it was shown that a precise measurement of the lifetime would be challenging. The accuracy obtained in these scenarios is at best 10%. For the ILC study, the events were produced with $\sqrt{s} = 600\,{\rm GeV}$ and $\mathcal{L} = 250\,{\rm fb}^{-1}$. The resulting accuracies of the stau lifetime, stau mass and axino mass measurements were highly dependent on the number of staus trapped in the detectors. For the runs illustrated in the study, an average 1% accuracy was obtained for the stau mass and as high as 3% accuracy for the measurement of the lifetime. These numbers can easily be improved by fine–tuning the centre of mass energies of the collisions so as to optimise the numbers of staus trapped in the detectors. On the other hand, the axino mass was shown to be very poorly

determined using the 2–body decay kinematics, which is not expected to significantly improve with higher statistics for low axino to stau mass ratio.

Furthermore the possibility of distinguishing between the collider signatures of an axino and a gravitino LSP scenario was explored. As both particles have very weak couplings to normal matter, their signatures can look very similar at colliders. The 3–body decay $\widetilde{\tau}_{\mathrm{R}} \to \tau X \gamma$ where $X = \widetilde{a}, \widetilde{G}$, was studied in this context and it was shown that the smaller the mass degeneracy between the stau and the bino, the larger is the difference in the fully differential decay distributions between the axino LSP and the gravitino LSP scenario. The decay into the axino LSP in this case has a significant excess in the regions where hard and back–to–back photons are produced as compared to the gravitino LSP. As $m_{\widetilde{B}}/m_{\widetilde{\tau}} \to 2.0$, this deviation was shown to reduce significantly and it becomes almost impossible to distinguish the two cases unless a very large number of events are analysed. The total 3–body branching ratios were also looked at as a means of distinguishing between the two cases. This study similarly showed that the differences between the two cases increase towards smaller $(m_{\widetilde{B}} - m_{\widetilde{\tau}})$ values.

Additionally the ways in which the cosmological constraints presented in this thesis can be affected by the presence of the gravitino $\widetilde{G}$, when it is also lighter than the stau NLSP, were investigated. While the majority of the study focused on the hierarchy $m_{\widetilde{a}} < m_{\widetilde{\tau}} \ll m_{\widetilde{G}}$, the special case of $m_{\widetilde{a}}, m_{\widetilde{G}} < m_{\widetilde{\tau}}$ was briefly studied in this part, exploring the effects of the additional decay of the stau into the gravitino on the total decay widths of the stau. Using this, BBN constraints in this scenario were derived and it was found that the constraints can be significantly weakened and, e.g. evaded for $m_{\widetilde{\tau}} = 1\,\mathrm{TeV}$ if $m_{\widetilde{G}} \lesssim 60\,\mathrm{GeV}$ and $m_{\widetilde{a}}/m_{\widetilde{\tau}} \ll 1$.

If $m_{\widetilde{G}} < m_{\widetilde{\tau}}$ and $\Gamma(\widetilde{\tau}_{\mathrm{R}} \to \tau\tilde{a}) \ll \Gamma(\widetilde{\tau}_{\mathrm{R}} \to \tau\tilde{G})$, $\tau_{\widetilde{\tau}}$ is governed by $\widetilde{\tau}_{\mathrm{R}} \to \tau\widetilde{G}$. Then the f_a limit can be evaded while the CBBN constraints discussed in [89, 96, 97, 108, 162, 163, 190, 192] and their implications for thermally produced gravitino abundance become relevant. On the other hand, if $\Gamma(\widetilde{\tau}_{\mathrm{R}} \to \tau\tilde{a}) \gg \Gamma(\widetilde{\tau}_{\mathrm{R}} \to \tau\tilde{G})$, the hadronic BBN and CBBN limits discussed in this thesis apply. However, the gravitinos lead to an increase of the LSP density, thus leading to more restrictive T_R limits. In this case the results presented in this study remain as conservative upper limits.

The investigations presented in this thesis show that for the interesting case of new long–lived charged particles, BBN constraints play an important role and can be used to restrict the models considerably. These constraints will become particularly important if such particles are produced and detected at the upcoming LHC experiments.

Appendix A

Heavy Mass Expansion and Reduction to Basic Scalar Integrals

A.1 Heavy Mass Expansion

Due to Feynman diagrams that can be highly complex to solve, one can make use of large scale hierarchies involved to simplify the problem. As such, one calculates the asymptotic expansions of Feynman amplitudes in the limits of certain masses and/or momenta. Heavy mass expansion (HME) is one category of such an asymptotic expansion in the limit of a large mass [193, 194]. It applies in the cases where the following assumptions can be made

- each mass can be categorised as either large, M_i, or small, m_i;
- all external momenta are small compared to the large masses, $k_i \ll M_i$.

For a Feynman integral $\mathcal{F}$ of Feynman diagram Γ, the expansion is compactly written as

$$\mathcal{F}(\Gamma) \to \sum_{\gamma} \mathcal{F}(\Gamma \backslash \gamma) * \mathcal{T}_{\{k_i, m_i\}} \mathcal{F}(\gamma) \tag{A.1}$$

where γ represents the subgraphs over which the sum is performed (a subgraph is derived by drawing all possible one–particle irreducible graphs containing the heavy propagators). The operator $\mathcal{T}_{\{k_i,m_i\}}$ performs a Taylor expansion on the subgraphs with respect to the small parameters k_i and/or m_i. $\mathcal{F}(\Gamma \backslash \gamma)$ represents the original graphs where the subgraphs have been shrunk to a point.

When considering processes involving loops, special care must be paid to the loop momenta q_i. Since these are unconstrained by momentum and energy conservation, they can be both of the order of the small parameters and of the large masses. In order to carry out the expansion in a consistent manner, each of the momenta regions must be individually looked out.

For the one–loop processes considered in this paper, there are two such regions. All external momenta and masses outside the heavy (s)quark mass loop are taken to be small. Let us refer to the first diagram in Fig. 2.3 and denote the momentum running through the loop q_2 with the heavy mass scale M. These 2 regions are then defined as follows:

1. $|q_2| \sim M$
2. $|q_2| \ll M$

A Taylor expansion for the second region yields a scaleless integral, which vanishes in dimensional regularisation.

For the two–loop processes, there are four momenta regions that must be considered. Let us refer to the diagrams in Fig. 2.1 and denote the momentum running through the outer loop q_1 and the momentum running through the heavy loop q_2. Then these 4 regions are defined as follows:

1. $|q_1|, |q_2| \sim M$
2. $|q_1| \ll M, |q_2| \sim M$
3. $|q_1| \sim M, |q_2| \ll M$
4. $|q_1|, |q_2| \ll M$

After the appropriate Taylor expansions, the last two regions reduce to scaleless integrals, which vanish in dimensional regularisation. This leaves only the first and second regions, which in practical terms translate into the Taylor expansion of the whole diagram and the Taylor expansion of only the heavy loop with respect to the small parameters, respectively. Figure A.1 gives a pictorial depiction of what is going on in the two–loop case, where the propagators with the large mass parameter M are represented by thick lines and the rest by thin lines.

A.2 Tensor Reduction

Using Passarino–Veltman reduction procedures, the tensor integrals were simplified to scalar ones. Using the following notation,

$$T_0(n_1,n_2,n_3) = \int \mathrm{d}^D q_1 \, \mathrm{d}^D q_2 \frac{1}{(q_1^2 - m_Q^2)^{n_1} (q_2^2 - m_Q^2)^{n_2} (q_1+q_2)^{2n_3}} \,, \tag{A.2}$$

$$T^{\mu_1 \cdots \mu_n \nu_1 \cdots \nu_n}(n_1,n_2,n_3) = \int \mathrm{d}^D q_1 \, d^D q_2 \frac{q_1^{\mu_1} \cdots q_1^{\mu_n} q_2^{\nu_1} \cdots q_2^{\nu_n}}{(q_1^2 - m_Q^2)^{n_1} (q_2^2 - m_Q^2)^{n_2} (q_1+q_2)^{2n_3}} \,, \tag{A.3}$$

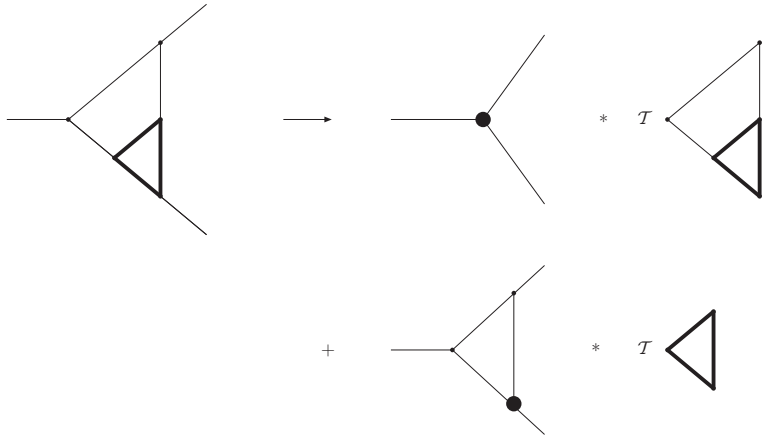

Figure A.1: The leading term in the heavy mass expansion of the two–loop 2–body decay of the stau NLSP into the axino LSP, where the propagators with the large mass parameter M are represented by thick lines and the rest by thin lines. propagators.

the following relations were used in order to reduce the tensor integrals:

$$T^{\mu_1\nu_1}(n_1,n_2,n_3) = \frac{1}{D} g^{\mu_1\nu_1} q_1.q_2 T_0(n_1,n_2,n_3), \tag{A.4}$$

$$T^{\mu_1\mu_2\nu_1\nu_2}(n_1,n_2,n_3) = \frac{1}{D^3+D^2-2D}\Big[\Big\{(D+1)q_1^2q_2^2 - 2(q_1.q_2)^2\Big\} g^{\mu_1\mu_2}g^{\nu_1\nu_2} + \{D(q_1.q_2)^2 - q_1^2q_2^2\}(g^{\mu_1\nu_1}g^{\mu_2\nu_2} + g^{\mu_1\nu_2}g^{\mu_2\nu_1})\Big] T_0(n_1,n_2,n_3), \tag{A.5}$$

where $g^{\mu\nu}$ is the metric tensor and D is the number of dimensions.

A.3 Integration by Part Identities

After applying the heavy mass expansion and tensor reduction formulae, only vacuum two–loop integrals and one–loop integrals are left (the results of which are well–known). The two–loop integrals take the form $T_0(n_1,n_2,n_3)$. These are simplified with the use of integration by parts (IBP) identities, reducing the two–loop integrals to master integrals.

Using the following identities,

$$\int \mathrm{d}^D q_1\, \mathrm{d}^D q_2\, \frac{\partial}{\partial q_1^\mu} \frac{q_1^\mu}{(q_1^2-m_Q^2)^{n_1}(q_2^2-m_Q^2)^{n_2}(q_1+q_2)^{n_3}} = 0 \tag{A.6}$$

$$\int \mathrm{d}^D q_1\, \mathrm{d}^D q_2\, \frac{\partial}{\partial q_1^\mu} \frac{q_2^\mu}{(q_1^2-m_Q^2)^{n_1}(q_2^2-m_Q^2)^{n_2}(q_1+q_2)^{n_3}} = 0 \tag{A.7}$$

$$\int \mathrm{d}^D q_1\, \mathrm{d}^D q_2\, \frac{\partial}{\partial q_2^\mu} \frac{q_1^\mu}{(q_1^2-m_Q^2)^{n_1}(q_2^2-m_Q^2)^{n_2}(q_1+q_2)^{n_3}} = 0 \tag{A.8}$$

$$\int \mathrm{d}^D q_1 \, \mathrm{d}^D q_2 \, \frac{\partial}{\partial q_2^\mu} \frac{q_2^\mu}{(q_1^2 - m_Q^2)^{n_1} (q_2^2 - m_Q^2)^{n_2} (q_1 + q_2)^{n_3}} = 0 \tag{A.9}$$

all the integrals that appear in the calculation are reduced to master integrals. This was implemented using the Automated Integral Reduction program [195]. In fact, in the course of the calculation, there was only one master integral, $T_0(1, 1, 0)$, where the two–loop integral decouples into a product of two one–loop integrals.

Appendix B

Free–Streaming Velocity

Free–streaming is also known as collisionless phase mixing. During this phase, collisionless particles stream out of overdense regions and suppress density fluctuations below the comoving free–streaming scale $\lambda_{\rm FS}$. As explained in Sec. 3.2, $\lambda_{\rm FS}$ is obtained by integrating over the velocity of the particle from the time it is generated to the time of matter-radiation equality $t_{\rm eq}$

$$\lambda_{\rm FS} = \int_{t_i}^{t_{\rm eq}} {\rm d}t \, \frac{v(t)}{a(t)}. \tag{B.1}$$

The comoving velocity of the axino at time t is given by

$$v(t) = \frac{|\vec{p}(t)|}{\sqrt{|\vec{p}(t)|^2 + m^2}}, \tag{B.2}$$

where the momentum at time t can be related to the momentum today using $|\vec{p}(t)| = |\vec{p}_0(t)|a_0/a(t) = |\vec{p}_0(t)|a(t)$. This leads to the relation

$$v(t) = \frac{v_0}{\sqrt{v_0^2 + a(t)^2}}, \tag{B.3}$$

where $p_0 = mv_0$.

In the radiation–dominated epoch

$$\frac{t}{a^2(t)} = \frac{t_{\rm eq}}{a^2(t_{\rm eq})} = t_{\rm eq}(1 + z_{\rm eq})^2. \tag{B.4}$$

This relation can be used in (B.3) and (B.1) to obtain

$$\lambda_{\rm FS}(t_{\rm eq}) = \int_{t_i}^{t_{\rm eq}} {\rm d}t \, \frac{v_0}{a(t)\sqrt{v_0^2 + a(t)^2}}, \tag{B.5}$$

$$= v_0 \, t_{\rm eq} \, (1 + z_{\rm eq})^2 \int_{t_i}^{t_{\rm eq}} {\rm d}t \, \frac{1}{t\sqrt{1 + v_0^2(1 + z_{\rm eq})^2 t_{\rm eq}/t}}. \tag{B.6}$$

After integration, this becomes

$$\lambda_{\rm FS}^0 = \int_{t_i}^{t_{\rm eq}} {\rm d}t\, \frac{v(t)}{a(t)} = v_0\, t_{\rm eq}\, (1+z_{\rm eq})^2\, \log\left(\sqrt{\frac{t_{\rm eq}}{t_i}}\, \frac{1+\sqrt{1+v_0^2\,(1+z_{\rm eq})^2}}{1+\sqrt{1+v_0^2\,(1+z_{\rm eq})^2 (t_{\rm eq}/t_i)}} \right), \quad \text{(B.7)}$$

where (3.12) is then obtained at the limit $t_i \to 0$.

The corresponding free–streaming velocity of the collisionless particle is given by $v_0 \equiv v_{\rm FS}^0$. The form that $v_{\rm FS}^0$ takes depends on the cosmic origins of the particle. In WDM studies, the DM particles are taken to have decoupled from the hot plasma with a thermal spectrum while still relativistic at $T_{\rm f}^{\rm WDM} \gg m_{\rm WDM}$.

The DM particles are taken to be non–relativistic today, so the present day velocity can be written as $\vec{v}_0 = \vec{p}_0/m_{\rm WDM}$. The redshift relation $\vec{p}_0 a_0 = \vec{p}_1 a_1$ relates the present day velocity to its velocity at some time t_1 in the past, where a_i is the scale factor at time t_i. Using

$$g_{*S}(t_0)(a_0 T_0)^3 = g_{*S}(t_1)(a_1 T_1)^3, \quad \text{(B.8)}$$

$\vec{v}_0$ can be rewritten as

$$\vec{v}_0 = \frac{\vec{p}_1}{m}\,\frac{a_1}{a_0} = \frac{\vec{p}_1}{m}\left(\frac{g_{*s}(t_0)}{g_{*s}(t_1)}\right)^{1/3}\frac{T_0}{T_1}. \quad \text{(B.9)}$$

For non–degenerate, relativistic particles that obey Fermi statistics, the root mean square momentum at the time of freeze–out is given by

$$\langle p(T_f^{\rm WDM})\rangle = 3.151\, T_f^{\rm WDM}. \quad \text{(B.10)}$$

Using (B.9), the root mean squared velocity is then

$$\langle \vec{v}_0 \rangle = 3.151\, \frac{T_0}{m_{\widetilde{a}}} \left(\frac{g_{*s}(t_0)}{g_{*s}(T_f^{\rm WDM})} \right)^{1/3}. \quad \text{(B.11)}$$

The density of these thermal relics is given by $\rho_{\rm WDM} = m_{\rm WDM}\, n_{\rm WDM}$ which fixes its abundance to

$$\Omega_{\rm WDM} h^2 = 0.05 \left(\frac{230}{g_{*S}(T_f^{\rm WDM})} \right) \left(\frac{m_{\rm WDM}}{100\,{\rm eV}} \right). \quad \text{(B.12)}$$

Since it is typically assumed that all dark matter is made up of one species of particle, $g_{*S}(T_f^{\rm WDM})$ is fixed by the requirement $\Omega_{\rm WDM} = \Omega_{\rm dm}$, which leads to the following expression for the r.m.s. velocity of WDM

$$(v_{\rm FS}^{\rm rms,0})^{\rm WDM} = 0.75\,{\rm km\,s^{-1}} \left(\frac{\Omega_{\rm dm} h^2}{0.105} \right)^{1/3} \left(\frac{100\ {\rm eV}}{m_{\rm WDM}} \right)^{4/3}, \quad \text{(B.13)}$$

where $T_0 = 2.73\,\mathrm{K}$ and $g_{*S}(t_0) = 3.91$ have been used.

For the specific case of axino dark matter, all three sources of origin that are discussed in Chapter 3 are considered here. These are the thermal relics, thermally produced and non–thermally produced axinos.

B.1 Thermal Relic Axinos

Like the generic WDM considered above, these axinos were once in thermal equilibrium and decoupled from the primordial plasma while still relativistic at $T_{\mathrm{f}}^{\widetilde{a}} \gg m_{\widetilde{a}}$. Thus their r.m.s. momentum is similarly given by

$$\langle p(T_f^{\widetilde{a}})\rangle = 3.151\, T_f^{\widetilde{a}}. \tag{B.14}$$

Without setting $\Omega_{\widetilde{a}}^{\mathrm{therm}} = \Omega_{\mathrm{dm}}$, the value of $g_{*S}(T_f^{\widetilde{a}})$ is not fixed. Instead, with an MSSM realisation with a PQ extension, this can be set to $g_{*S}(T_{\mathrm{R}}) \approx 230$, leading to the r.m.s. value of their present free–streaming velocity given by

$$(v_{\mathrm{FS}}^{\mathrm{rms},0})_{\widetilde{a}}^{\mathrm{therm}} = 0.57\,\mathrm{km\,s^{-1}} \left(\frac{230}{g_{*S}(T_{\mathrm{f}}^{\widetilde{a}})}\right)^{1/3} \left(\frac{100\ \mathrm{eV}}{m_{\widetilde{a}}}\right). \tag{B.15}$$

B.2 Thermally Produced Axinos

As the TP axinos inherit the thermal spectrum of the particles that produce them, they acquire the same free–streaming velocity as the thermal relic axinos (B.11)

$$(v_{\mathrm{FS}}^{\mathrm{rms},0})^{\widetilde{a},\mathrm{TP}} = 0.57\,\mathrm{km\,s^{-1}} \left(\frac{230}{g_{*S}(T_{\mathrm{R}})}\right)^{1/3} \left(\frac{100\,\mathrm{eV}}{m_{\widetilde{a}}}\right). \tag{B.16}$$

B.3 Non–Thermally Produced Axinos

For the present free–streaming velocity of axinos produced from the non–thermal decay of the stau, (B.9) is used as the starting point. Here, time t_1 is the time at which the axinos are produced, which can be set to $t_1 = \tau_{\widetilde{\tau}}$ when using the sudden decay approximation. As the decay is dominated by the 2-body decay $\widetilde{\tau}_{\mathrm{R}} \to \tau\widetilde{a}$, the momentum from the kinematics of this decay can be used to determine the momentum with which the axinos are produced

$$|\vec{p}_{\widetilde{a}}| = \frac{m_{\widetilde{\tau}}^2 - m_{\widetilde{a}}^2 - m_{\tau}^2}{2m_{\widetilde{\tau}}}. \tag{B.17}$$

The energy density determines the expansion rate through the Hubble parameter which, as the decay happens in the radiation dominated epoch, $\tau_{\widetilde{\tau}_{\rm R}} < t_{\rm eq}$, takes the form

$$H^2(t) \equiv \left(\frac{\dot{a}}{a}\right)^2 = \frac{8\pi G_N}{3}\rho_R = \frac{8\pi G_N}{3}\frac{\pi^2}{30}g_*(t)T^4, \tag{B.18}$$

where ρ_R is the radiation density for a flat universe (k=0). In the radiation–dominated era, the radiation density evolves as $\rho_R \propto a^{-4}$. This leads to the Hubble parameter to evolve as $H(t) = 1/2t$, leading to the following expression for the temperature at time t

$$T = \left[\frac{90 \mathrm{M}_{\rm Pl}^2}{4\pi^2 g_*(t) t^2}\right]^{1/4}. \tag{B.19}$$

Substituting this into (B.9), an expression for the present free–streaming velocity of axinos that are non–thermally produced from NLSP decays is obtained in the $m_\tau \to 0$ limit

$$v_{\rm FS}^{0\,\widetilde{a},{\rm NTP}} = \frac{1}{m_{\widetilde{a}}}\frac{m_{\widetilde{\tau}}^2 - m_{\widetilde{a}}^2}{2m_{\widetilde{\tau}}}\,\mathrm{T}_0\left(\frac{g_{*S}(T_0)}{g_{*S}(\tau_{\widetilde{\tau}})}\right)^{1/3}\left(\frac{4\pi^2 g_*(\tau_{\widetilde{\tau}})\tau_{\widetilde{\tau}}^2}{90\,\mathrm{M}_{\rm Pl}^2}\right)^{1/4}. \tag{B.20}$$

Bibliography

[1] H. Fritzsch, M. Gell-Mann, and H. Leutwyler, Phys. Lett. **B47**, 365 (1973).

[2] D. J. Gross and F. Wilczek, Phys. Rev. Lett. **30**, 1343 (1973).

[3] D. J. Gross and F. Wilczek, Phys. Rev. **D8**, 3633 (1973).

[4] H. D. Politzer, Phys. Rev. Lett. **30**, 1346 (1973).

[5] S. L. Glashow, Nucl. Phys. **22**, 579 (1961).

[6] S. Weinberg, Phys. Rev. Lett. **19**, 1264 (1967).

[7] A. Salam, Originally printed in *Svartholm: Elementary Particle Theory, Proceedings Of The Nobel Symposium Held 1968 At Lerum, Sweden*, Stockholm 1968, 367-377.

[8] P. W. Higgs, Phys. Lett. **12**, 132 (1964).

[9] P. W. Higgs, Phys. Rev. Lett. **13**, 508 (1964).

[10] P. W. Higgs, Phys. Rev. **145**, 1156 (1966).

[11] F. Englert and R. Brout, Phys. Rev. Lett. **13**, 321 (1964).

[12] G. S. Guralnik, C. R. Hagen, and T. W. B. Kibble, Phys. Rev. Lett. **13**, 585 (1964).

[13] A. Einstein, Annalen Phys. **49**, 769 (1916).

[14] S. Weinberg, Phys. Rev. **D13**, 974 (1976).

[15] S. Weinberg, Phys. Rev. **D19**, 1277 (1979).

[16] E. Gildener, Phys. Rev. **D14**, 1667 (1976).

[17] L. Susskind, Phys. Rev. **D20**, 2610 (1979).

[18] F. Zwicky, Astrophys. J. **86**, 217 (1937).

[19] D. Larson *et al.*, (2010), 1001.4635.

[20] S. P. Martin, (1997), hep-ph/9709356.

[21] R. D. Peccei and H. R. Quinn, Phys. Rev. **D16**, 1791 (1977).

[22] R. D. Peccei and H. R. Quinn, Phys. Rev. Lett. **38**, 1440 (1977).

[23] A. Freitas, F. D. Steffen, N. Tajuddin, and D. Wyler, Phys. Lett. **B679**, 270 (2009), 0904.3218.

[24] A. Freitas, F. D. Steffen, N. Tajuddin, and D. Wyler, Phys. Lett. **B682**, 193 (2009), 0909.3293.

[25] G. 't Hooft, Phys. Rev. **D14**, 3432 (1976).

[26] J. Goldstone, Nuovo Cim. **19**, 154 (1961).

[27] Particle Data Group, C. Amsler *et al.*, Phys. Lett. **B667**, 1 (2008).

[28] S. Weinberg, Phys. Rev. **D11**, 3583 (1975).

[29] A. A. Belavin, A. M. Polyakov, A. S. Schwartz, and Y. S. Tyupkin, Phys. Lett. **B59**, 85 (1975).

[30] D. B. Kaplan and A. V. Manohar, Phys. Rev. Lett. **56**, 2004 (1986).

[31] H. Georgi, Hadronic J. **1**, 155 (1978).

[32] M. A. B. Beg and H. S. Tsao, Phys. Rev. Lett. **41**, 278 (1978).

[33] R. N. Mohapatra and G. Senjanovic, Phys. Lett. **B79**, 283 (1978).

[34] A. E. Nelson, Phys. Lett. **B143**, 165 (1984).

[35] S. M. Barr, Phys. Rev. Lett. **53**, 329 (1984).

[36] S. Weinberg, Phys. Rev. Lett. **40**, 223 (1978).

[37] F. Wilczek, Phys. Rev. Lett. **40**, 279 (1978).

[38] S. L. Adler, Phys. Rev. **177**, 2426 (1969).

[39] J. S. Bell and R. Jackiw, Nuovo Cim. **A60**, 47 (1969).

[40] W. A. Bardeen, Phys. Rev. **184**, 1848 (1969).

[41] C. Vafa and E. Witten, Nucl. Phys. **B234**, 173 (1984).

[42] W. A. Bardeen and S. H. H. Tye, Phys. Lett. **B74**, 229 (1978).

[43] R. D. Peccei, To appear in Proceedings of 19th Int. Conf. on High Energy Physics, Tokyo, Japan, Aug 23-30, 1978.

[44] M. Dine, W. Fischler, and M. Srednicki, Phys. Lett. **B104**, 199 (1981).

[45] A. R. Zhitnitsky, Sov. J. Nucl. Phys. **31**, 260 (1980).

[46] J. E. Kim, Phys. Rev. Lett. **43**, 103 (1979).

[47] M. A. Shifman, A. I. Vainshtein, and V. I. Zakharov, Nucl. Phys. **B166**, 493 (1980).

[48] M. Beltran, J. Garcia-Bellido, and J. Lesgourgues, Phys. Rev. **D75**, 103507 (2007), hep-ph/0606107.

[49] P. Sikivie, Lect. Notes Phys. **741**, 19 (2008), astro-ph/0610440.

[50] F. D. Steffen, Eur. Phys. J. **C59**, 557 (2009), 0811.3347.

[51] J. T. Goldman and C. M. Hoffman, Phys. Rev. Lett. **40**, 220 (1978).

[52] J. Kandaswamy, P. Salomonson, and J. Schechter, Phys. Lett. **B74**, 377 (1978).

[53] Y. Asano *et al.*, Phys. Lett. **B107**, 159 (1981).

[54] J. M. Frere, J. A. M. Vermaseren, and M. B. Gavela, Phys. Lett. **B103**, 129 (1981).

[55] I. Antoniadis and T. N. Truong, Phys. Lett. **B109**, 67 (1982).

[56] J. E. Kim, Phys. Rept. **150**, 1 (1987).

[57] W. A. Bardeen, R. D. Peccei, and T. Yanagida, Nucl. Phys. **B279**, 401 (1987).

[58] R. Battesti *et al.*, Lect. Notes Phys. **741**, 199 (2008), 0705.0615.

[59] H. Primakoff, Phys. Rev. **81**, 899 (1951).

[60] H. Peng *et al.*, Nucl. Instrum. Meth. **A444**, 569 (2000).

[61] S. J. Asztalos *et al.*, Phys. Rev. **D69**, 011101 (2004), astro-ph/0310042.

[62] K. Zioutas *et al.*, Nucl. Instrum. Meth. **A425**, 480 (1999), astro-ph/9801176.

[63] CAST, K. Zioutas *et al.*, Phys. Rev. Lett. **94**, 121301 (2005), hep-ex/0411033.

[64] S. Moriyama *et al.*, Phys. Lett. **B434**, 147 (1998), hep-ex/9805026.

[65] R. Cameron *et al.*, Phys. Rev. **D47**, 3707 (1993).

[66] G. G. Raffelt, Lect. Notes Phys. **741**, 51 (2008), hep-ph/0611350.

[67] H. P. Nilles and S. Raby, Nucl. Phys. **B198**, 102 (1982).

[68] K. Tamvakis and D. Wyler, Phys. Lett. **B112**, 451 (1982).

[69] J. E. Kim and H. P. Nilles, Phys. Lett. **B138**, 150 (1984).

[70] J. E. Kim, Phys. Lett. **B136**, 378 (1984).

[71] J. E. Kim, Phys. Rev. Lett. **67**, 3465 (1991).

[72] D. H. Lyth, Phys. Rev. **D48**, 4523 (1993), hep-ph/9306293.

[73] S. Chang and H. B. Kim, Phys. Rev. Lett. **77**, 591 (1996), hep-ph/9604222.

[74] G. Lazarides, C. Panagiotakopoulos, and Q. Shafi, Phys. Lett. **B192**, 323 (1987).

[75] A. A. Penzias and R. W. Wilson, Astrophys. J. **142**, 419 (1965).

[76] E. Hubble, Proc. Nat. Acad. Sci. **15**, 168 (1929).

[77] E. Hubble and M. L. Humason, Astrophys. J. **74**, 43 (1931).

[78] S. Sarkar, Rept. Prog. Phys. **59**, 1493 (1996), hep-ph/9602260.

[79] K. Jedamzik and M. Pospelov, New J. Phys. **11**, 105028 (2009), 0906.2087.

[80] R. V. Wagoner, W. A. Fowler, and F. Hoyle, Astrophys. J. **148**, 3 (1967).

[81] V. F. Mukhanov, Int. J. Theor. Phys. **43**, 669 (2004), astro-ph/0303073.

[82] R. H. Cyburt, B. D. Fields, and K. A. Olive, JCAP **0811**, 012 (2008), 0808.2818.

[83] T. M. Bania, R. T. Rood, and D. S. Balser, Nature **415**, 54 (2002).

[84] A. De Rujula, S. L. Glashow, and U. Sarid, Nucl. Phys. **B333**, 173 (1990).

[85] S. Dimopoulos, D. Eichler, R. Esmailzadeh, and G. D. Starkman, Phys. Rev. **D41**, 2388 (1990).

[86] J. Rafelski, M. Sawicki, M. Gajda, and D. Harley, Phys. Rev. **A44**, 4345 (1991).

[87] M. Pospelov, Phys. Rev. Lett. **98**, 231301 (2007), hep-ph/0605215.

[88] M. Pospelov, (2007), 0712.0647.

[89] M. Pospelov, J. Pradler, and F. D. Steffen, JCAP **0811**, 020 (2008), 0807.4287.

[90] M. Kamimura, Y. Kino, and E. Hiyama, Prog. Theor. Phys. **121**, 1059 (2009), 0809.4772.

[91] R. H. Cyburt, J. R. Ellis, B. D. Fields, and K. A. Olive, Phys. Rev. **D67**, 103521 (2003), astro-ph/0211258.

[92] M. Asplund, D. L. Lambert, P. E. Nissen, F. Primas, and V. V. Smith, Astrophys. J. **644**, 229 (2006), astro-ph/0510636.

[93] K. Jedamzik, JCAP **0803**, 008 (2008), 0710.5153.

[94] K. Hamaguchi, T. Hatsuda, M. Kamimura, Y. Kino, and T. T. Yanagida, Phys. Lett. **B650**, 268 (2007), hep-ph/0702274.

[95] M. Kawasaki, K. Kohri, and T. Moroi, Phys. Lett. **B649**, 436 (2007), hep-ph/0703122.

[96] J. Pradler and F. D. Steffen, Eur. Phys. J. **C56**, 287 (2008), 0710.4548.

[97] J. Pradler and F. D. Steffen, Phys. Lett. **B648**, 224 (2007), hep-ph/0612291.

[98] M. Kawasaki, K. Kohri, and T. Moroi, Phys. Lett. **B625**, 7 (2005), astro-ph/0402490.

[99] M. Kawasaki, K. Kohri, and T. Moroi, Phys. Rev. **D71**, 083502 (2005), astro-ph/0408426.

[100] M. H. Reno and D. Seckel, Phys. Rev. **D37**, 3441 (1988).

[101] S. Dimopoulos, R. Esmailzadeh, L. J. Hall, and G. D. Starkman, Astrophys. J. **330**, 545 (1988).

[102] S. Dimopoulos, R. Esmailzadeh, L. J. Hall, and G. D. Starkman, Nucl. Phys. **B311**, 699 (1989).

[103] K. Kohri, Phys. Rev. **D64**, 043515 (2001), astro-ph/0103411.

[104] K. Jedamzik, Phys. Rev. **D70**, 063524 (2004), astro-ph/0402344.

[105] K. Jedamzik, Phys. Rev. **D74**, 103509 (2006), hep-ph/0604251.

[106] G. Sigl, K. Jedamzik, D. N. Schramm, and V. S. Berezinsky, Phys. Rev. **D52**, 6682 (1995), astro-ph/9503094.

[107] K. Jedamzik, Phys. Rev. Lett. **84**, 3248 (2000), astro-ph/9909445.

[108] R. H. Cyburt, J. R. Ellis, B. D. Fields, K. A. Olive, and V. C. Spanos, JCAP **0611**, 014 (2006), astro-ph/0608562.

[109] R. H. Cyburt *et al.*, JCAP **0910**, 021 (2009), 0907.5003.

[110] E. Holtmann, M. Kawasaki, K. Kohri, and T. Moroi, Phys. Rev. **D60**, 023506 (1999), hep-ph/9805405.

[111] S. Schilling, PhD Thesis, University of Zurich (2005).

[112] R. Mertig, M. Bohm, and A. Denner, Comput. Phys. Commun. **64**, 345 (1991).

[113] T. Hahn and M. Perez-Victoria, Comput. Phys. Commun. **118**, 153 (1999), hep-ph/9807565.

[114] G. 't Hooft and M. J. G. Veltman, Nucl. Phys. **B153**, 365 (1979).

[115] A. Brandenburg, L. Covi, K. Hamaguchi, L. Roszkowski, and F. D. Steffen, Phys. Lett. **B617**, 99 (2005), hep-ph/0501287.

[116] L. Covi, L. Roszkowski, R. Ruiz de Austri, and M. Small, JHEP **06**, 003 (2004), hep-ph/0402240.

[117] M. Hashimoto, K. I. Izawa, M. Yamaguchi, and T. Yanagida, Phys. Lett. **B437**, 44 (1998), hep-ph/9803263.

[118] M. Kawasaki, K. Nakayama, and M. Senami, JCAP **0803**, 009 (2008), 0711.3083.

[119] WMAP, D. N. Spergel *et al.*, Astrophys. J. Suppl. **170**, 377 (2007), astro-ph/0603449.

[120] Particle Data Group, W. M. Yao *et al.*, J. Phys. **G33**, 1 (2006).

[121] WMAP, J. Dunkley *et al.*, Astrophys. J. Suppl. **180**, 306 (2009), 0803.0586.

[122] J. Hamann, S. Hannestad, M. S. Sloth, and Y. Y. Y. Wong, Phys. Rev. **D75**, 023522 (2007), astro-ph/0611582.

[123] K. Rajagopal, M. S. Turner, and F. Wilczek, Nucl. Phys. **B358**, 447 (1991).

[124] T. Asaka and T. Yanagida, Phys. Lett. **B494**, 297 (2000), hep-ph/0006211.

[125] A. Brandenburg and F. D. Steffen, JCAP **0408**, 008 (2004), hep-ph/0405158.

[126] L. Covi, H.-B. Kim, J. E. Kim, and L. Roszkowski, JHEP **05**, 033 (2001), hep-ph/0101009.

[127] M. E. Gomez, S. Lola, C. Pallis, and J. Rodriguez-Quintero, JCAP **0901**, 027 (2009), 0809.1859.

[128] A. Strumia, JHEP **06**, 036 (2010), 1003.5847.

[129] E. Braaten and T. C. Yuan, Phys. Rev. Lett. **66**, 2183 (1991).

[130] K.-Y. Choi, L. Roszkowski, and R. Ruiz de Austri, JHEP **04**, 016 (2008), 0710.3349.

[131] H. Baer, M. Haider, S. Kraml, S. Sekmen, and H. Summy, JCAP **0902**, 002 (2009), 0812.2693.

[132] L. Covi, J. E. Kim, and L. Roszkowski, Phys. Rev. Lett. **82**, 4180 (1999), hep-ph/9905212.

[133] T. Asaka, K. Hamaguchi, and K. Suzuki, Phys. Lett. **B490**, 136 (2000), hep-ph/0005136.

[134] G. Belanger, F. Boudjema, A. Pukhov, and A. Semenov, Comput. Phys. Commun. **149**, 103 (2002), hep-ph/0112278.

[135] G. Belanger, F. Boudjema, A. Pukhov, and A. Semenov, Comput. Phys. Commun. **174**, 577 (2006), hep-ph/0405253.

[136] E. W. Kolb and M. S. Turner, Front. Phys. **69**, 1 (1990).

[137] W. B. Lin, D. H. Huang, X. Zhang, and R. H. Brandenberger, Phys. Rev. Lett. **86**, 954 (2001), astro-ph/0009003.

[138] J. Hisano, K. Kohri, and M. M. Nojiri, Phys. Lett. **B505**, 169 (2001), hep-ph/0011216.

[139] F. D. Steffen, JCAP **0609**, 001 (2006), hep-ph/0605306.

[140] E. Polisensky and M. Ricotti, (2010), 1004.1459.

[141] A. V. Maccio' and F. Fontanot, (2009), 0910.2460.

[142] J. J. Dalcanton and C. J. Hogan, Astrophys. J. **561**, 35 (2001), astro-ph/0004381.

[143] D. Boyanovsky, H. J. de Vega, and N. Sanchez, Phys. Rev. **D77**, 043518 (2008), 0710.5180.

[144] V. K. Narayanan, D. N. Spergel, R. Dave, and C.-P. Ma, (2000), astro-ph/0005095.

[145] M. Viel, J. Lesgourgues, M. G. Haehnelt, S. Matarrese, and A. Riotto, Phys. Rev. **D71**, 063534 (2005), astro-ph/0501562.

[146] M. Viel, J. Lesgourgues, M. G. Haehnelt, S. Matarrese, and A. Riotto, Phys. Rev. Lett. **97**, 071301 (2006), astro-ph/0605706.

[147] M. Viel *et al.*, Phys. Rev. Lett. **100**, 041304 (2008), 0709.0131.

[148] K. Jedamzik, M. Lemoine, and G. Moultaka, JCAP **0607**, 010 (2006), astro-ph/0508141.

[149] M. Kaplinghat, Phys. Rev. **D72**, 063510 (2005), astro-ph/0507300.

[150] K. Jedamzik, K.-Y. Choi, L. Roszkowski, and R. Ruiz de Austri, JCAP **0607**, 007 (2006), hep-ph/0512044v2.

[151] S. Bailly, K. Jedamzik, and G. Moultaka, Phys. Rev. **D80**, 063509 (2009), 0812.0788.

[152] K. Kohri, T. Moroi, and A. Yotsuyanagi, Phys. Rev. **D73**, 123511 (2006), hep-ph/0507245.

[153] J. L. Feng, A. Rajaraman, and F. Takayama, Phys. Rev. **D68**, 063504 (2003), hep-ph/0306024.

[154] J. Pradler, (2009), 0909.3429.

[155] M. Ratz, K. Schmidt-Hoberg, and M. W. Winkler, JCAP **0810**, 026 (2008), 0808.0829.

[156] J. Pradler and F. D. Steffen, Nucl. Phys. **B809**, 318 (2009), 0808.2462.

[157] M. Fukugita and T. Yanagida, Phys. Lett. **B174**, 45 (1986).

[158] S. Davidson and A. Ibarra, Phys. Lett. **B535**, 25 (2002), hep-ph/0202239.

[159] W. Buchmuller, P. Di Bari, and M. Plumacher, Ann. Phys. **315**, 305 (2005), hep-ph/0401240.

[160] S. Blanchet and P. Di Bari, JCAP **0703**, 018 (2007), hep-ph/0607330.

[161] S. Antusch and A. M. Teixeira, JCAP **0702**, 024 (2007), hep-ph/0611232.

[162] M. Kawasaki, K. Kohri, T. Moroi, and A. Yotsuyanagi, (2008), 0804.3745.

[163] J. Pradler and F. D. Steffen, Phys. Lett. **B666**, 181 (2008), 0710.2213.

[164] J. E. Kim, Phys. Rev. **D58**, 055006 (1998), hep-ph/9802220.

[165] M. Drees and X. Tata, Phys. Lett. **B252**, 695 (1990).

[166] A. Nisati, S. Petrarca, and G. Salvini, Mod. Phys. Lett. **A12**, 2213 (1997), hep-ph/9707376.

[167] S. Ambrosanio, G. D. Kribs, and S. P. Martin, Phys. Rev. **D56**, 1761 (1997), hep-ph/9703211.

[168] J. L. Feng and T. Moroi, Phys. Rev. **D58**, 035001 (1998), hep-ph/9712499.

[169] S. P. Martin and J. D. Wells, Phys. Rev. **D59**, 035008 (1999), hep-ph/9805289.

[170] M. Fairbairn *et al.*, Phys. Rept. **438**, 1 (2007), hep-ph/0611040.

[171] S. Ambrosanio, B. Mele, S. Petrarca, G. Polesello, and A. Rimoldi, JHEP **01**, 014 (2001), hep-ph/0010081.

[172] J. R. Ellis, A. R. Raklev, and O. K. Oye, JHEP **10**, 061 (2006), hep-ph/0607261.

[173] K. Ishiwata, T. Ito, and T. Moroi, Phys. Lett. **B669**, 28 (2008), 0807.0975.

[174] S. Kaneko, J. Sato, T. Shimomura, O. Vives, and M. Yamanaka, Phys. Rev. **D78**, 116013 (2008), 0811.0703.

[175] J. L. Feng and B. T. Smith, Phys. Rev. **D71**, 015004 (2005), hep-ph/0409278.

[176] A. De Roeck *et al.*, Eur. Phys. J. **C49**, 1041 (2007), hep-ph/0508198.

[177] S. Asai, K. Hamaguchi, and S. Shirai, Phys. Rev. Lett. **103**, 141803 (2009), 0902.3754.

[178] J. L. Pinfold and L. Sibley, (2010), 1006.3293.

[179] H. U. Martyn, Eur. Phys. J. **C48**, 15 (2006), hep-ph/0605257.

[180] A. Djouadi, J.-L. Kneur, and G. Moultaka, Comput. Phys. Commun. **176**, 426 (2007), hep-ph/0211331.

[181] T. Sjostrand, S. Mrenna, and P. Z. Skands, JHEP **05**, 026 (2006), hep-ph/0603175.

[182] J. Brau, (ed.) *et al.*, ILC-REPORT-2007-001.

[183] M. Dine, A. E. Nelson, and Y. Shirman, Phys. Rev. **D51**, 1362 (1995), hep-ph/9408384.

[184] M. Dine, A. E. Nelson, Y. Nir, and Y. Shirman, Phys. Rev. **D53**, 2658 (1996), hep-ph/9507378.

[185] G. F. Giudice and R. Rattazzi, Phys. Rept. **322**, 419 (1999), hep-ph/9801271.

[186] H. P. Nilles, Phys. Rept. **110**, 1 (1984).

[187] H. E. Haber and G. L. Kane, Phys. Rept. **117**, 75 (1985).

[188] F. D. Steffen, (2005), hep-ph/0507003.

[189] K. Hamaguchi, M. M. Nojiri, and A. de Roeck, JHEP **03**, 046 (2007), hep-ph/0612060.

[190] F. D. Steffen, Phys. Lett. **B669**, 74 (2008), 0806.3266.

[191] T. Asaka and M. Yamaguchi, Phys. Lett. **B437**, 51 (1998), hep-ph/9805449.

[192] F. D. Steffen, AIP Conf. Proc. **903**, 595 (2007), hep-ph/0611027.

[193] V. A. Smirnov, Commun. Math. Phys. **134**, 109 (1990).

[194] V. A. Smirnov, Mod. Phys. Lett. **A10**, 1485 (1995), hep-th/9412063.

[195] C. Anastasiou and A. Lazopoulos, JHEP **07**, 046 (2004), hep-ph/0404258.

Acknowledgements

First and foremost, I would like to thank Daniel Wyler for giving me the opportunity to do my PhD at this institute in Zürich. Thank you Daniel for giving me the freedom in my thesis and for your contagious and boundless enthusiasm for physics.

I would like to thank Ayres Freitas for his endless patience and for persevering with the project even when he moved six timezones away. I could not have completed it without his help.

I would also like to thank Frank Steffen for his contribution to the thesis. I have very much enjoyed our collaboration and learning various aspects of cosmology with him. His involvement has added a lot of variety to the thesis.

Thanks also go to my office mates Daniel Maitre, Nicolas Greiner, Pedro Schwaller and Rikkert Frederix. And to all at the institute members, present and former, who made my PhD time at the institute a lot of fun. I will especially remember the parties, the chocolate fondues and the bowling tournaments, not to mention the daily distraction of the table tennis and table football. I am sure to look back at my time here with great fondness.

A special mention goes to my Mum and Dad who encouraged me to take on the challenge and who have patiently waited while I finish it. I would also like to thank Kak Long, Alang, Atih and Eda, for the constant reminder of my seemingly permanent status as a student.

Most of all, I want to thank Christian, whose presence made this whole experience all the more special. Thank you for your support and encouragement, and for just being there.